11-11-2016

Full Analysis of Heat Pipes Including Fins and Nanofluids

Leonard M. Poplaski 5222235
University of Connecticut - Storrs, lenny.poplaski@uconn.edu

Full Analysis of Heat Pipes Including Fins and Nanofluid

Leonard M. Poplaski

B.S., University of Connecticut, 2014

A Thesis

Submitted in Partial Fulfillment of the

Requirement for the Degree of

Masters in Science

At the

University of Connecticut

2016

APPROVAL PAGE

Masters of Science Thesis

Full Analysis of Heat Pipes Including Fins and Nanofluids

Presented by

Leonard M. Poplaski, B.S.

Major Advisor_____

Amir Faghri

Associate Advisor_____

Tai-Hsi Fan

Associate Advisor_____

Xinyu Zhao

Associate Advisor_____

Michael Pettes

University of Connecticut
2016

Acknowledgement

I would like to thank the individuals that supported and guided me through my master's work. I have gained knowledge, experience, and friendships of which will be invaluable in the future. I would like to personally thank my parents for their continued support of my educational career both financially and through encouragement.

I would like to thank Dr. Faghri for allowing me the opportunity of performing research under his guidance. I have learned a broad range of experimental and numerical techniques in the topics of heat pipes, nanofluids, and two phase modeling. His teachings greatly enhanced my technical writing abilities and provided me much insight into engineering practices.

To my lab mates and friends for all their help and support, may we never forget all the times we have shared together. I will miss every one of you and hope that we shall remain in contact.

Finally, I would like to thank the National Science Foundation who without their financial support my research would not have been possible.

Table of Contents

APPROVAL PAGE iii
Acknowledgement iv
Abstract vii
Chapter 1. Heat Pipe Simulation Including External Coolant Flow 1
Nomenclature 1
1. Introduction 2
2. Physical model 4
2.1. Background 4
2.2. Governing equations 4
2.3. Boundary conditions 5
3. Thermal resistance network 6
4. Computational methodology 7
4.1. Steady-state simulations 7
4.2. Transient simulations 8
4.3. Channel flow convergence 8
5. Results and discussion 8
5.1. High temperature heat pipe (HTHP) verification 8
6. Low temperature heat pipe (LTHP) validation 11
Case 3: LTHP 11
6.1. Simulation with channel flow cooling 12
6.2. Case 4: LTHP channel flow cooling 12
6.3. Case 5: HTHP channel flow cooling 13
7. Conclusion 15
Acknowledgement 15
References 16
List of Figures 18
List of Tables 33
Chapter 2. Reduction of Heat Pipe Thermal Resistances Through the use of Nanofluid 41
Nomenclature 41
1. Introduction 42
2. Physical Model 46
3. Modified Merit Number 52
4. Computational Methodology 53

5. Results 54
5.1 Case A 54
5.2 Case B 55
5.3 Parametric Study 56
Conclusions 58
Acknowledgement 59
References 60
List of Figures 65
List of Tables 75
Chapter 3. Two-Phase Numerical Simulation of a Two-Phased Closed Thermosyphon 87
Nomenclature: 87
Introduction: 88
Two Phase Simulation Analysis: 92
Phase Continuity: 92
Momentum Equations: 93
Energy equation: 94
Boundary Conditions: 95
Solution Methodology: 96
Results: 96
Conclusion: 96
References: 97
List of Figures: 101

Abstract

Full numerical simulation of heat pipes was performed for heat pipes under various operating conditions with a variety of working fluids including fins and nanofluid. Two and three-dimensional models were developed assuming a laminar compressible vapor core. An advanced thermal resistance network for heat pipes was used along with the numerical model to identify dominate thermal resistances. Simulations were performed on heat pipes with external channel cooling around the condenser with and without external fins to determine the impact of individual heat pipe thermal resistances. It was found that the vapor core thermal resistance is significant as the operating temperature increases. The largest thermal resistances are those corresponding to the external heat sources and sinks.

The numerical model was extended for use with nanofluid-filled heat pipes and accounted for flow in the wick; to determine the capillary limit and corresponding optimal nanoparticle concentration. A revised Merit number was proposed for nanofluid-charged heat pipes and used to quantify performance enhancements. Three nanoparticles were explored in this study Al_2O_3, TiO_2 and CuO. The optimal nanoparticle concentration of Al_2O_3, TiO_2 and CuO corresponding to the capillary limit for a conventional nanofluid-filled heat pipe was determined to be 25% by vol. for both Al_2O_3 and TiO_2, and 35% for CuO. Overall, a maximum decrease in total thermal resistance was observed to be 83%, 79% and 76% for Al_2O_3, CuO and TiO_2, respectively. Finally, a homogenous multiphase model was developed for simulation of a thermosyphon and some preliminary results were obtained for the operation of the condenser section.

Chapter 1. Heat Pipe Simulation Including External Coolant Flow

Nomenclature

A	area (m^2)
c_p	specific heat (J/kgK)
$\boldsymbol{h}$	heat transfer coefficient (W/m^2 K)
h	enthalpy (J/kg)
HTHP	high temperature heat pipe
h_{fg}	latent heat (J/kg)
k	thermal conductivity (W/m K)
L	length (m)
LTHP	low temperature heat pipe
$\dot{m}''$	mass flux (kg/s)
Nu	Nusselt number
n	normal vector
Pr	Prandtl number
p	pressure (Pa)
Q	heat rate (W)
q''	heat flux (J/m^2)
R	thermal resistance (W/K)
R_g	universal gas constant (J/kg K)
Re	Reynolds number
r	radius (m)
T	temperature (K)
t	thickness (m), time (s)
V	velocity (m/s)
v	specific volume
W	work *(J)*, width (m)
x, y, z	spatial coordinates

Greek symbols

ε	emissivity
θ	circumferential angle
μ	dynamic viscosity ($N{\cdot}s/m^2$)
ρ	density (kg/m^3)
σ	Stefan-Boltzmann constant
τ	viscous stress tensor (N/m^2)
φ	porosity

Subscripts

a	adiabatic
abs	absolute
act	actual
c	condenser
cell	cell value
D	diameter (m)
e	evaporator
eff	effective
ex	external
$ex-f$	external to fin
$ex-w$	external to wall
f	fluid
f	fin
gage	gage value
hp	heat pipe
i	i^{th} component, inner
in	input
inter	interface
inlet	inlet
l	liquid
o	outer
op	operating
out	outlet
s	solid
sat	saturation
surr	surrounding
tot	total
theo	theoretical
v	vapor
w	wall
wk	wick
0	reference value
∞	free stream

1. Introduction

Heat pipe applications range from the cooling of consumer electronics such as laptops [1-2] to thermal management of spacecraft [3]; proposed uses include turbine blade and high speed aircraft wing cooling [2]. A heat pipe generally consists of an evaporator (heat input), a condenser (heat output), and an adiabatic (heat transport) region. Heat pipes are able to achieve high heat transfer rates compared to traditional heat transfer devices due to phase change of the internal working fluid. At the evaporator section, heat is conducted through the heat pipe wall and wick, vaporizing the working fluid in the saturated wick. The vapor flows to the condenser due to a pressure gradient, where it is then condensed and returned to the evaporator by capillary action in the wick.

Two-dimensional simplified numerical models have shown good agreement with experimental results [4–6]. A two-dimensional transient numerical model for a heat pipe with compressible vapor flow was presented by Cao and Faghri [4] to simulate high temperature heat pipe operation. The heat transfer in the wick was assumed to be governed by pure conduction. The numerical model was validated with experimentally obtained pressure and vapor temperature distributions with good success. Buchko and Faghri [6] extended the work of Cao and Faghri [4] by modeling low temperature heat pipes with multiple heat sources and accounted for the effects of porosity and permeability in the wick structure. The effect of spatial distribution of the heat load was investigated, and decomposition of the heat input into multiple locations was found to increase the maximum heat transferred across a single heat pipe. Rice and Faghri [5] performed a detailed numerical analysis of both low and high temperature heat pipes, accounting for flow in the wick to determine the capillary pressure required for the return of the working fluid. Ranjan et al. [7] developed a model including the effects of the wick micro-structure on the overall heat transfer rate. Two numerical models were employed, the first was a macro-model where the phase-change rates and the temperature/pressure at the solid-liquid interface was obtained through an energy balance at the interface. The second method examined the wick micro-structure and computed the phase change rates from the liquid meniscus formed in the pores. The two models were then coupled to predict the performance of a heat pipe with a screen wick.

Zuo and Faghri [8] developed an equivalent thermal network to simplify the simulation of transient heat pipe operation. The thermal resistance of the internal working fluid flow was assumed to be negligible during transient operation, and was therefore excluded in the model. A thermodynamic representation of heat pipe operation was also discussed using a *T*-*S* diagram, from which proper heat pipe functionality was justified.

Xiao and Faghri [9] developed a complex numerical model of a three-dimensional flat plate heat pipe, and predicted its thermodynamic behavior without use of empirical correlations. The flow in the vapor core was assumed laminar and incompressible with state properties following the ideal gas relation. The wick was assumed to be saturated with working fluid and have constant transport properties. Inclusion of a vertical column wick was found to lower the thermal resistance and increase the capillary limit, resulting in a higher axial pressure drop and larger liquid and vapor velocities. Kaya and Goldak [10] also studied three-dimensional heat

pipe operation using the finite element numerical method where the mass, momentum and energy conservation equations were solved for the vapor and liquid flow. The obtained numerical velocity and pressure distributions were verified with experimentally obtained data. It was shown that the vapor flow field remains nearly symmetric around the heat pipe.

Transport of heat by a flat heat pipe with multiple discrete heat sources was evaluated by Vaddakan et al. [11]. The numerical model was used to simulate heat transfer and fluid flow in the wick. The heat input and evaporator locations were varied to determine where and when dry out would first occur. Similar to Buchko and Faghri [6], it was found that a decrease in heat pipe operating temperature can be achieved by separating the heat input into smaller sources with larger separation between each source.

In this work, a numerical model for a three-dimensional cylindrical heat pipe has been developed to analyze the component thermal resistances of the heat pipe, including the external thermal resistances of the heat sources and sinks. A single-domain conjugate approach, with no empirical correlations, was used in order to obtain accurate thermal resistance values. In addition, simulations were performed including the full coolant flow field around the heat pipe condenser. To our knowledge, this is the first attempt to simulate a three-dimensional heat pipe in conjunction with the external flow of coolant.

2. Physical model

2.1. Background

Heat pipes are passive two-phase devices capable of high heat transfer rates while maintaining a low temperature drops. Heat input at the evaporator causes the working fluid to vaporize, which flows to the condenser where the hot vapor releases its latent energy to the cooler condenser wick and wall. Capillary action in the wick aids in the return of the working fluid to the evaporator (heat pipes), while wickless heat pipes (thermosyphons) rely on gravity to return the working fluid and are limited to certain inclination angles with the evaporator placed below the condenser. Figure 1 shows the typical elements and configuration of a heat pipe with fins, and a flow channel external to the condenser. The heat pipe consists of three main radial regions: (1) the vapor core, where the evaporated working fluid is transported, (2) the wick, which aids in the return of the condensed working fluid to the evaporator, and (3) the wall which provides structural rigidity. Heat (Q_{in}) enters the evaporator (L_e), and leaves at the condenser (L_c). In some numerical cases, fins were included on the condenser outer surface of the heat pipe to aid in the rejection of heat to the external working fluid, of the coolant channel.

2.2. Governing equations

The three-dimensional governing equations were solved assuming the vapor flow to be laminar and compressible with constant properties [12].

Conservation of mass:

$$\frac{\partial \rho}{\partial t} + \nabla \cdot \rho V = 0 \tag{1}$$

Conservation of momentum:

$$\frac{\partial}{\partial t}(\rho V) + \nabla \cdot (\rho V V) = -\nabla p + \nabla \cdot \tau \tag{2}$$

Conservation of energy:

$$\frac{D}{Dt}(\rho h) + \nabla \cdot q'' = \frac{Dp}{Dt} + \nabla V : \tau \tag{3}$$

where $\nabla V : \tau$ is the viscous dissipation term.

The density of the vapor is described by the ideal gas relation:

$$\rho = \frac{p}{RT} \tag{4}$$

The flow in the wick was considered negligible, and the associated convective heat transfer was neglected; thus, the heat transfer in the wick was modeled as pure conduction. Therefore,

the governing equations for heat transfer in the wick and wall are given by following form of the heat equation:

$$\nabla \cdot k\nabla T = \rho c_p \frac{\partial T}{\partial t} \tag{5}$$

The wick is composed of a screen wire mesh with an effective thermal conductivity [13]:

$$k_{eff} = \frac{k_l[k_l+k_s-(1-\varphi)(k_l-k_s)]}{(k_l+k_s)+(1-\varphi)(k_l-k_s)} \tag{6}$$

where k_s and k_l are the solid and liquid thermal conductivities, respectively, and φ is the porosity of the wick.

The equations for continuity, momentum and energy are solved for the external cooling flow when a heat transfer fluid (HTF) is employed at the condenser surface. It is assumed that the external flow of coolant is steady, laminar and incompressible with negligible buoyancy forces. The walls of the coolant channel are insulated and conductive heat transfer in the channel walls is neglected. The conjugate heat transfer between the heat pipe and coolant was fully simulated, and the contact resistances in the heat pipe and flow channel are assumed to be insignificant.

2.3. Boundary conditions

The following boundary conditions are applicable to the cases without external fins. When fins are included on the condenser surface, conduction through the fins is solved and the external fin surface is modeled as a convective boundary similar to the condenser wall.

At the evaporator wall

In each case with a constant heat flux applied to the evaporator (Cases 1-4, Cases 5: A-C, F and G):

$$k\nabla T \cdot n = \left.\frac{Q_{in}}{A}\right|_{r=r_0,\ 0 < y < L_e} \tag{7}$$

When a constant heat transfer coefficient convection is applied to the evaporator wall (Cases 5: D, E, H and I), flux matching was performed between Fourier's law and Newton's law of cooling, yielding:

$$k\nabla T \cdot n = \boldsymbol{h}(T_\infty - T_{e,ex-w})\Big|_{r=r_0,\ 0 < y < L_e} \tag{8}$$

It should be noted that a value of $\boldsymbol{h}$ is used assuming liquid water as the heat input fluid.

At the condenser wall (9)

The heat transfer modes external to the condenser were one of the following: constant heat transfer coefficient convection, constant heat sink, radiative and channel flow. Constant heat transfer coefficient convective heat transfer at the condenser, Equation (8), is applied using the

free stream temperature, wall temperature and heat transfer coefficient corresponding to the coolant. In the case of a constant convective boundary condition the value of $\boldsymbol{h}$ is assumed based on previous work's [4-6], and directly applied in Equation (8) (Cases 1-3). When the heat pipe is modeled with channel flow cooling (Case 4 A-D, Case 5: A, E-F), predictions for $\boldsymbol{h}$ are calculated and used to theoretically predict the external condenser thermal resistance.

For *radiation:*

$$k\nabla T \cdot n = \varepsilon\sigma(T_{surr}^4 - T_{c,ex-w}^4)_{r=r_0,\ L_e + L_a < y < L_e + L_a + L_c} \tag{10}$$

For a *constant heat flux heat sink:*

$$k\nabla T \cdot n = \left.\frac{-Q_{in}}{A}\right|_{r=r_0,\ L_e + L_a < y < L_e + L_a + L_c} \tag{11}$$

The channel is described with boundary conditions of: a velocity inlet, pressure outlet and no slip insulated walls.

In the *coolant channel* ($L_e + L_a \le y \le L_e + L_a + L_c, 0 < x < W, z = z_{in}$) (12)

an inlet velocity, V_{inlet}, and temperature, T_{inlet}, are specified

At the *outlet of the channel* ($L_e + L_a \le y \le L_e + L_a + L_c,\ 0 < x < W,\ z = z_{out}$) (13)

the gage pressure is set such that:

$$p_{gage} = p_{abs} - p_{op} = 0 \tag{14}$$

At any of the channel wall locations, the heat transfer and velocity are zero. The internal boundary conditions at the wick-vapor interface of the heat pipe are provided by a velocity inlet and temperature boundary.

The energy balance at the wick-vapor interface is used to determine the interfacial velocity for the vapor region:

$$\dot{q}''_{inter} = \left(\dot{m}'' h_{fg}\right)_{inter} = \left(\rho_v v_v h_{fg}\right)_{inter} \tag{15}$$

The Clausius-Clapeyron equation is used to determine the interfacial temperature:

$$T_{sat} = \left[\frac{1}{T_0} - \frac{R_g}{h_{fg}} ln\left(\frac{p_v}{p_0}\right)\right]^{-1} \tag{16}$$

3. Thermal resistance network

Thermal resistance is defined as the ratio of the driving potential (temperature) to the corresponding heat transfer, and is used to identify which component *i* of the heat pipe restrict heat transfer:

$$R_i = \frac{\Delta T_i}{Q_i} \tag{17}$$

where T_i is the spatially averaged temperature of the heat pipe component.

The thermal resistance network for a heat pipe is outlined pictorially in Figure 2, and the corresponding equations for each heat pipe component are given in Table 1. For cases involving external channel flow (Case 4 and Case 5 A, F, G, H and I), the heat transfer coefficient $\boldsymbol{h}$ was predicted analytically using [14]:

$$\overline{\mathrm{Nu}} = 0.3 + \frac{0.62 Re_D{}^{1/2} \mathrm{Pr}^{1/3}}{\left[1+(0.4/\mathrm{Pr})^{2/3}\right]^{1/4}} \left[1 + \left(\frac{\mathrm{Re}_D}{282000}\right)^{5/8}\right]^{4/5} \tag{18}$$

The external flow around the heat pipe is the primary area of interest since it has the greatest influence on the heat transfer from the condenser surface; thus the external Reynolds number was calculated based on heat pipe diameter, and found to be laminar in all cases.

4. Computational methodology

The governing equations with the associated boundary conditions were solved using the finite-volume approach [15]. Symmetry was assumed about the *yz* plane of the flow channel; therefore only half of the physical domain was solved. A user defined function (UDF) was written for the commercial software package ANSYS Fluent to set the temperature of the wick-vapor interface and the blowing/suction velocity of the vapor at the interface. The assigned interface velocity emulates the phase change that occurs at the wick surface.

Two solution methods were considered: 1) steady-state and 2) transient. Provided with enough time steps, the transient method converges to the same steady-state solution. Simulations were performed on a Dell Optiplex 7020 (running Microsoft Windows 7 equipped with an Intel i7 – 4790 processor and 16 GB of RAM).

4.1. Steady-state simulations

For simulations where the time dependent details of operation were of negligible importance, the transient terms in the governing equations were disregarded, and no initial conditions were provided. A pressure gradient appears in governing Equations (2-3), however, no pressure is known in the heat pipe, and therefore an infinite number of steady-state solutions exist for the pressure distribution. The coupling between pressure and saturation temperature (Equation 16) produces an infinite number of steady-state temperature distributions that satisfy the applied boundary conditions. To obtain the unique solution, with the correct heat pipe operating pressure, an iterative process is performed where the vapor end cap closest to the condenser ($x = 0, y = L_e + L_a + L_c$ in Figure 1) is modeled as a pressure outlet and the vapor core is simulated as an open system. With the vapor core modeled as an open system, the pressure difference between the end cap and the vapor allow mass to exit the

heat pipe. The mass flow rate through the end cap is then used to calculate the amount of heat leaving the end cap:

$$Q_{out} = \frac{\dot{m}_{out}}{h_{fg}} \tag{19}$$

To reduce the mass leaving the control volume the operating temperature is correct and the corresponding saturation pressure is set as the operating pressure. When the outflow mass is zero, the internal pressure drop is the same as for a closed heat pipe. In this work, the steady-state method was only applied to heat pipes with convective boundary conditions. More information may be found in [5] for steady-state simulations using other boundary condition types. The correction for convective sinks is:

$$\Delta T = \frac{\dot{m}_{out} h_{fg}}{A_{c,o} h} \tag{20}$$

To properly apply the method outlined above, the following steps must be taken:

1. Supply a guess operating temperature and corresponding pressure
2. Perform steady-state iterations of the governing equations until the mass flow rate has converged
3. Use the mass flow rate to calculate the operating temperature correction ΔT
4. Correct the operating temperature and pressure of the domain

Steps 2-4 are repeated until the net heat rate between the condenser and the evaporator is within a set tolerance.

4.2. Transient simulations

The full set of governing equations are solved including the transient terms using an implicit scheme. The implicit scheme does not have a maximum time step required to prevent divergence, however, more computational time is required than for the steady state formulation.

4.3. Channel flow convergence

To reduce computation time, a converged flow field was obtained with and without fins, and then supplied as a guess to the coupled heat pipe channel flow problem. The effects of start-up were not evaluated in the case of channel flow, thus only the previously outlined steady-state solution formulation was utilized.

5. Results and discussion

5.1. High temperature heat pipe (HTHP) verification

High temperature heat pipes have operating temperatures of 750 K or above [13], with common working fluids being sodium, silver and lithium. The numerical model was compared with the high temperature experimental and numerical data of sodium filled heat

pipes [4-6], to verify its accuracy. The first case (Case 1) tested the consistency of results generated by the steady-state and transient methods for a heat pipe with constant heat input to the evaporator and a condenser cooled by convection. The results were compared to those of Rice and Faghri [5], Cao and Faghri [4] and the experimental data of Ivanovski et al. [16]. Case 2 involves the transient response of the heat pipe to a step heat input. Case 2 simulations were performed for both radiative and convective cooling of the condenser. Results for both cooling conditions were verified with the numerical results of Cao and Faghri [4]. The dimensions of the heat pipes for Case 1 and Case 2 are listed in Table 2, along with their respective working fluids, heat inputs, as well as wall and wick thermophysical properties.

Case 1: HTHP steady state operation

Overview of Case 1:

- Constant heat rate input (560 W)
- Convective cooling (58.5 W/m^2K)
- Validated to experimental data of Ivanovski et al. [16]
- Verified to the numerical simulations of Cao and Faghri [4] and Rice and Faghri [5]

Case 1 uses dimensions and properties similar to those of Cao and Faghri [4] and Rice and Faghri [5] to simulate the heat pipe experiments of Ivanovski et al. [16]. The sodium heat pipe has an evaporator heat rate of 560 W, and a condenser cooled by convection with a heat transfer coefficient of 58.5 W/m^2K and reference temperature of 300 K. The simulation proceeded until a steady-state solution was obtained, and was validated with the experimental wall temperature distribution reported by Ivanovski et al. [16]. A similarity solution published by Faghri [17] was used to verify the internal pressure distribution. The computational mesh for Case 1 contained 40 cells in the axial direction, 10 cells in the radial, and 20 cells in the azimuthal direction. The wick and wall each contained 2 cells while the vapor region contained 6. The average surface temperatures of the condenser and evaporator were monitored, and less than 0.5 percent variation in each was observed after 2000 iterations. The computation time was approximately 8 hours. The difference between the predicted and measured temperature is largest in the adiabatic region of the heat pipe.

The axial temperature variation are plotted in Figure 3a, and the obtained numerical results are compared to the existing numerical and experimental data, with good agreement. Slight deviations are attributed to the difference in vapor properties used in each study.

In Figure 3b, it can be seen that the numerically obtained pressure drop differs from the similarity solution by a maximum of 8%. It was observed that the largest absolute pressure difference exists at the end of the adiabatic region, at which point the vapor decelerates.

Thermal resistances obtained from Case 1 are provided in Table 3. In Case 1, the thermal resistance of the vapor core was found to be dominant for the heat pipe, at almost 50% of the overall thermal resistance. This can be attributed to the high thermal conductivity and small thickness of the heat pipe wall, which imposes a negligible impedance on the transfer of heat, along with the larger temperature drop experienced by the vapor. The dominant resistance is that

of the condenser external flow. This is expected, since the internal resistances of the heat pipe are dependent on the phase change of the working fluid, and thus have much less influence on the temperature drop.

Case 2: HTHP stepped heat input

Overview of Case 2:

- Constant heat rate input of 623 W stepped up to 770 W (Cases 2 A and B)
- Convective cooling 39 W/m^{2}K $T_\infty = 300$ K (Case 2 A)
- Radiative cooling $\varepsilon = 0.85$, $T_{ref} = 0$ K (Case 2 B)
- Verified to the numerical simulations of Cao and Faghri [4] and Rice and Faghri [5]

A high temperature heat pipe with a constant heat input of 623 W was simulated using the transient model until steady-state was attained, at which time the heat input was increased to 770 W. Heat pipe cooling was provided by one of two means: radiation (Case 2 A, $\varepsilon = 0.85$, $T_{ref} = 0$ K) or convection (Case 2 B, $\boldsymbol{h}$ = 39 W/m^{2}K, $T_\infty = 300$ K). The computational mesh had 80 cells in the *z*-direction, 10 cells in the radial direction and 20 in the azimuthal direction. The computation time to obtain a steady-state solution was approximately 14 hours for Method 2 (transient) and 8 hours for Method 1 (steady).

Figure 4 shows the vapor temperature of the heat pipe at different times as it transitions to steady-state (the rate of heat addition is equal to rate of heat removal). An instantaneous increase in heat input is applied to a heat pipe initally at steady-state (Figure 4a) and is again allowed to reach steady-state operation (Figure 4c). Figure 4b shows the wall temperature after 10 seconds. A larger vapor temperature drop exists in Figure 4a than in Figure 4c (~ 30 K versus 13 K), which implies that the thermal resistance of the vapor core decreases as the heat pipe approaches steady-state operation. A similar trend is apparent for convective cooling (Figure 5), where the temperature drop decreases with time. The temperature drop is larger in Figure 5a (immediately after the increase in heat rate) than in Figure 5c (at steady-state operation), indicating a greater thermal resistance through the vapor core. Pressure drops at steady-state are provided for Case 2 A and B in Figure 6a and b, respectively. The heat pipe in Case 2 A showed a larger centerline absolute pressure drop when compared to Case 2 B, due to a greater wall temperature difference. Since the heat pipe vapor core is an ideal gas, an increase in the wall temperature drop induces a corresponding change in vapor temperature and thus increases the absolute vapor pressure drop.

In Case 2 A, the largest heat pipe thermal resistances were found to be those in the evaporator. The vapor core ceased to be the largest thermal resistance because of the increase in condenser surface area from Case 1, which allows for a more even distribution of heat (lower end-to-end vapor temperature drop). In Case 2 B, the thermal resistance through the vapor core was further reduced from Case 2 A. This phenomenon is explained by examining the vapor core thermal resistance equation and evaluating it under different operating conditions. By applying the ideal gas equation of state to Equation 25b, we can remove the temperature terms:

$$\Delta R = \frac{8 L_{\text{eff}}}{\pi R_g {r_i}^4} \left(\frac{\mu_{v2} p_{v2}}{{\text{h}_{fg2}}^2 {\rho_{v2}}^3} - \frac{\mu_{v1} p_{v1}}{{\text{h}_{fg1}}^2 {\rho_{v1}}^3} \right) \tag{21}$$

where subscripts 1 and 2 denote the states to be compared. The above relation shows a third order inverse dependence between the vapor core thermal resistance and the working fluid density. Since the density is highly dependent on the temperature and pressure of the heat pipe, large variations in thermal resistance can be expected. Using the average properties of Case 2 A (denoted 1) and Case 2 B (denoted 2) in Equation (21), it can be shown that the thermal resistance increases by a full order of magnitude and that the largest contributors to this effect were due to changes in density and pressure.

The conduction through the wick and wall for Case 1 and Case 2 agreed well with the theoretical calculations (Table 3). The thermal resistance through the evaporator wall was of greater magniture than the condenser wall resistance in both Cases. The evaporator was relatively short in Case 2; since the thermal resistance of the evaporator section is inversely proportional to the evaporator length, a greater thermal resistance was obtained. Similarly, the thermal resistance through the evaporator wick was of the next highest magnitude.

In determination of the interfacial resistances, the thermal accommodation factor was assumed unity. This showed good agreement for Case 1, however, Case 2 A and Case 2 B showed larger variations from the predicted values. In either case, the estimates were still within reasonable agreement.

6. Low temperature heat pipe (LTHP) validation

Case 3: LTHP

Overview of Case 3:

- One heater at a constant heat rate input of 97 W (Case 3 A)
- Two heaters each at a constant heat rate input of 98 W (Case 3 B)
- Condenser modeled as a constant heat sink equal to the rate of heat input (Case A and B)
- Verified with the numerical results of Rice and Faghri [5]
- Validated with experimental results of by Buchko and Faghri [6]

Low temperature heat pipes (LTHPs) operate in the 200 to 550 K temperature range and typically use water, ammonia or acetone as working fluids [13]. The LTHP experiment performed by Buchko and Faghri [6] had multiple heat sources; their experimental data was used to verify the current numerical model. This heat pipe differed from previously simulated by incorperating multiple evaportor sections seperated by adiabatic regions (the locations of the evaporator sections are given in Table 1). Since the experimental flow rates and temperatures were not reported by Buchko and Faghri [6], the condensor was modeled as a constant heat sink. Two cases were performed for the low temperature heat pipe: Case A used heater 1 (e1) with an input of 97 W, and Case 3 B used heaters 1 (e1) and 2 (e2) with an input of 98 W each. For both cases, the mesh had 138, 7, and 14 cells in the *z*-direction, radial and azimuthal, respectively. Three of the 7 radial cells were in the wick domain, while the remaining were located in the vapor. The reference temperature for each case was obtained from the estimated mean vapor

temperature of the experimental results. The properties and dimensions for each case are listed in Table 1. Since a constant heat source(s) and sink were applied as the input and output, the external resistences do not exist and are excluded from those reported in Table 4. The simulation took approximately 4 hours to reach time invariant temperatures.

The evaporator wall-vapor core temperature drop, shown in Figure 7, was approximatly the same when either one heater (97 W heat input) or two heat inputs (98 W, each) were applied. By dividing the evaporator into multiple sections, it was possible to minimize the temperature rise in the heated sections. However, if the heat input is doubled, the condenser wall temperature must decrease to provide further cooling; as such, Case 2 B was found to have a larger wall temperature drop (~17 K) than Case 2 A (~12 K).

The pressure drops shown in Figure 8 are in good agreement with the similarity solution of Faghri [17], with both solutions demonstrating a pressure drop recovery at the beginning of the condenser. In Case 3 A, less deviation was found compared to the analytically predicted thermal resistance than for Case 3 B (3.5% and 11.5% of the total pressure drop, respectively). This may be attributed to the method used to obtain the empirical vapor core thermal resistance. To account for the multiple evaporators and adiabatic sections, an effective length was used to calculate the vapor core thermal resistance. The effective evaporator length was defined as the sum of each individual evaporator length. Furthermore, there may be some heat loss through the adiabatic region between the two heaters; therefore this assumption may underestimate the true thermal resistance.

In the performed LTHP simulations, the vapor core and interfacial thermal resistances can be considered negligible since they are several orders of magnitude smaller than those of the wick or wall (Table 3). The heat pipe wall is relatively thin and made of highly conductive copper, therefore the thermal resistances associated with heat transfer in the wall were found to be negligible, and the wick thermal resistances were the primary impedance to heat transfer.

6.1. Simulation with channel flow cooling

The channel flow simulations involved separate cases of heat pipes operating at high and low temperatures with air flow modeled around the condenser wall. The channel flow simulations solve the conjugate heat transfer of the heat pipe and air coolant, and thus did not employ a constant heat transfer coefficient at the surface of the condenser wall. Temperature variations were found from the leading to trailing edge of the heat pipe, depicted in Figure 9. LTHPs with channel flow cooling were investigated in Case 4, while HTHPs were simulated in Case 5. Properties and dimensions are given in Table 1.

6.2. Case 4: LTHP channel flow cooling

Overview of Case 4:

- No condenser fins were included in Cases 4 (A and B)
- 3 condenser fins were included in Cases 4 (C and D)
- A constant heat input of 10 W heat input with convective cooling was used in Cases 4 (A and C)
- A constant heat input of 20 W heat input with convective cooling was used in Cases 4 (B and D)

LTHPs were simulated with fins (Cases 4 B and D) and without fins on the condenser (Cases A, C), under a constant heat input of 10 W (Cases A and B), which was then doubled to 20 W in subsequent simulations (Cases C and D). Three evenly-spaced aluminium fins were added to increase the heat transfer area for the cases with condenser fins.

Increasing the heat input from 10 to 20 W on the unfinned heat pipe resulted in an increased leading-to-trailing edge temperature variation (Figure 10). However, the magnitude of this temperature variation is still small when compared with the overall evaporator to condenser wall temperature drop (< 5%). A considerable variation in vapor core thermal resistance (Table 5) was observed in most Cases (> 300%). However, the axial temperature change of the vapor core only differs from the analytically predicted temperature by $1 \cdot 10^{-6}$ K, which may not be computationally or physically feasible.

In Case 4 C and Case 4 D, the total vapor core thermal resistance was negligible when compared to the wick and wall. The addition of condenser fins did not greatly increase the vapor core thermal resistance because the temperature drop was negligible. Due to the low thermal conductivity of the wall and wick material, the thermal resistances due to conduction dominate. In order to optimize heat pipe operation, the wall material could be changed from stainless steel to copper, increasing heat transfer rates.

6.3. Case 5: HTHP channel flow cooling

Overview of Case 5:

- No condenser fins were included in Cases 5 (A, B, D, F and H)
- 6 Fins were included in the condenser of Cases 5 (C, E, G and I)
- Constant heat input with constant convective cooling was applied in Cases 5 (B and C)
- Convective heat input with convective cooling was applied in Case 5 (D and E)
- Constant heat input with channel flow cooling was applied in Cases 5 (A, F, and G)
- Convective heat input with channel flow cooling was applied in Cases (H and I)

The external channel flow simulation method was expanded to HTHPs and validated with experimental results of Ivanovski et al. [16]. In order to verify the accuracy of the channel flow model, simulations were performed with a constant convection coefficient at the condenser section, with heat transfer coefficients estimated from the bulk fluid properties of the channel flow cases. This provided predictions for the heat pipe thermal resistances, wall temperature variations, and pressure drops.

Heat was provided to the evaporator in one of two ways: 1) constant heat input (Cases 5 A, B, F and G) and 2) convective heat input (Cases 5 D, E, H and I). Heat pipes were simulated without condenser fins (Cases A, B, D, F and H) and with six evenly spaced condenser fins (Cases C, E, G, and I). Channel flow cooling was included in Cases 5 A, F, G, H and I with a flow velocity intended to match the heat transfer coefficient used in Case 5 B, C, D and E. All heat pipe properties and dimensions are provided in Table 2.

Case 5 A used the data from Ivanovski et al. [16] to validate the channel flow model using an inlet channel velocity estimated by matching the heat transfer coefficient provided by Cao and Faghri [4]. As an estimate, this showed good agreement with the vapor temperatures from Case 1 (within ~3 K on average, shown in Figure 11a). The pressure drop in Figure 12a shows that the numerical simulation only deviated from the similarity solution by 10 % of the maximum pressure drop.

A LTHP with constant heat input, convective cooling and no condenser fins was simulated in Case 5 B and compared to a LTHP with 6 condenser fins (Case 5 C). The wall temperature (Figure 11b, c) was found to decrease with the addition of fins by approximately 70 K. For Case 5 C, a larger driving pressure drop was found (Figure 12c) than in Case 5 B, (Figure 12b) at 15% to 11% of the maximum pressure drop when compared to the similarity solution. This is due to a sudden drop in pressure is experienced in the vicinity of the fins. The finned heat pipe had an 18% lower external condenser thermal resistance (Table 6) than the un-finned heat pipe under the same conditions. The vapor core thermal resistance, however, was found to be larger for the finned heat pipe. This is due to a decrease in the heat pipe operating temperature which decreased the vapor core density, and increased the thermal resistance.

Heat pipe simulations were performed without fins (Case 5 C) and with fins (Case 5 D) for a convectively cooled and heated heat pipe. The addition of fins reduced the mean wall temperature by about 170 K (Figure 11e) from the un-finned heat pipe (Figure 11d). Again, a greater vapor pressure drop deviation was found for Case E due to the presence of external condenser fins (~ 5 % higher than Case D). The thermal resistance of the overall system with added fins was 30% less than the un-finned case (Table 6). The heat transferred with fins was also increased by 30% from the un-finned heat pipe.

For the convective cooling cases without fins, the thermal resistances of the wick and wall dominate over those of the interface and vapor core. For the finned heat pipe, the thermal resistance through the vapor core becomes of greater concern. In all cases of constant convective cooling, the external condenser thermal resistance was the largest system resistance, and the addition of fins was found to reduce this resistance.

Full simulation of the coolant flow field was performed in Cases A and F-I, and estimates were made for the condenser side heat transfer coefficients based on bulk fluid properties. As a result of the varying heat transfer coefficient in the case of channel flow, larger variations were observed from the empirical correlations of the overall resistances.

Case F used an un-finned heat pipe with a constant heat input and channel flow cooling (heat pipe and flow properties listed in Table 1). The simulation was then repeated with 6 external condenser fins (Case G). Case 5 G showed the largest disagreement in pressure drop with the similarity solution (Figure 14b), of any case (700 Pa at maximum). This is attributed to the Mach number of the heat pipe being greater than 1 and internal vapor velocity surpassing the sonic limit.

A heat pipe with convective heat input and channel flow cooling was simulated (Case H) and the simulation was repeated with 6 condenser fins (Case I). The condenser fins were found to

decrease the average wall temperature (30 K), however, the amount of heat transfer was only increased slightly (11%).

The variation in wall temperature from the heat pipe leading-to-trailing edge was small for all cases; less than 5% of the heat pipe overall temperature drop (Figure 13). A comparison between the un-finned heat pipes with constant heat input (Cases 5 C), and fully simulated channel flow cooling (Case 5 F), yielded a variation of approximately 12% of the overall system thermal resistance. The heat pipe with constant heating and convective cooling with fins (Case C) was found to have a lower thermal resistance than without fins (Case B) by about 17%. In addition, the heat pipe with channel flow cooling was found to have a decreased thermal resistance by approximately 8% from the heat pipe without fins (Case G). This decrease in fin effectiveness, seen between the two finned cases under constant heat input, may be a result of the fin interaction with the coolant flow. The coolant flow is slowed and the temperature is increased, thus lowering the local heat transfer coefficient. The thermal resistance due to the external hot and cold working fluid at the evaporator/ condenser wall were the greatest thermal resistances due to the large temperature drop, between the heat pipe wall and fluid. The largest internal resistances were those of the heat pipe wall and wick, due to the low thermal conductivity of each. In Case 5 C, E and G, it was shown that the vapor core thermal resistance was not negligible (as it was in other cases) due to a higher vapor temperature drop, because of the addition of fins. However, the temperature of the heat pipe outer wall was greatly reduced on the condenser side, which decreased the thermal resistance of the system. The resistances of the wick-vapor interface were also significant in Case 5 G due to the high centerline Mach number which causes viscous heating on the boundary and an increased end-to-end temperature difference.

7. Conclusion

A working model was developed to simulate high and low temperature heat pipe operation for both transient and steady state modes of operation. In addition, the single domain conjugate problem of coolant flow around a conventional cylindrical heat pipe was also solved without empirical correlations and the dominant thermal resistances were identified. It was proven that in high temperature heat pipe applications, the addition of fins can increase the thermal resistance of the vapor core, due to an increase in the vapor core temperature drop, and thus may be of higher design concern. In lower temperature applications, it was shown that the vapor core temperature does not increase significantly; thus the thermal resistance through the vapor can be neglected.

Acknowledgement

This material is based upon work supported by the National Science Foundation under Grant Nos. 1435233 (University of Connecticut) and 1435131 (University of Kansas).

References

[1] H. Shabgard, M. J. Allen, N. Sharifi, S. P. Benn, A. Faghri, and T. Bergman, "Heat Pipe Heat Exchangers and Heat Sinks: Opportunities, Challenges, Applications, Analysis, and State of the Art," *International Journal of Heat and Mass Transfer*, vol. 89, no. 2015, pp. 138–158, 2015.

[2] A. Faghri, "Review and Advances in Heat Pipe Science and Technology," *Journal of Heat Transfer*, vol. 134, no. 12. p. 123001, 2012.

[3] W. G. Anderson and C. Tarau, "Variable Conductance Heat Pipes for Radioisotope Stirling Systems," in *AIP Conference Proceedings*, 2008, vol. 969, pp. 679–688.

[4] Y. Cao and A. Faghri, "Transient Two-Dimensional Compressible Analysis for High-Temperature Heat Pipes with Pulsed Heat Input," *Numerical Heat Transfer, Part A: Applications*, vol. 18, no. 4. pp. 483–502, 1991.

[5] J. A. Rice and A. Faghri, "Analysis of Screen Wick Heat Pipes, Including Capillary Dry-Out Limitations," *Journal of Thermophysics and Heat Transfer*, vol. 21, no. 3. pp. 475–486, 2007.

[6] A. Faghri and M. Buchko, "Experimental and Numerical Analysis of Low-Temperture Heat Pipes with Multiple Heat Souces," *Journal of Heat Transfer*, vol. 113, pp. 728–734, 1991.

[7] R. Ranjan, J. Y. Murthy, S. V. Garimella, and U. Vadakkan, "A Numerical Model for Transport in Flat Heat Pipes Considering Wick Microstructure Effects," *International Journal of Heat and Mass Transfer*, vol. 54, no. 1–3, pp. 153–168, 2011.

[8] Z. J. Zuo and A. Faghri, "A Network Thermodynamic Analysis of the Heat Pipe," *International Journal of Heat and Mass Transfer*, vol. 41, no. 11, pp. 1473–1484, 1998.

[9] B. Xiao and A. Faghri, "A Three-Dimensional Thermal-Fluid Analysis of Flat Heat Pipes," *International Journal of Heat and Mass Transfer*, vol. 51, no. 11–12, pp. 3113–3126, 2008.

[10] T. Kaya and J. Goldak, "Three-Dimensional Numerical Analysis of Heat and Mass Transfer in Heat Pipes," *Heat Mass Transfer*, vol. 43, pp. 775–785, 2007.

[11] U. Vadakkan, S. V. Garimella, and J. Y. Murthy, “Transport in Flat Heat Pipes at High Heat Fluxes From Multiple Discrete Sources,” *Journal of Heat Transfer*, vol. 126, no. 3. p. 347, 2004.

[12] A. Faghri, A. Zhang, and J. Howell, *Advanced Heat and Mass Transfer*. Global Digital Press, 2010.

[13] A. Faghri, *Heat Pipe Science and Technology*, 2nd ed. Global Digital Press, 2016.

[14] T. Bergman, P. Lavine, F. Incropera, and D. Dewitt, *Fundamentals of Heat and Mass Transfer*, 7th ed. Hoboken: John Wiley and Sons, 2011.

[15] S. Patankar, “Numerical Heat Transfer and Fluid Flow,” in *Series in Computational Methods in Mechanics and Thermal Sciences*, 1980, pp. 1–197.

[16] M. Ivanovskii, V. Sorokin, and I. Yagodin, *The Physical Principles of Heat Pipes*. Oxford University Press, 1982.

[17] A. Faghri, “Performance Characteristics of a Concentric Annular Heat Pipe, Part II, Vapor Flow Analysis,” *ASME Journal of Heat Transfer*, vol. 111, no. 4, pp. 851–857, 1989.

List of Figures

Figure 1 Heat pipe elements and configuration for a conventional cylindrical heat pipe 19
Figure 2 Heat pipe thermal network used to calculate R_{hp}.....20
Figure 3 Case 1: numerical results compared to previous studies 21
Figure 4 Centerline temperature vs length for Case 2 A 22
Figure 5 Centerline vapor temperature vs length for Case 2 B.....23
Figure 6 Pressure drop vs length for Case 2 (HTHP pulsated heat input) 24
Figure 7 Case 3 LTHP: wall temperature vs length 25
Figure 8 Case 3 LTHP: pressure drop vs length 26
Figure 9 Top view of the solution domain for a heat pipe under channel flow cooling.....27
Figure 10 Case 4 Wall temperature vs length 28
Figure 11 Case 5 HTHP temperature vs length 29
Figure 12 Case 5 HTHP centerline vapor pressure drop vs length 30
Figure 13 Case 5 F-I channel flow cooling temperature vs length 31
Figure 14 Case 5 F-I channel flow cooling pressure drop vs length 32

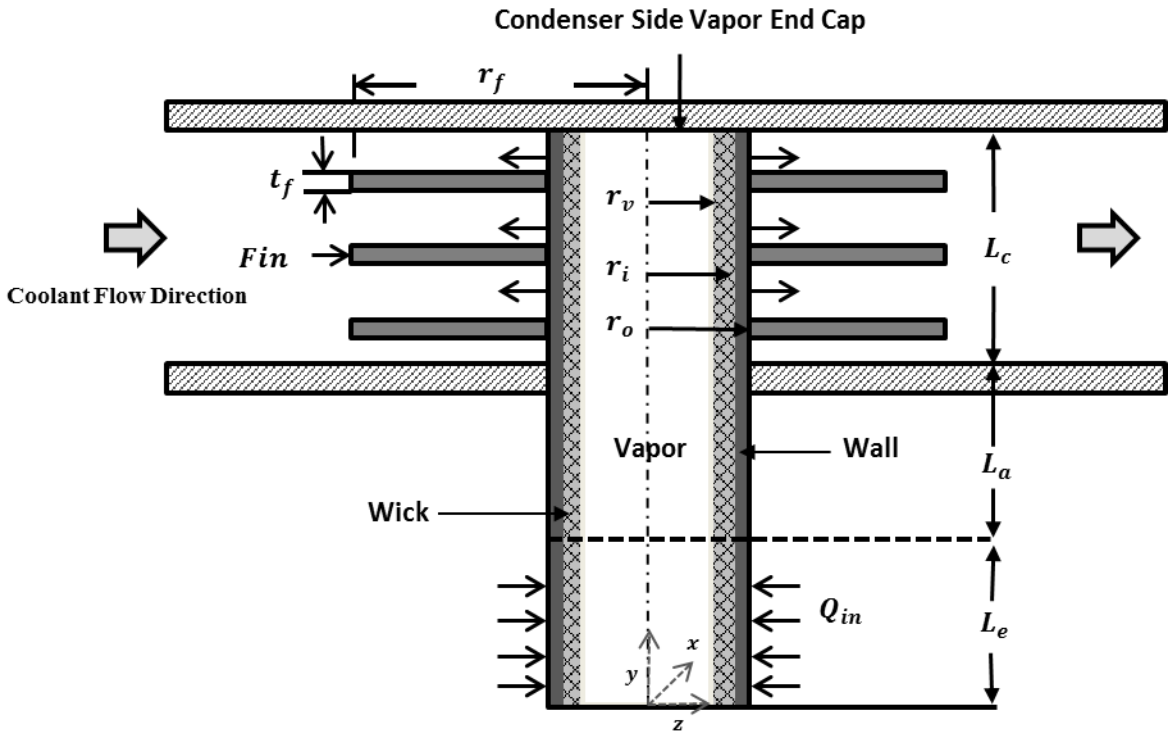

Figure 1 *Heat pipe elements and configuration for a conventional vertical cylindrical heat pipe with channel flow across the condenser section.*

$\boldsymbol{R_{(e/c),ex}}$: External thermal resistance due to heat source / heat sink

$\boldsymbol{R_{(e/c),w}}$: Radial thermal resistance due to conduction through the evaporator/ condenser wall

$\boldsymbol{R_{(e/c),wk}}$: Radial thermal resistance due to conduction through the evaporator/condenser wick

$\boldsymbol{R_{(e/c),inter}}$: Radial thermal resistance due to convection at the evaporator/condenser interface

$\boldsymbol{R_v}$: Axial resistance due to the vapor

$\boldsymbol{R_{a,w}}$: Axial conduction through adiabatic wall

$\boldsymbol{R_{a,wk}}$: Axial conduction through adiabatic wick

$\boldsymbol{R_{c,f}}$: External resistance from fins to coolant

Note: if fins are added an equivalent resistance must be placed on the condenser surface such that $\frac{1}{R_{c,eff}} = \frac{1}{R_{c,w}} + \frac{1}{R_{c,f}}$

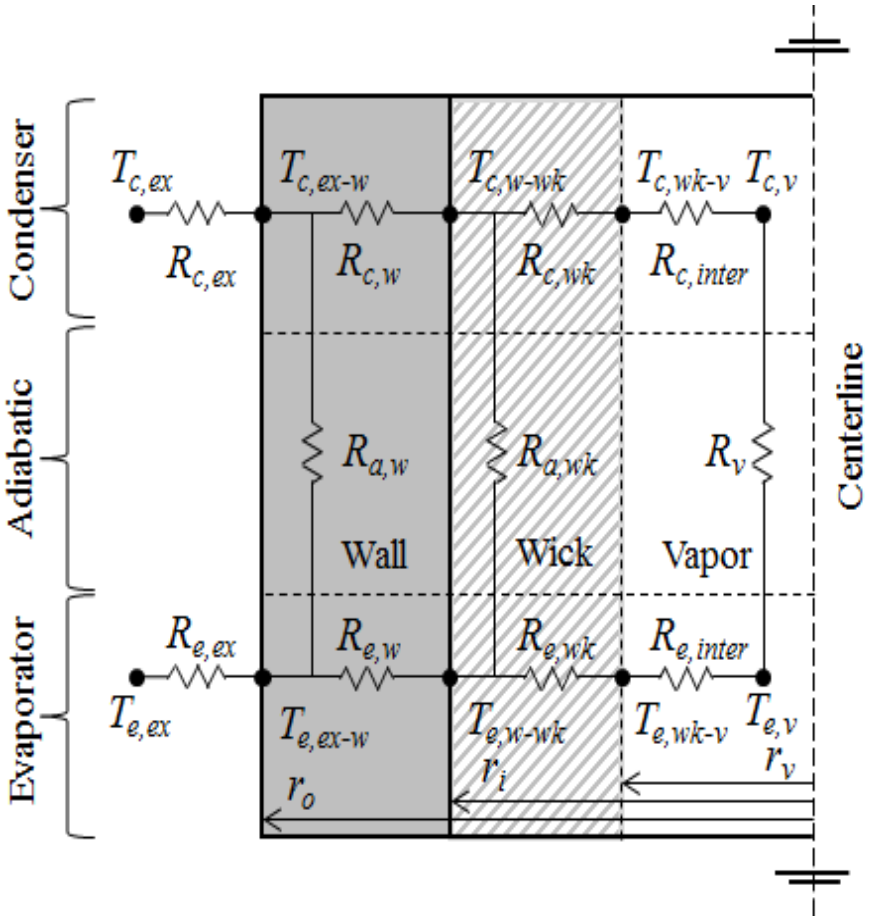

Figure 2 *Heat pipe thermal network used to calculate R_{hp}.*

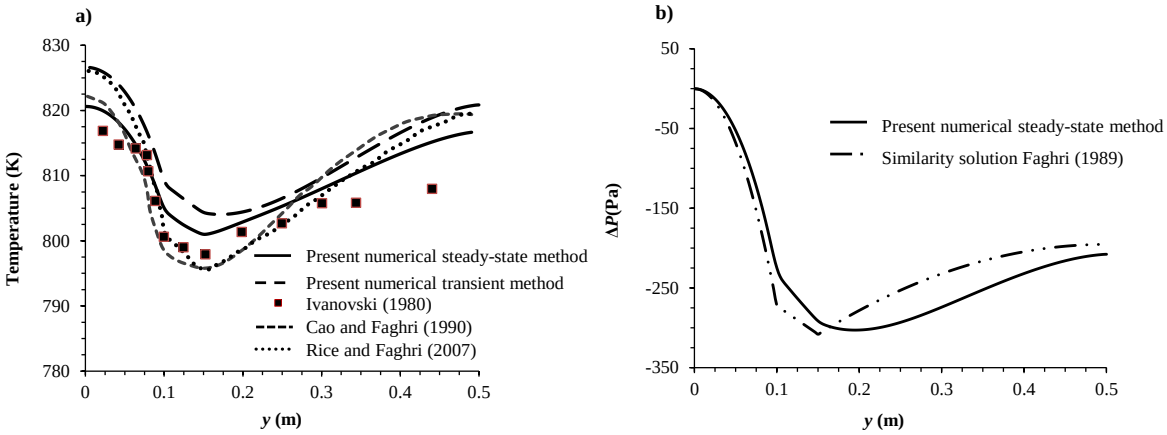

Figure 3 *Case 1: Numerical results compared to previous studies* ***a)*** *centerline vapor temperature vs. length* ***b)*** *centerline vapor pressure drop vs. length.*

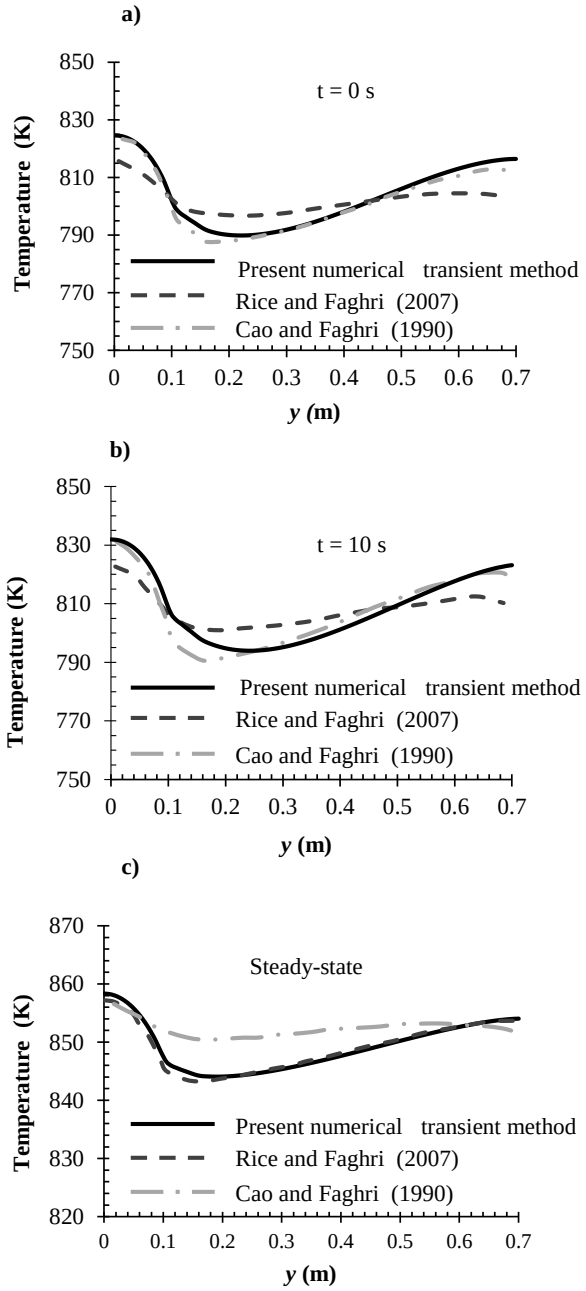

Figure 4 *Centerline temperature vs. length for Case 2 A (HTHP pulsated heat input, radiative cooling) at multiple intervals steps* ***a)*** *t=0 seconds after heat input increase* ***b)*** *t=10 seconds after heat input increase* ***c)*** *steady-state* $\left(Q_e = Q_c\right)$.

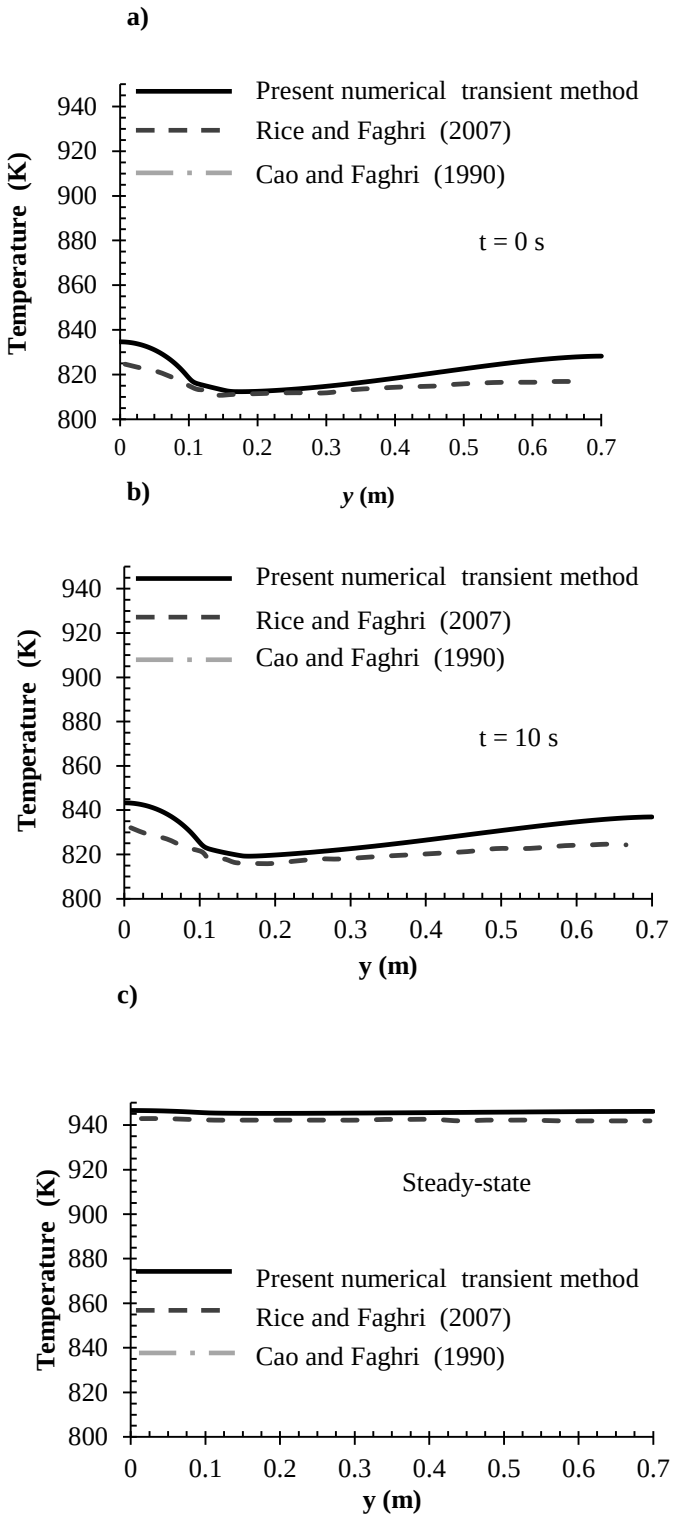

Figure 5 *Centerline vapor temperature vs. length for Case 2 B (HTHP pulsated heat input, convective cooling) at multiple time intervals* ***a)*** *t=0 seconds after heat input increase* ***b)*** *t=10 seconds after heat input increase* ***c)*** *steady-state* $\left(Q_e = Q_c\right)$.

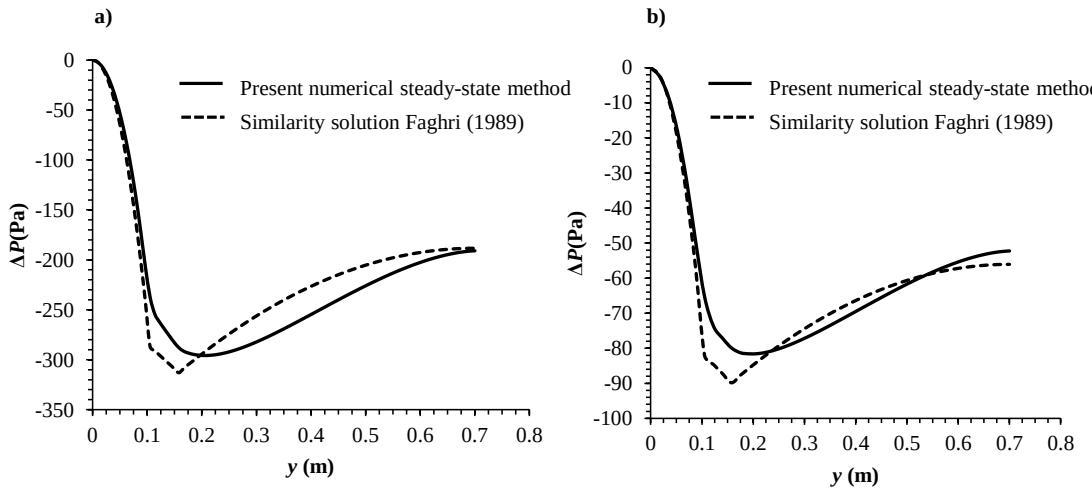

Figure 6 *Pressure drop vs. length for Case 2 (HTHP pulsated heat input)* ***a)*** *Case 2 A steady state radiative cooling* ***b)*** *Case 2 B steady state convective cooling.*

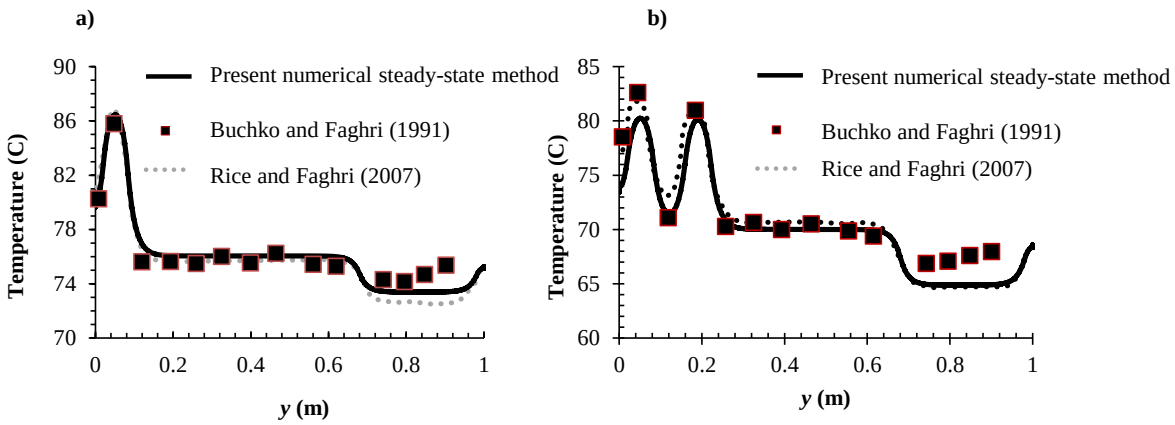

Figure 7 *Case 3 (LTHP): wall temperature vs. length* ***a)*** *Case 3 A: with evaporator 1 active, 97 W* ***b)*** *Case 3 B: with evaporators 1 and 2 active, 98 W each.*

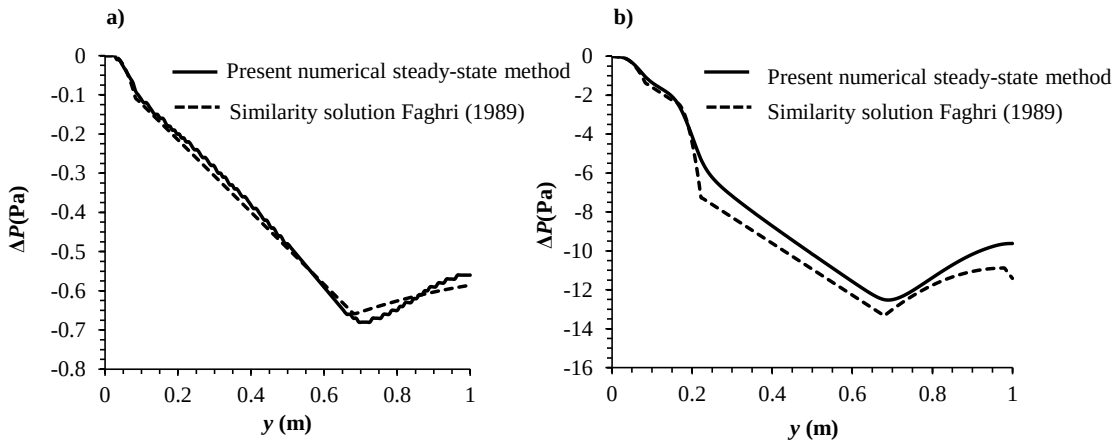

Figure 8 *Case 3 (LTHP): pressure drop vs. length* ***a)*** *Case 3 A: with evaporator 1 active, 97 W* ***b)*** *Case 3 B: with evaporators 1 and 2 active, 98 W each.*

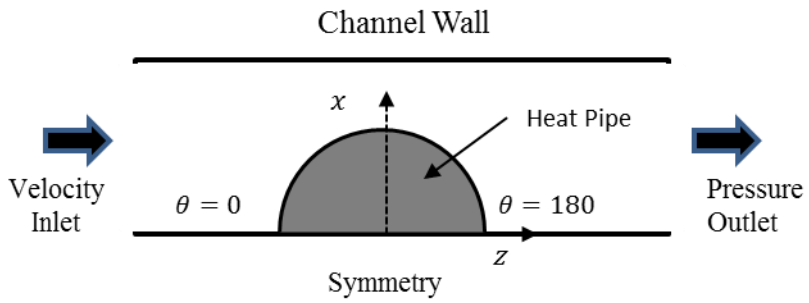

Figure 9 S*olution domain (in the xz plane) for a heat pipe with channel flow cooling.*

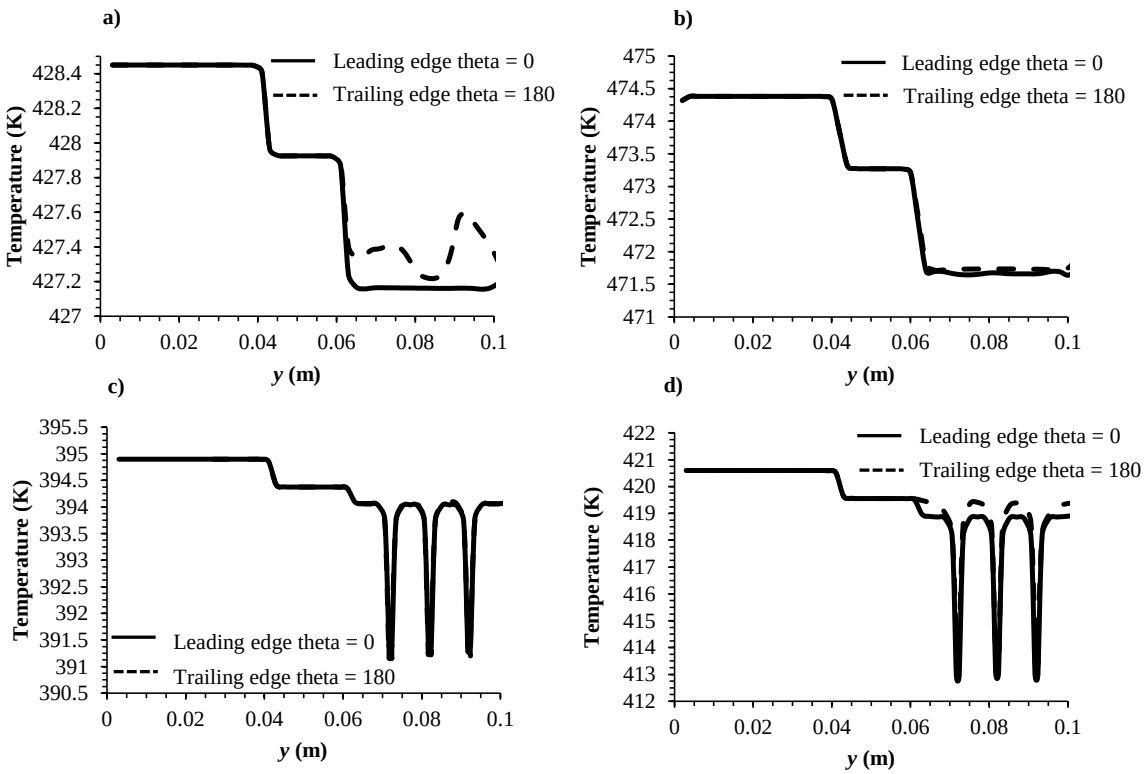

Figure 10 *Case 4: Wall temperature vs. length **a)** Case 4 A: 10 W heat input without fins **b)** Case 4 B: 20 W heat input without fins **c)** Case 4 C: 10 W heat input with 3 condenser fins **d)** Case 4 D: 20 W heat input with 3 condneser fins.*

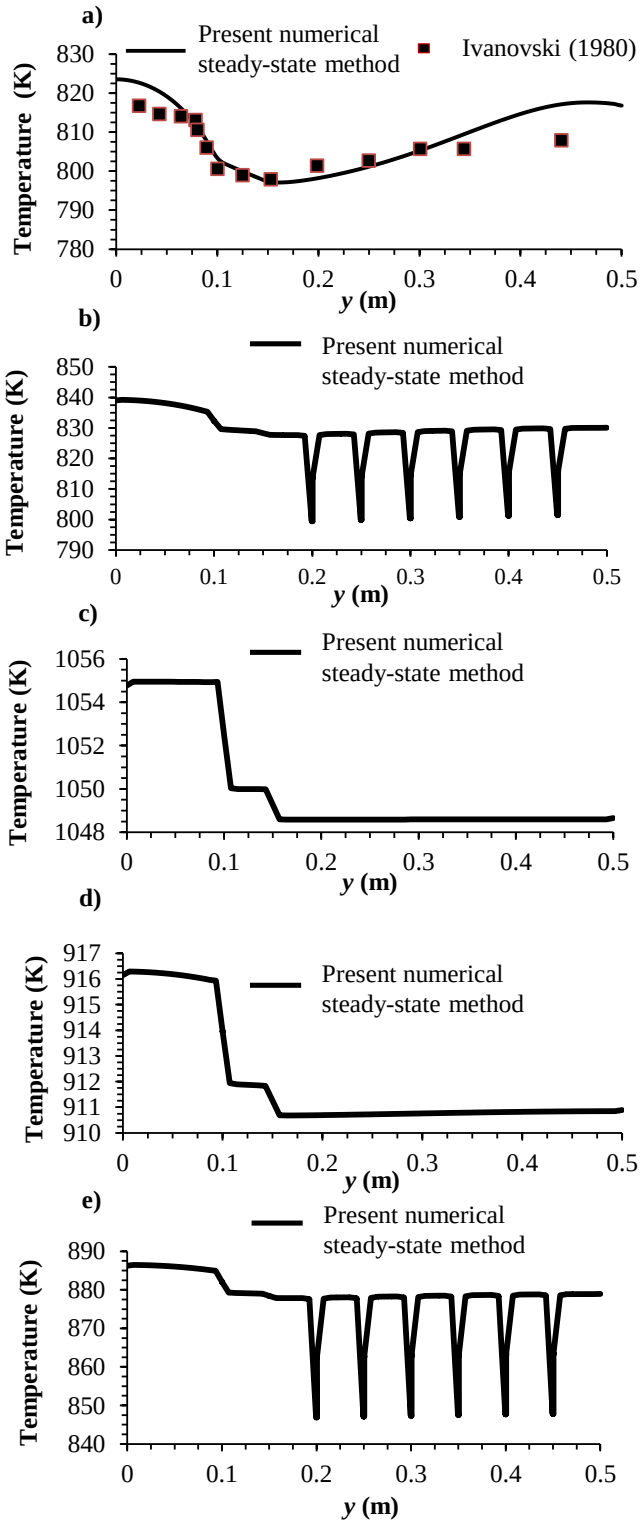

Figure 11 *Case 5 (HTHP) Length vs. centerline vapor temperature for:* ***a)*** *Case 5 A: Channel flow cooling, length vs. wall temperature for:* ***b)*** *Case 5 B constant heat input with fins* ***c)*** *Case 5 C constant heat input without fins* ***d)*** *Case 5 D convective heat input without fins* ***e)*** *Case 5 E convective heat input with fins.*

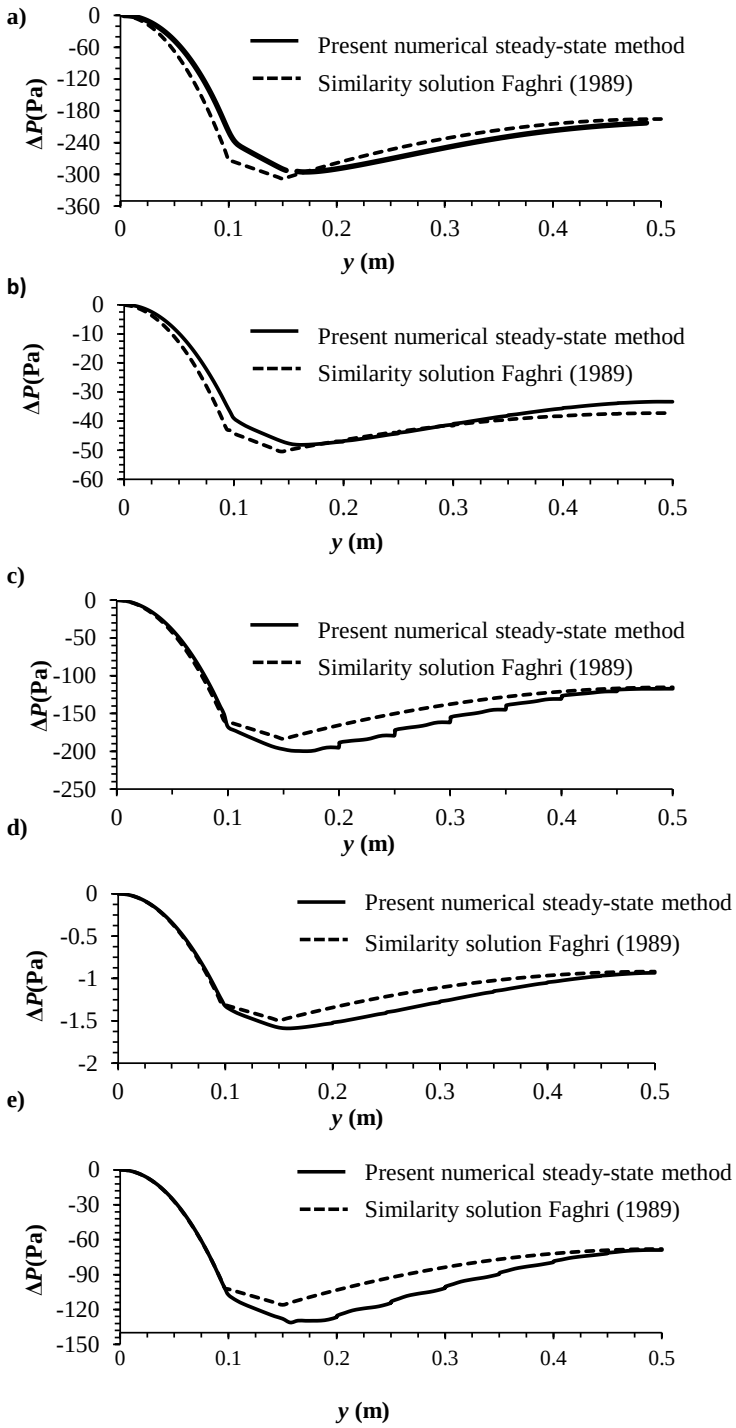

Figure 12 *Case 5 (HTHP) Centerline vapor pressure drop vs. length* ***a)*** *Case 5 A channel flow cooling* ***b)*** *Case 5 B constant heat input with fins* ***c)*** *Case 6 C constant heat input without fins* ***d)*** *Case 5 D convective heat input without fins* ***e)*** *Case 5 E convective heat input with fins.*

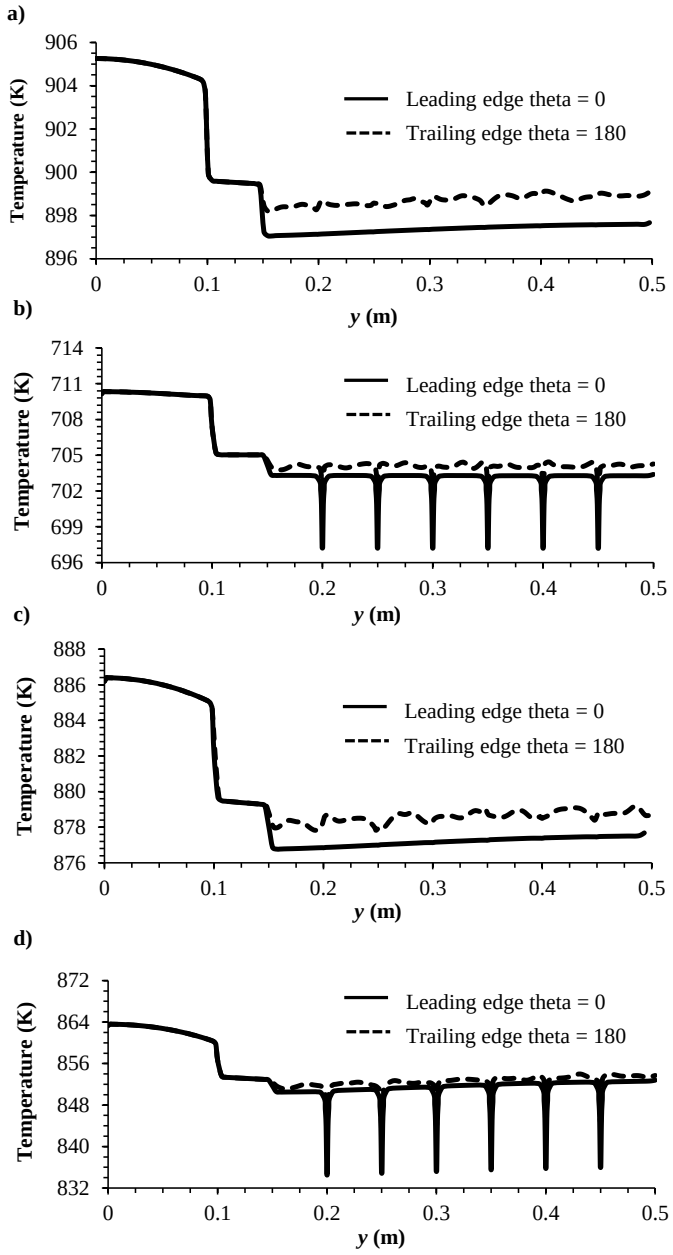

Figure 13 *Case 5 F-I: Channel flow cooling temperature vs. length* ***a)*** *Case 5 F constant heat input no fins* ***b)*** *Case 5 G constant heat input 6 fin)* ***c)*** *Case 5 H convective heat input, no fins* ***d)*** *Case 5 I convective input, 6 fins.*

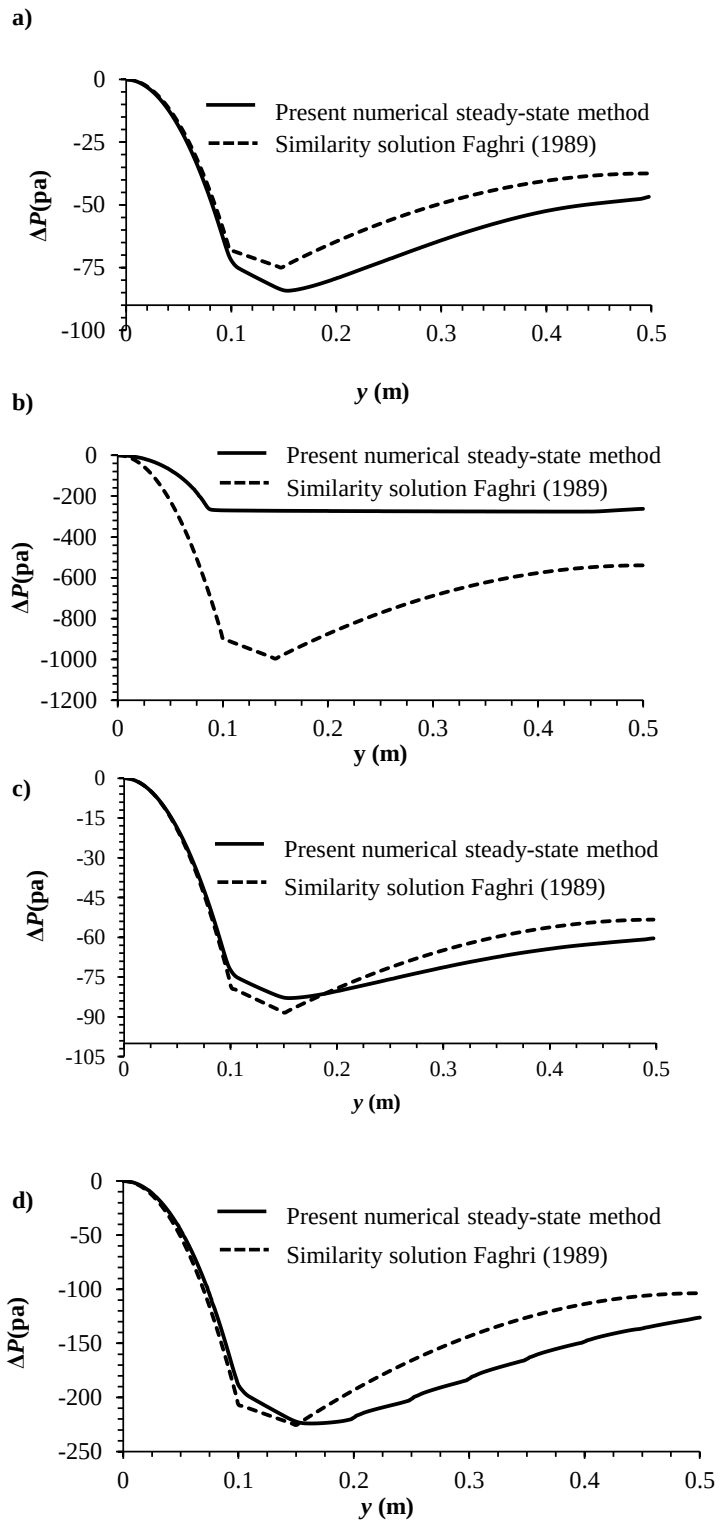

Figure 14 *Case 5 F-I: Channel flow cooling pressure drop vs. length* ***a)*** *Case 5 F constant heat input no fins* ***b)*** *Case 5 G constant heat input 6 fins* ***c)*** *Case 5 H convective heat input, no fins* ***d)*** *Case 5 I convective input, 6 fins.*

List of Tables

Table 1 Thermal resistance network definitions and correlations 34
Table 2 Heat pipe, properties, dimensions and operating conditions for five the five case simulated 35
Table 3 HTHP resistances for Case 1 and Case 2 36
Table 4 LTHP thermal resistances for Case 3 37
Table 5 LTHP with channel flow cooling thermal resistances for Case 4 38
Table 6 HTHP thermal resistances for Case 5 A-E 39
Table 7 HTHP with channel flow cooling thermal resistances for Case 5 F-I 40

Table 1 *Thermal resistance network definitions and correlations*

Equation #	Resistance	Numerical (a)	Analytical/Empirical (b)
(20)	$R_{e,ex}$	$\frac{T_{e,ex}-T_{e,ex-w}}{Q_{e,ex}}$	convection: $\frac{1}{A_{e,o}\boldsymbol{h}^*}$
(21)	$R_{c,ex}$	$\frac{T_{c,ex}-T_{c,ex-w}}{Q_{c,ex}}$	convection: $\frac{1}{A_{c,o}\boldsymbol{h}^*}$ radiation: $\frac{1}{A_{c,o}\left(\varepsilon\sigma\left(T_{c,ex}{}^2+T_{sur}{}^2\right)\left(T_{c,ex}+T_{sur}\right)\right)}$
(22)	$R_{e,w}$	$\frac{T_{e,ex-w}-T_{e,w-wk}}{Q_{e,w}}$	$\frac{\ln\left(r_o/r_i\right)}{2\pi k_w L_e}$
(23)	$R_{e,wk}$	$\frac{T_{e,w-wk}-T_{e,wk-v}}{Q_{e,wk}}$	$\frac{\ln\left(r_i/r_v\right)}{2\pi k_{wk} L_e}$
(24)	$R_{e,\mathrm{inter}}$	$\frac{T_{e,wk-v}-T_{e,v}}{Q_{e,\mathrm{inter}}}$	$\frac{1}{A_{e,i}\left(\frac{2\alpha}{2-\alpha}\right)\left(\frac{h_{fg}{}^2\rho_v}{T_v}\right)\sqrt{\frac{1}{2\pi R_g T_v}}\left(1-\frac{p_v}{2\rho_v h_{fg}}\right)}$
(25)	R_v	$\frac{T_{e,v}-T_{c,v}}{Q_v}$	$\frac{8\mathrm{R}_g\mu_v T_v^2}{\pi h_{fg}^2 P_v\rho_v}\left[\frac{\left(L_c+L_e\right)/2+L_a}{r_i^4}\right]$
(26)	$R_{c,\mathrm{inter}}$	$\frac{T_{c,v}-T_{c,wk-v}}{Q_{c,\mathrm{inter}}}$	$\frac{1}{A_{c,i}\left(\frac{2\alpha}{2-\alpha}\right)\left(\frac{h_{fg}{}^2\rho_v}{T_v}\right)\sqrt{\frac{1}{2\pi R_g T_v}}\left(1-\frac{p_v}{2\rho_v h_{fg}}\right)}$
(27)	$R_{c,wk}$	$\frac{T_{c,wk-v}-T_{c,w-wk}}{Q_{c.wk}}$	$\frac{\ln\left(r_i/r_v\right)}{2\pi k_{wk} L_c}$
(28)	$R_{c,w}$	$\frac{T_{c,wk-w}-T_{c,ex-w}}{Q_{c,w}}$	$\frac{\ln\left(r_o/r_i\right)}{2\pi k_w L_c}$
(29)	$R_{a,w}$	$\frac{T_{e,ex-w}-T_{c,ex-w}}{Q_{a,w}}$	$\frac{L_a}{\pi k_w\left(r_o{}^2-r_i{}^2\right)}$
(30)	$R_{a,wk}$	$\frac{T_{e,w-wk}-T_{c,w-wk}}{Q_{a,wk}}$	$\frac{L_a}{\pi k_{wk}\left(r_i^2-r_v{}^2\right)}$

* The heat transfer coefficient is assumed in the case of a constant convection boundary but calculated from flow properties in the case of channel flow cooling. In most cases the adiabatic thermal resistances were neglected since they are large and do not impede the phase change of the working fluid which is the area of interest.

** Equation letter *(a)* denotes the numerical while *(b)* denotes analytical/empirical.

Table 2 *Heat pipe, properties, dimensions and operating conditions for Cases 1-5*

	Case 1: HTHP steady state operation	**Case 2:** HTHP stepped heat input	***Case 3:*** LTHP validation	**Case 4:** LTHP channel flow cooling	**Case 5:** HTHP with and without channel flow cooling
Property /dimension	Value				
Working fluid	Sodium	Sodium	Water	Water	Sodium
k_v (W/mK)	0.0406	0.0406	0.02161	0.0261	0.0406
μ_v (N-s/m^2)	2.01e-5	2.01e-5	1.34e-05	1.34e-05	2.01e-5
h_{fg} (kJ/kg)	4131	4131	2256	2256	4131
r_v (m)	0.0070	0.0070	0.01025	0.0040	0.0070
r_i (m)	0.0075	0.0080	0.01100	0.0045	0.0075
r_o (m)	0.0085	0.0090	0.01270	0.0050	0.0085
L_e (m)	0.1000	0.1050	0.06350	0.0400	0.100
Heater starting locations e1 (m) e2 (m) e3 (m) e4 (m)	NA	NA	0.0200 0.1588 0.2976 0.4364	NA	NA
L_a (m)	0.05	0.0525	NA	0.0200	0.050
L_c (m)	0.35	0.5425	0.30000	0.0400	0.350
Condenser starting location (m)	NA	NA	0.68	NA	NA
Wall	NA	Stainless steel	Copper	Stainless steel	Stainless Steel
k_w (W/mK)	35	21.7	387.6	16	35
$\rho_{w/wk}$ (kg/m^3)	8030	8030	8978	8030	8030
$cp_{w/wk}$ (kJ/kgK)	502.48	502.48	381	508	502.48
k_{wk} (W/mK)	35	45	1.38	16	35
Fin material	NA	NA	NA	Aluminum	Aluminum
r_f (m)	NA	NA	NA	0.015	0.015
k_f (W/mK)	NA	NA	NA	16	16
ρ_f (kg/m^3)	NA	NA	NA	8030	8030
cp_f (kJ/kgK)	NA	NA	NA	508	508
Heat input	Constant heat rate: 560 W	Constant heat rate: Initial input 623 W Step increase 770 W	Constant heat rate: Case 3 A: e1: 97 W Case 3 B: e1: 98 W e2: 98W	Constant heat rate: Cases 4 A.C: 10 W Cases 4 B,D :20 W	Constant heat rate: Cases 5 A,B,C,F,G 560 W Convective input: Cases 5 D, E,H,I T_∞ =1000 K **h** =1000 W/m^{2}K
Heat output	Convection coefficient: (58.5 W/m^{2}K) T_∞ =300 K	Radiation: Case 2 A T_{ref} =0 K ε = 0.85 Convection: Case 2 B 39 W/m^{2}K T_∞ =300 K	Constant heat sink	No Fins: Cases 4 A, C Fins: Cases 4 B, D Channel flow: All Cases Inlet velocity 10 m/s Inlet temperature 373 K	No Fins: Cases 5 A, B, D, F, H Fins: Cases 5 C, E, G, I Channel flow: Inlet velocity Case 5 A: 5.13 m/s Cases 5 F,G,H,I: 3 m/s Convection: Cases 5 B,C,D,E T_∞ =300 K **h** =40 W/m^{2}K

Table 3 *HTHP resistances for Case 1 & Case 2*

Case 1: HTHP under steady state operation

Resistance (W/K)	***Re,w***	***Re,wk***	***Re,inter***	***Rv***	***Rc,w***	***Rc,wk***	***Rc,inter***	***Rc,ex***	***Rhp***	***Rtot***
Empirical/analytical	5.69E-03	3.14E-03	2.56E-03	1.30E-02	1.63E-03	8.96E-04	7.31E-04	0.915	2.82E-02	0.943
Numerical	5.64E-03	3.10E-03	2.41E-03	1.05E-02	1.61E-03	8.89E-04	1.03E-03	0.919	2.52E-02	0.944
% Difference	<1%	~1%	6%	19%	<1%	<1%	41%	<1%	11%	<1%
Heat input (W)							560			

Case 2 A: HTHP with pulsated heat input and radiative cooling at steady-state operation

Resistance (W/K)	***Re,w***	***Re,wk***	***Re,inter***	***Rv***	***Rc,w***	***Rc,wk***	***Rc,inter***	***Rc,ex***	***Rhp***	***Rtot***
Empirical/Analytical	8.23E-03	4.50E-03	7.32E-04	3.88E-03	1.59E-03	8.71E-04	1.42E-04	0.714	1.99E-02	0.734
Numerical	8.18E-03	4.47E-03	1.28E-03	3.95E-03	1.58E-03	8.66E-04	2.69E-04	0.715	2.06E-02	0.735
% Difference	<1%	<1%	75%	5%	<1%	<1%	90%	<1%	3%	<1%
Heat input (W)							770			

Case 2 B: HTHP with pulsated heat input and convective cooling at steady-state operation

Resistance (W/K)	***Re,w***	***Re,wk***	***Re,inter***	***Rv***	***Rc,w***	***Rc,wk***	***Rc,inter***	***Rc,ex***	***Rhp***	***Rtot***
Empirical/analytical	8.23E-03	4.50E-03	2.41E-04	3.49E-04	1.59E-03	8.71E-04	4.66E-05	0.836	1.58E-02	0.852
Numerical	8.19E-03	4.47E-03	1.86E-04	3.56E-04	1.58E-03	8.66E-04	7.44E-05	0.838	1.57E-02	0.854
% Difference	<1%	<1%	23%	2%	<1%	<1%	60%	<1%	<1%	<1%
Heat input (W)							770			

Table 4 *LTHP thermal resistances for Case 3*

Case 3 A: LTHP one heat source input

Resistance (W/K)	***Re1,w***	***Re1,wk***	***Re1,inter***	***Rv***	***Rc,w***	***Rc,wk***	***Rc,inter***	***Rhp***
Empirical/analytical	1.06E-03	1.28E-01	3.42E-05	2.64E-06	2.25E-04	2.71E-02	7.24E-06	2.74E-02
Numerical	9.05E-04	9.32E-02	3.06E-07	1.63E-06	2.16E-04	2.53E-02	6.12E-07	2.56E-02
% Difference	15%	27%	99%	38%	4%	7%	92%	7%
Heat input (W)							97	

Case 3 B: LTHP two heat source inputs

Resistance (W/K)	***Re1,w***	***Re1,wk***	***Re1,inter***	***Re2,w***	***Re2,wk***	***Re2,inter***	***Rv***	***Rc,w***	***Rc,wk***	***Rc,inter***
Empirical/analytical	9.45E-04	1.28E-01	3.91E-05	9.45E-04	1.28E-01	3.91E-05	2.85E-05	9.45E-04	1.28E-01	3.60E-05
Numerical	9.11E-04	9.40E-02	3.31E-05	9.02E-04	9.20E-02	2.34E-04	1.09E-04	9.02E-04	9.20E-02	2.34E-04
% Difference	4%	27%	15%	5%	28%	>300%	283%	5%	28%	>300%
Heat input (W)							196			

Table 5 LTHP with channel flow cooling thermal resistances for Case 4

Case 4 A: LTHP channel flow cooling with a 10 W heat input and without fins

Resistance (W/K)	***Re,w***	***Re,wk***	***Re,inter***	***Rv***	***Rc,w***	***Rc,wk***	***Rc,inter***	***Rc,ex,w***	***Rhp***	***Rtot***
Empirical/analytical	2.62E-02	2.93E-02	1.87E-05	1.03E-04	2.62E-02	2.93E-02	1.87E-05	5.99	1.09E-01	6.1
Numerical	2.61E-02	2.91E-02	1.93E-04	1.06E-03	2.60E-02	2.90E-02	1.25E-03	5.34	1.12E-01	5.45
% Difference	<1%	<1%	>300%	>300%	<1%	1%	>300%	11%	3%	11%
Heat input (W)	10									

Case 4 B: LTHP channel flow cooling with a 20 W heat input and without fins

Resistance (W/K)	***Re,w***	***Re,wk***	***Re,inter***	***Rv***	***Rc,w***	***Rc,wk***	***Rc,inter***	***Rc,ex,w***	***Rhp***	***Rtot***
Empirical/analytical	2.62E-02	2.93E-02	9.33E-06	2.10E-05	2.62E-02	2.93E-02	9.33E-06	5.99	1.09E-01	6.1
Numerical	2.61E-02	2.91E-02	7.43E-04	5.66E-04	2.59E-02	2.89E-02	1.80E-04	5.01	1.11E-01	5.12
% Difference	<1%	<1%	>300%	>300%	<1%	1%	>300%	16%	2%	16%
Heat input (W)	20									

Case 4 C: LTHP channel flow cooling with a 10 W heat input and fins

Resistance (W/K)	***Re,w***	***Re,wk***	***Re,inter***	***Rv***	***Rc,w***	***Rc,wk***	***Rc,inter***	***Rc,ex,w***	***Rc,ex,f***	***Rhp***	***Rtot***
Empirical/analytical	2.62E-02	2.93E-02	3.83E-05	4.80E-07	2.62E-02	2.93E-02	3.83E-05	6.47	1.86	1.09E-01	1.55
Numerical	2.61E-02	2.90E-02	1.46E-04	5.99E-04	5.01E-03	2.88E-02	7.48E-04	5.96	2.77	9.01E-02	1.98
% Difference	<1%	<1%	281%	>300%	81%	2%	>300%	8%	49%	18%	28%
Heat input (W)	10	Heat output from wall (W)		4	Heat output from fins (W)			6			

Case 4 D: LTHP channel flow cooling with a 20 W heat input and fins

Resistance (W/K)	***Re,w***	***Re,wk***	***Re,inter***	***Rv***	***Rc,w***	***Rc,wk***	***Rc,inter***	***Rc,ex,w***	***Rc,ex,f***	***Rhp***	***Rtot***
Empirical/analytical	2.62E-02	2.93E-02	1.93E-05	1.20E-07	2.62E-02	2.93E-02	1.93E-05	6.47	1.86	1.09E-01	1.55
Numerical	2.61E-02	2.91E-02	1.35E-05	5.20E-05	2.61E-02	2.92E-02	6.70E-05	6.84	2.88	1.10E-01	2.14
% Difference	<1%	<1%	30%	>300%	<1%	<1%	246%	6%	55%	<1%	38%
Heat input (W)	20	Heat output from wall (W)		7	Heat output from fins (W)			13			

Table 6 *HTHP thermal resistances for Case 5 A-*

Case 5A Constant heat input with channel flow cooling and no fins

Resistance (W/K)	***Re,w***	***Re,wk***	***Re,inter***	***Rv***	***Rc,w***	***Rc,wk***	***Rc,inter***	***Rc,ex,w***	***Rhp***	***Rtot***
Empirical/analytical	5.69E-03	3.14E-03	1.57E-03	2.19E-02	1.63E-03	8.96E-04	6.25E-04	3.52E-02	9.15E-01	9.50E-01
Numerical	5.56E-03	3.10E-03	4.04E-03	1.26E-02	1.73E-03	9.67E-04	5.00E-04	3.30E-02	9.25E-01	9.58E-01
% Difference	2%	1%	61%	74%	6%	7%	88%	7%	1%	1%
Heat input (W)						562				

Case 5 B: Constant heat input with convective cooling and no fins

Resistance (W/K)	***Re,w***	***Re,wk***	***Re,inter***	***Rv***	***Rc,w***	***Rc,wk***	***Rc,inter***	***Rc,ex,w***	***Rhp***	***Rtot***
Empirical/analytical	5.69E-03	3.14E-03	1.02E-04	3.58E-05	1.63E-03	8.96E-04	2.91E-05	1.36	1.15E-02	1.35
Numerical	5.45E-03	3.02E-03	1.04E-05	3.28E-05	1.60E-03	8.87E-04	1.03E-05	1.36	1.10E-02	1.35
% Difference	4%	4%	90%	8%	1%	1%	64%	<1%	4%	<1%
Total heat input (W)							562			

Case 5 C: Constant heat input with convective cooling and 6 condenser fins

Resistance (W/K)	***Re,w***	***Re,wk***	***Re,inter***	***Rv***	***Rc,w***	***Rc,wk***	***Rc,inter***	***Rc,ex,w***	***Rc,ex,f***	***Rhp***	***Rtot***
Empirical/analytical	5.69E-03	3.14E-03	1.69E-03	9.72E-03	1.63E-03	8.96E-04	4.84E-04	1.36	2.84	2.32E-02	9.43E-01
Numerical	5.85E-03	3.07E-03	2.10E-03	6.46E-03	1.53E-03	8.80E-04	6.01E-04	1.36	2.84	2.05E-02	9.43E-01
% Difference	3%	2%	24%	34%	6%	2%	24%	<1%	<1%	12%	<1%
Heat input (W)								562			

Case 5 D: Convective heat input with convective cooling and no fins

Resistance (W/K)	***Re,ex***	***Re,w***	***Re,wk***	***Re,inter***	***Rv***	***Rc,w***	***Rc,wk***	***Rc,inter***	***Rc,ex,w***	***Rhp***	***Rtot***
Empirical/analytical	1.87E-01	5.69E-03	3.14E-03	4.33E-04	8.37E-04	1.63E-03	8.96E-04	1.24E-04	1.34	1.27E-02	1.54
Numerical	1.88E-01	5.47E-03	3.02E-03	1.69E-04	6.23E-04	1.61E-03	8.61E-04	2.29E-04	1.34	1.20E-02	1.54
% Difference	<1%	4%	4%	61%	26%	<1%	4%	85%	<1%	6%	<1%
Heat input (W)									447		

Case 5 E: Convective heat input with convective cooling and 6 fins

Resistance (W/K)	***Re,ex***	***Re,w***	***Re,wk***	***Re,inter***	***Rv***	***Rc,w***	***Rc,wk***	***Rc,inter***	***Rc,ex,w***	***Rc,ex,f***	***Rhp***	***Rtot***
Empirical/analytical	1.87E-01	5.69E-03	3.14E-03	6.05E-04	1.87E-03	1.63E-03	8.96E-04	1.73E-04	1.36	2.84	1.40E-02	9.34E-01
Numerical	1.85E-01	5.62E-03	3.07E-03	2.60E-04	1.51E-03	1.62E-03	9.09E-04	9.74E-05	1.36	2.84	1.31E-02	9.33E-01
% Difference	1%	1%	2%	57%	19%	<1%	1%	44%	<1%	<1%	7%	<1%
Heat input (W)		616	Total heat output through wall (W)			194	Total heat output through fins (W)					424

Table 7 *HTHP with channel flow cooling thermal resistances for Case 5 F-I*

Case 5 F: Constant heat input without fins

Resistance (W/K)	***Re,w***	***Re,wk***	***Re,inter***	***Rv***	***Rc,w***	***Rc,wk***	***Rc,inter***	***Rc,ex,w***	***Rhp***	***Rtot***
Empirical/analytical	5.69E-03	3.14E-03	5.29E-04	1.03E-03	1.63E-03	8.96E-04	1.51E-04	1.36	1.31E-02	1.38
Numerical	5.67E-03	3.12E-03	3.78E-04	8.91E-04	1.68E-03	9.25E-04	2.70E-04	1.07	1.29E-02	1.08
% Difference	<1%	<1%	29%	14%	3%	3%	78%	22%	1%	23%
Heat input (W)						562				

Case 5 G: Constant heat input with fins

Resistance (W/K)	***Re,w***	***Re,wk***	***Re,inter***	***Rv***	***Rc,w***	***Rc,wk***	***Rc,inter***	***Rc,ex,w***	***Rc,ex,f***	***Rhp***	***Rtot***
Empirical/analytical	5.69E-03	3.14E-03	4.55E-03	1.40E-01	1.63E-03	8.96E-04	1.30E-03	1.36E+00	2.84	1.56E-01	1.07
Numerical	5.67E-03	3.12E-03	2.46E-02	1.35E-01	1.32E-03	8.78E-04	1.49E-01	9.75E-01	2.52	3.15E-01	1.25
% Difference	<1%	<1%	81%	3%	19%	2%	300%<	28%	11%	102%	17%
Heat input (W)		562	Total output form walls(W)			388	Total output from fins (W)				177

Case 5 H: Convective heat input without fins

Resistance (W/K)	***Re,w***	***Re,wk***	***Re,inter***	***Rv***	***Rc,w***	***Rc,wk***	***Rc,inter***	***Rc,ex,w***	***Rhp***	***Rtot***
Empirical/analytical	5.69E-03	3.14E-03	6.03E-04	1.65E-03	1.63E-03	8.96E-04	1.72E-04	1.36	1.38E-02	1.38
Numerical	6.14E-03	3.38E-03	4.78E-04	1.46E-03	1.77E-03	9.76E-04	3.42E-04	1.03	1.45E-02	1.04
% Difference	8%	8%	21%	11%	9%	9%	99%	24%	6%	24%
Heat input (W)						636				

Case 5 I: Convective heat input with fins

Resistance (W/K)	***Re,w***	***Re,wk***	***Re,inter***	***Rv***	***Rc,w***	***Rc,wk***	***Rc,inter***	***Rc,ex,w***	***Rc,ex,f***	***Rhp***	***Rtot***
Empirical/analytical	5.69E-03	3.14E-03	7.49E-04	2.62E-03	1.63E-03	8.96E-04	2.14E-04	1.36	2.84	1.49E-02	9.35E-01
Numerical	5.67E-03	3.12E-03	8.55E-04	2.65E-03	1.39E-03	9.15E-04	8.40E-04	9.74E-01	2.48	1.54E-02	9.89E-01
% Difference	<1%	<1%	12%	1%	14%	2%	75%	29%	13%	3%	5.8%
Heat input (W)		734	Total output from wall (W)			567	Total output from fins (W)				215

Chapter 2. Reduction of Heat Pipe Thermal Resistances Through the use of Nanofluid

Nomenclature

A	area (m^2)	*Greek symbols continued*	
C	speed of sound (m/s)	ϕ	nanoparticle volume concentration
C_f	dimensionless drag coefficient	φ	porosity
c_p	specific heat (W/kg K)	*Subscripts*	
d	diameter (m)	a	adiabatic
E_{latent}	latent (J)	*abs*	absolute
$E_{sensible}$	sensible (J)	*BF*	basefluid
h	heat transfer coefficient (W/m^2 K)	*BP*	bulk nanoparticle
h_{fg}	latent heat (J/kg)	c	condenser
K	permeability	*cap*	capillary
K'	specific heat ratio	*cond*	condensation
k	thermal conductivity (W/m K)	e	evaporator
L	length (m)	*evap*	evaporation
p	pressure (Pa)	eff	effective
M	merit number	*HP*	heat pipe
$\dot{m}$	mass flow rate (kg/s)	i	inner, iteration
$\dot{m}''$	mass flux (kg/ m^2s)	l	liquid
N	mesh number (1/m)	*layer*	nanolayer
Q	heat rate (W)	max	max
(QL)	heat transport factor	*NF*	nanofluid
q	heat flux (W/m^2)	*NP*	effective nanoparticle
R	thermal resistance (W/K)	o	outer
R_g	universal gas constant (J/kg K)	*op*	operating
r	radius (m)	out	outlet
S	crimping factor	p	pore
T	temperature (K)	s	solid
t	thickness (m), time (s)	sat	saturation
V	velocity magnitude (m/s), Volume (m^3)	t	total
v	kinematic viscosity (m^2/s)	v	vapor
v	radial velocity (m/s)	wk	wick
w	axial velocity (m/s)	0	reference value
Greek symbols		*velocity vector*	*r, z*
α	ratio of nanolayer to nanoparticle thermal conductivity		
β	ratio of nanolayer thickness to nanoparticle radius		
δ	film thickness (m)		
μ	dynamic viscosity (N·S/m^2)		
ρ	density (kg/m^3)		
σ	surface tension (N/m)		
ν	kinematic viscosity (m^2/s)		
Φ	viscous dissipation		

1. Introduction

Nanofluids (NFs) are generally suspensions of metal or metal oxide particles/fibers with an average size of about 1-100 nm. Common nanoparticles (NPs) include Al_2O_3, TiO_2, CuO, Au, Ag and Si, which may be added to aqueous or alcohol basefluids, and are synthesized in a number of ways, such as by inert gas condensation (Granqvist & Buhrman, 1976), chemical vapor deposition (Choi et al., 2001), spray-drying (Ashley, 1994), and rapid expansion in supersonic nozzles (Hill et al., 1963). Ultrasonic agitation and additional surfactants are also used to promote better uniformity and to prevent agglomeration of nanoparticles in solution (Lee et al. 1999).

The feasibility and effectiveness of thermal enhancement of fluids with nanoparticles (and the term "nanofluid") was introduced by Choi & Eastman (1995). Prior to the theoretical work of Choi & Eastman (1995), it was largely understood that the effective conductivity of a solution could be enhanced by addition of supplemental high-conductivity particles. In fact, Maxwell (1881) theoretically modeled the effective thermal conductivity of suspensions containing spherical particles. However, most studies focused on the addition of micro-scale particles, which showed limited use in practical engineering applications because of clogging problems (Choi & Tran 1991; Choi et al., 1992a, 1992b).

In stationary fluids, nanofluids have demonstrated relatively high temperature-dependent effective thermal conductivities (Eastman et al., 2001; Choi et al., 2001; You et al., 2003) that exceed those of traditional solid-liquid suspensions. Eastman et al. (2001) observed an increase in effective conductivity of about 40% using 0.3 vol.% metallic copper nanoparticles as compared to the basefluid of ethylene glycol. Choi et al. (2001) similarly saw an increase in effective thermal conductivity for a dispersion of carbon nanotubes in a synthetic poly (α-olefin) oil; however, it was noted that the increase in effective thermal conductivity was non-linear, and was not accurately predicted using previous models, including those of Maxwell (1881) and the Hamilton & Crosser (1959) model.

Nanofluid behavior and enhancement has also been investigated for various convective and phase-change applications. You et al. (2003) experimentally studied the thermal behavior of aqueous Al_2O_3 nanofluids for pool boiling at different nanoparticle concentrations. The experiment indicated a ~200% increase in the critical heat flux compared to that for the pure water case (though the nucleate boiling heat transfer coefficients appeared to be equal for both cases).

Putra et al. (2003) studied natural convective heat transfer of a 4.0% Al_2O_3 nanofluid inside a horizontal cylinder that was heated and cooled at opposite ends. However, it was found that the convective heat transfer coefficient for nanoparticle solutions was less than that for the same system charged with distilled water. Putra et al. (2003) concluded that the heat transfer deterioration ultimately depended on particle density, concentration, as well as the aspect ratio of the outer cylinder.

Xuan & Li (2000) summarized a procedure for preparation of a homogenous nanofluid solution, along with a theoretical model to predict the heat transfer of turbulent nanofluid flow in

a tube. A dispersed model was used to account for the complex one- and multi-dimensional interactions of Brownian diffusion, sedimentation, and dispersion which coexist in nanofluid convective flows.

Heat pipes and gravity-assisted thermosyphons are effective, passive devices that enable high rates of heat transfer using internal phase change mechanisms (Faghri 2012, 2014, 2016; Shabgard et al. 2015). A conventional heat pipe is typically a rigid, sealed container under vacuum, charged with an amount of liquid. A heat source is applied to the evaporator, and heat is transferred to the wick structure by a combination of conduction and convection. The liquid contained in the wick structure vaporizes and passes to the evacuated vapor core of the heat pipe. The vapor then moves through the adiabatic section, which provides near-isothermal internal heat transfer at steady-state conditions. The vapor undergoes condensation in the condenser section, which is cooled by an external heat sink. The liquid condensate is then pumped back to the evaporator section via capillary action, where it again undergoes evaporation. The latent heat transfer from vaporization and condensation in the evaporator and condenser sections, respectively, allow for the high heat transfer rates and minimal thermal resistance of heat pipes. Thermosyphons operate similarly to heat pipes, but do not rely on a wick structure for recirculation of the condensate; instead they rely on gravity assisted-condensate films to continue the internal wetting of the evaporator section.

Prior research of nanofluid integration with heat pipes has mainly been experimental in nature, as detailed in Table 8. The first column indicates the principal investigators, year, and the type of study (experimental/theoretical). The column to the right includes information relating to the working fluid and the average diameter of the nanoparticles. The following column provides the volume, weight, or mass concentration of the nanofluid. The next column includes general trends and supporting observations relating to the change in thermal resistance. Other general comments and relevant information are in the final column.

Table 8 indicates that the addition of nanofluids may enhance flow and thermal performance according to different physical mechanisms associated with the various types of heat pipe (conventional heat pipes, thermosyphons, pulsating, rotating, micro/miniature, and loop heat pipes). Conventional heat pipes rely on a wick structure to provide the capillary pressure to recirculate the working fluid from the condenser section to the evaporator section. Nanoparticle deposition in the wick structure (particularly in the evaporator section) and improved wettability of the wick surface is largely believed to be reasons for nanofluid thermal performance enhancement in a conventional heat pipe (Kang et al., 2006, 2009; Lin et al., 2008; Mousa, 2011; Kole & Dey, 2013; Ghanbarpour & Khodabandeh, 2015; Kim et al., 2015). In addition, there is a deposition layer which alters the effective thermal conductivity of the nanoparticle itself. Thermosyphons (wickless heat pipes) involve film evaporation and pool boiling heat transfer in the evaporator section, and gravity-assisted condensed liquid films provide the recirculation of liquid from the condenser section to the evaporator section. Nanoparticles provide nucleation sites and the bombardment of vapor bubbles, which improves heat transfer rates. Loop and pulsating heat pipes may also experience performance enhancement with nanofluids due to an

increased number of nucleation sites, lower bubble departure frequency, and bombardment of forming vapor bubbles (Riehl & Dos, 2012; Gunnasegaran et al., 2013; Wan et al., 2015).

From Table 1, a number of further observations and conclusions can be drawn pertaining to the use of nanofluids in heat pipes. The addition of nanofluids in heat pipes have predominately shown enhanced thermal behavior. A maximum reduction in heat pipe thermal resistance of 81% was obtained by Kang et al. (2006) using a silver-water nanofluid, as compared to a similarly dimensioned heat pipe filled with water. Similarly, Liu & Zhu (2011) found a reduction in the total heat pipe thermal resistance by 60% using copper oxide-water nanofluid. Other thermal improvement was based on the reduced surface tension made possible by nanofluids (Khandekar et al. 2008; Liu et al., 2011; Venkatachalapathy et al., 2015), which allows for greater wettability and improved nucleate boiling (Mousa, 2011; Wan et al., 2015). In addition to the enhanced effective thermophysical properties of nanofluids, there is an optimal fill ratio of a heat pipe that is dependent on the nanoparticle concentration of the nanofluid. It was observed that nanofluids reduce the optimal fill ratio of a particular heat pipe, and thus require less base fluid to fully saturate the wick (Teng et al., 2010). Xuan & Li (2000) observed an increase in the effective thermal conductivity of almost 1.8% for 7.5 vol.% Cu-water nanofluid over that of a water-filled heat pipe, and identified the influence of volume fraction, shape, dimensions and properties of the nanoparticles. The effective thermal conductivity of an aqueous alumina nanofluid was observed to increase with a greater volume fraction of nanoparticles, yet decreased 25% with increased sphericity of the nanoparticles. Kim & Bang (2016) noted enhanced heat transfer effects in an aqueous graphene-oxide charged heat pipe due to improved wettability and capillary pumping pressure. The deposition of nanoparticles on the evaporator wick-vapor interface resulted in gravity-driven liquid films of condensate, much like in a thermosyphon. In addition, nanoparticle deposition within the wick increased the capillary pressure, which further improved heat transfer of the nanofluid-filled heat pipes compared to those using the basefluid (with no nanoparticles).

It should be noted that addition of nanoparticles to a base fluid can, under some circumstances, decrease heat pipe thermal performance. Kim et al. (2015) observed a conventional heat pipe with a screen wire-mesh subject to a constant heat flux at the evaporator and convective cooling of the condenser. Increased wettability was observed and attributed to a nanoparticle deposition in the evaporator section, which decreased nucleate boiling, bubble departure frequency, and increased the overall thermal resistance. Tsai et al. (2004), Lin et al. (2008), Teng et al. (2010), Liu & Zhu, (2011), Mousa (2011), Kole & Dey (2013), and Wan et al. (2015) indicated that there is an optimal concentration of nanoparticles in a nanofluid-charged heat pipe for a maximum reduction in thermal resistance. Deviation from the optimal concentration resulted in larger thermal resistance and overall decreased heat transfer. In addition, Tsai et al. (2004) observed permanent precipitation of nanoparticles, and Buschmann & Franzke (2014) observed decreased effectiveness of nanofluids after five weeks of inactivity, especially for higher nanoparticle concentrations. It was hypothesized that precipitation of nanoparticles occurred in the evaporator section. Long-term sedimentation and decreased effectiveness is an important consideration for nanofluid application in heat pipes, though Yang

& Liu (2011) partially addressed the sedimentation issue with the addition of surface-functualized silica nanoparticles.

There are far less analytical and numerical investigations regarding nanofluids and their application to heat pipes. Shafahi et al. (2010a) used a two-dimensional steady, compressible analytical approach employing effective fluid properties to obtain the velocity, pressure, temperature and maximum heat transfer limit for a conventional screen-wick cylindrical heat pipe charged with aqueous Al_2O_3, CuO, and TiO_2 nanoparticles. The effect of particle diameter and nanoparticle concentration was observed under the assumption of a constant condenser wall temperature. The overall heat transfer of the heat pipe increased with the concentration of nanoparticles, and the optimum concentration of each nanoparticle in the base fluid was identified.

Do & Jang (2010) studied nanofluid enhancement in a flat micro-heat pipe and formulated two different analytical models under the assumptions of one-dimensional steady incompressible axial flow, a one-dimensional axial temperature difference in the heat pipe wall, and negligible convection in the liquid and vapor phases. The first model investigated the heat transfer and thermal resistance of the heat pipe with respect to an enhanced effective thermal conductivity of the working fluid. The second model simulated heat transfer in the heat pipe due to increased surface area of the highly conductive deposition layer of nanoparticles surrounding the grooved wick structure. It was concluded that the thermal resistance of the nanofluid charged heat pipe is dependent on two opposing phenomena. The thin deposition layer of nanoparticles in the evaporator causes an increased liquid pressure drop within the porous nanoparticle layer, which limits evaporative heat transfer. However, the deposition of nanoparticles also results in additional conductive surface area within the evaporator section wick structure, thus increasing heat transfer.

Ghanbarpour and Khodabandeh (2015) developed a steady-state analytical model alongside their experimental study to predict the effective thermal conductivity, viscosity, entropy generation, and thermal resistance of a nanofluid- and basefluid-charged heat pipe using a thermal network approach. The model assumed negligible axial conduction through the heat pipe wall, wick, and negligible thermal resistance through the vaporcore. The experiment indicated a reduction in entropy generation of between 3-13.5% using nanofluids at concentrations of 1-5.0 vol.%. The proposed analytical model showed reasonable agreement with experimental data. Mashaei & Shahryari (2015) extended the analytical solution of the energy equation from Shabgard & Faghri (2011) using separation of variables to predict the wall temperature of a conventional cylindrical heat pipe charged with water based Al_2O_3 and TiO_2 nanofluids. The analysis assumed steady-state conditions, constant thermal conductivities of the nanoparticles, basefluid, wall, and solid phase of the wick, and a fully saturated wick. It was also assumed that the heat transfer in the porous wick was mainly by conduction. The analytical model predicted that a higher concentration of nanoparticles or nanoparticles of smaller diameter resulted in an increased heat transfer coefficient between the pipe wall and saturated vapor flow, and a decreased temperature difference between the evaporator and condenser sections of the heat pipe for both Al_2O_3 and TiO_2 nanoparticles.

Nanofluids have shown promise for higher heat transfer rates, higher effective thermal conductivity (lower thermal resistance), superior boiling and convective heat transfer, and beneficial influence on bubble formation and departure characteristics. However, some inconsistencies in nanofluid performance enhancement and varying explanations for the mechanisms of heat transfer make nanofluid behavior in heat pipes somewhat controversial. Most past studies are experimental in nature, based on overall performance measurement rather than detailed description of physical phenomena. Furthermore, past analytical and numerical research efforts mainly use conventional simplified assumptions that approximate the effects associated with nanofluids.

As a potential solution to the conflicting data and ambiguities of nanoparticle/nanofluid use, this effort serves to describe nanofluid heat transfer in heat pipes with a comprehensive numerical approach. Aqueous solution of aluminum, copper, and titanium oxide (Al_2O_3, CuO, TiO_2, respectively) were simulated as the working fluids of a conventional cylindrical heat pipe with a screen mesh wick, and the resulting thermal behavior was compared to previous experimental investigations. A parametric study was conducted to observe the effects of nanoparticle concentration, heat load, nanolayer deposition, and nanolayer thermal conductivity. The Merit number of a heat pipe was modified to include nanofluid properties and was used to illustrate the competing relationship between capillary and viscous effects. The maximum heat transport of a heat pipe corresponding to the optimal nanoparticle concentration was predicted numerically based on type of nanoparticle. This effort is unique due to the identification of the optimal nanoparticle concentration, as well as the consideration of the effect of the nanoparticle deposition layer using a numerical approach.

2. Physical Model

A two-dimensional conventional cylindrical heat pipe configuration is presented in Figure 15. The heat pipe includes three separate regions, the evaporator, adiabatic, and condenser sections, which are subject to different boundary conditions. In addition, there are three separately defined structural components of the heat pipe, the wall of outer radius r_o, a wick of outer radius r_i, and the vapor core of radius r_v.

An exterior heat source is applied to the surface of the heat pipe wall at the evaporator section, and the heat acts to vaporize the liquid working fluid in the wick structure at the liquid/vapor interface. The resulting pressure difference in the vapor core drives the axial flow of vapor through the adiabatic section and to the condenser. The condenser section acts as a heat sink, and provides heat rejection for the thermal energy transported via the inner vapor. Simultaneously, the vapor condenses in the condenser section and saturates the wick structure. The liquid condensate is then returned to the evaporator section due to the axial capillary pressure gradient in the wick.

Nanoparticles are assumed to be mainly within the wick structure and also as a thin layer on the wick surface Grab et al. (2014) and Buschmann & Franzke (2014). Grab et al. (2014) analyzed the vapor transport of two gold nanofluids (10^{-4} wt.%, 16 nm and 66 nm, respectively)

using a Liebig condenser, which involves the partial evaporation and condensation of a liquid sample. After evaporation and condensation of each sample, the 16 nm gold nanofluid had a weight percentage of 60.0 $\pm$ 6.0 x 10^{-9}, and the 66 nm particles had a weight percentage of 37.0 $\pm$ 3.7 x 10^{-9}. It was concluded that only extremely small fractions of nanoparticles are transported in the vapor phase. Buschmann & Franzke (2014) studied the vapor transport of nanofluids in a thermosyphon and concluded through observation with a Scanning Electron Microscope that there was no deposition of nanoparticles within the wick of the condenser section. The minor quantities of gold particles found in the condenser were characterized as "gold splatters," which likely reached the condenser during the violent boiling process. Accordingly, the governing equations for vapor flow do not account for nanoparticle transport. However, both the nanofluid and vapor pressure drops are coupled through the heat transfer characteristics of the working fluid.

The vapor flow is modeled as 2-dimensional, steady compressible laminar flow with constant viscosity (Faghri & Zhang, 2006; Faghri et al., 2010):

Continuity:

$$\frac{1}{r}\frac{\partial}{\partial r}\left(\rho_v r \mathsf{v}_v\right)+\frac{\partial}{\partial z}\left(\rho_v w_v\right)=0 \tag{22}$$

Radial momentum:

$$\frac{1}{r}\frac{\partial}{\partial r}\left(\rho_v r \mathsf{v}_v^2\right)+\frac{\partial}{\partial z}\left(\rho_v \mathsf{v}_v w_v\right)=-\frac{\partial p}{\partial r}+\frac{4}{3}\mu_v\frac{1}{r}\frac{\partial}{\partial r}\left(r\frac{\partial \mathsf{v}_v}{\partial r}\right)+\mu_v\frac{\partial^2 \mathsf{v}_v}{\partial z^2}+\mu_v\left(\frac{1}{3}\frac{\partial^2 w_v}{\partial z\partial r}-\frac{4}{3}\frac{\mathsf{v}_v}{r^2}\right) \tag{23}$$

Axial momentum:

$$\frac{1}{r}\frac{\partial}{\partial r}\left(\rho_v r \mathsf{v}_v w_v\right)+\frac{\partial}{\partial z}\left(\rho_v w_v^2\right)=-\frac{\partial p}{\partial z}+\frac{\mu_v}{r}\frac{\partial}{\partial r}\left(r\frac{\partial w_v}{\partial r}\right)+\frac{4}{3}\mu_v\frac{\partial^2 w_v}{\partial z^2}+\frac{1}{3}\mu_v\left(\frac{1}{r}\frac{\partial \mathsf{v}_v}{\partial z}+\frac{\partial^2 \mathsf{v}_v}{\partial z\partial r}\right) \tag{24}$$

Energy:

$$\rho_v c_{p,v}\left(\mathsf{v}_v\frac{\partial T_v}{\partial r}+w_v\frac{\partial T_v}{\partial z}\right)=k_v\left[\frac{1}{r}\frac{\partial}{\partial r}\left(r\frac{\partial T_v}{\partial r}\right)+\frac{\partial^2 T_v}{\partial z^2}\right]+\frac{Dp_v}{Dt}+\mu_v\Phi \tag{25}$$

where the viscous dissipation of the vapor is given by:

$$\Phi=2\left[\left(\frac{\partial \mathsf{v}_v}{\partial r}\right)^2+\left(\frac{\mathsf{v}_v}{r}\right)^2+\left(\frac{\partial w_v}{\partial z}\right)^2\right]+\left(\frac{\partial \mathsf{v}_v}{\partial z}+\frac{\partial w_v}{\partial r}\right)^2-\frac{2}{3}\left[\frac{1}{r}\frac{\partial}{\partial r}\left(r\mathsf{v}_v\right)+\frac{\partial w_v}{\partial z}\right]^2 \tag{26}$$

and the equation of state is used to solve for the compressibility of the vapor:

$$p_v=\rho_v R_g T_v \tag{27}$$

The steady two-dimensional heat conduction in the heat pipe wall is described by the energy equation:

$$\frac{1}{r}\frac{\partial}{\partial r}\left(r\frac{\partial T_v}{\partial r}\right)+\frac{\partial^2 T_v}{\partial z^2}=0 \tag{28}$$

Fluid mechanics and heat transfer within the wick structure involves complex interaction between the solid phase of the wick, the liquid within the pores, and the nanoparticles within the liquid. The nanofluid behavior through the screen mesh wick structure is modeled as steady, two-dimensional flow through porous media. The porous wick structure is a stationary, solid matrix with continuous connection of the internal voids, and with porosity φ. Furthermore, the void space is considered fully saturated with nanofluid. For all screen mesh cases, the void (or pore) characteristic length d_p is far less than the porous zone length scale L ($d_p \ll L$) in the radial and axial directions, and thus the volume averaged properties and local mean velocity are appropriate in the wick computation domain.

The intrinsic velocity of the fluid is the area-averaged velocity divided by the total volume filled with liquid, which is assumed isotropic and homogeneous throughout. The liquid, nanoparticles and wick structure are all assumed to be in local thermal equilibrium. However, the addition of nanoparticles to the working fluid requires modified effective thermophysical properties in the associated governing equations. Specifically, The addition of nanoparticles to the working fluid is described by the effective values of k_{eff}, ρ_{NF}, and ν_{NF} for effective thermal conductivity, density and viscosity of the nanofluid, respectively .

The liquid flow in the wick is modeled as 2-dimensional steady flow in porous media with effective properties (Faghri & Zhang 2006).

Continuity:

$$\frac{1}{r}\frac{\partial}{\partial r}\left(r\mathrm{v}_{NF}\right)+\frac{\partial w_{NF}}{\partial z}=0 \tag{29}$$

Radial momentum:

$$\begin{aligned}\frac{1}{\varphi^2}\left(\mathrm{v}_{NF}\frac{\partial \mathrm{v}_{NF}}{\partial r}+w_{NF}\frac{\partial \mathrm{v}_{NF}}{\partial z}\right)=&-\frac{1}{\rho_{NF}}\frac{\partial p}{\partial r}-\frac{\nu_{NF}\mathrm{v}_{NF}}{K}-\frac{\rho_{NF}C_f}{\sqrt{K}}\left|\mathbf{V}_{NF}\right|\mathrm{v}_{NF}\\&+\frac{\nu_{NF}}{\varphi}\left[\frac{1}{r}\frac{\partial}{\partial r}\left(r\frac{\partial \mathrm{v}_{NF}}{\partial r}\right)-\frac{\mathrm{v}_{NF}}{r^2}+\frac{\partial^2 \mathrm{v}_{NF}}{\partial z^2}\right]\end{aligned} \tag{30}$$

Axial momentum:

$$\frac{1}{\varphi^2}\left(\mathsf{v}_{NF}\frac{\partial w_{NF}}{\partial r}+w_{NF}\frac{\partial w_{NF}}{\partial z}\right)=-\frac{1}{\rho_{NF}}\frac{\partial p}{\partial z}-\frac{\nu_{NF}w_{NF}}{K}-\frac{\rho_{NF}C_f}{\sqrt{K}}|\boldsymbol{V}_{NF}|w_{NF}$$
$$+\frac{\nu_{NF}}{\varphi}\left[\frac{1}{r}\frac{\partial}{\partial r}\left(r\frac{\partial w_{NF}}{\partial r}\right)+\frac{\partial^2 w_{NF}}{\partial z^2}\right] \tag{31}$$

Energy:

$$\left(\rho_{NF}c_{p,NF}\right)\left(\mathsf{v}_{NF}\frac{\partial T_{NF}}{\partial r}+w_{NF}\frac{\partial T_{NF}}{\partial z}\right)=\frac{1}{r}\frac{\partial}{\partial r}\left(rk_{eff}\frac{\partial T_{NF}}{\partial r}\right)+\frac{\partial}{\partial z}\left(k_{eff}\frac{\partial T_{NF}}{\partial z}\right) \tag{32}$$

where φ is the porosity of the wick, K is the wick permeability, and $|\boldsymbol{V}_{NF}|$ is the magnitude of the liquid velocity. C_f is a dimensionless drag constant, which is assumed to be a constant 0.55 (Faghri & Zhang, 2006).

The effective thermal conductivity, k_{eff}, includes the combined effect of the porous screen-mesh wick structure, the nanofluid, and nanolayer deposition on the surface of the nanoparticle. It is important to differentiate between the nanoparticle deposition on the evaporator section of the wick and the formation of a nanolayer on the nanoparticle surface. This study includes the effects of the nanolayer on the particles. The effective thermal conductivity of the saturated wick is calculated:

$$k_{eff}=\frac{k_{NF}\left[k_{NF}+k_s-(1-\varphi)(k_{NF}-k_{s)}\right]}{(k_{NF}+k_s)+(1-\varphi)(k_{NF}-k_{s)}} \tag{33}$$

where the subscripts NF and S are the nanofluid and solid phases of the wick structure, respectively, and the porosity φ, is obtained:

$$\varphi=1-\frac{\pi SNd}{4} \tag{34}$$

where S is the crimping factor, N is the mesh number, and d is the wire diameter. An empirically derived constant of 1.05 was used for the crimping factor. The permeability, K, of the screen mesh is calculated from:

$$K=\frac{d^2\varphi^3}{122(1-\varphi)^2} \tag{35}$$

Yu & Choi (2003) proposed that the thermal conductivity of the nanoparticle is itself defined by an effective thermal conductivity, and is not accurately represented by the bulk thermal conductivity of the same material. An effective thermal conductivity for nanofluids, k_{NF}, and the nanoparticles themselves, k_{NP}, which includes the effect of the deposited nanolayer formed

on the nanoparticls, were developed based on a modified Maxwell model (Schwartz et al., 1995; Yu & Choi, 2003). The thermal conductivities are, respectively:

$$k_{NF} = k_{BF}\left[\frac{k_{NP} + 2k_{BF} + 2\left(k_{NP} - k_{BF}\right)\left(1+\beta\right)^3\phi}{k_{NP} + 2k_{BF} - \left(k_{NP} - k_{BF}\right)\left(1+\beta\right)^3\phi}\right] \tag{36}$$

$$k_{NP} = k_{BP}\frac{\left[2\left(1-\alpha\right)+\left(1+\beta\right)^3\left(1+2\alpha\right)\right]\alpha}{-\left(1-\alpha\right)+\left(1+\beta\right)^3\left(1+2\alpha\right)} \tag{37}$$

where the subscripts NP and BP are the effective nanoparticle and bulk material of the nanoparticle, respectively, α is the ratio of the thermal conductivity of the deposition layer to the bulk (no deposition layer) thermal conductivity of the nanoparticle material, and β is the ratio of the nanolayer thickness, t_{layer}, to the original particle radius, r_{NP} (Yu & Choi 2003):

$$\alpha = \frac{k_{layer}}{k_{NP}} \tag{38}$$

and:

$$\beta = \frac{t_{layer}}{r_{NP}} \tag{39}$$

For the case of $k_{layer} = k_{NP}$, the effective thermal conductivity of the nanoparticle, k_{NP} is the same as that of the bulk thermal conductivity of the nanoparticle material; i.e. the length scale of the particle does not alter the thermal conductivity of the material. In this investigation, the thermal conductivity of the nanoparticle deposition layer is assumed to be the same as that of the nanoparticle, resulting in an α of 1.0 (Yu & Choi 2003). Furthermore, the nanolayer thickness may be assumed to be 19-22.0% of the average nanoparticle diameter (Tillman & Hill, 2007). The volume fraction ϕ of the particles is then defined as:

$$\phi = \frac{V_{NP}}{V_{BF} + V_{NP}} \tag{40}$$

The density of the nanofluid, ρ_{NF}, is accounted for by the correlation (Pak & Cho, 1998):

$$\rho_{NF} = \left(1-\phi\right)\rho_{BF} + \phi\rho_{NP} \tag{41}$$

Brinkman's equation (Brinkman, 1952) is used for an approximation of the dynamic viscosity of a nanofluid:

$$\mu_{NF} = \frac{\mu_{BF}}{\left(1-\phi\right)^{2.5}} \tag{42}$$

which is used as the kinematic viscosity, $\nu_{NF} = \mu_{NF}/\rho_{NF}$. The specific heat capacity of the nanofluid may be obtained from the correlation (Pak & Cho, 1998):

$$c_{p,NF} = \frac{(1-\phi)(\rho_{BF} c_{p,\mathrm{BF}}) + \phi(\rho_{NP} c_{p,NP})}{(1-\phi)\rho_{BF} + \phi\rho_{NP}} \tag{43}$$

The surface tension was assumed to decrease linearly with the nanoparticle concentration and was approximated as (Venkatachalapathy et al., 2015):

$$\sigma_{NF} = (1-\phi)\sigma_{BF} \tag{44}$$

Many experimental studies have shown that the surface tension decreases with nanoparticle concentration; in this work it was assumed that a linear approximation would be adequate to determine the approximate trends incurred by adding nanoparticle solids to a working fluid.

The boundary conditions describing the entire computational domain are included below. The vapor velocity is assumed to be zero in the axial and radial directions at the endcaps of the heat pipe due to the assumption of the no-slip condition, and the endcaps are also considered to be adiabatic. The corresponding boundary conditions for the endcaps are then:

$$\mathrm{v}_v = w_v = \frac{\partial T_v}{\partial z} = 0 \tag{45}$$

The two-dimensional computational domain is solved as an axisymmetric problem with symmetry about the longitudinal centerline ($r = 0$). The radial velocity, acceleration and the radial gradient of the temperature are correspondingly zero at $r = 0$.

$$\mathrm{v}_v = \frac{\partial w_v}{\partial r} = \frac{\partial T_v}{\partial r} = 0 \tag{46}$$

The temperature at the liquid-vapor interface is assumed to be the local saturation temperature, given by the Clausius-Clapeyron equation (Faghri 2016):

$$T_{sat} = \left[\frac{1}{T_0} - \frac{R_g}{h_{fg}} \ln\left(\frac{p_{sat}}{p_0} \right) \right]^{-1} \tag{47}$$

where T_0 and p_0 and are the reference temperature and pressure, respectively.

The boundary conditions external to the heat pipe depend on the mode of heat transfer to the evaporator section/from the condenser section. In this investigation, a constant heat flux is applied to the evaporator surface (q_e) and a corresponding constant heat flux exits the condenser section (q_c), to account for the heat input/output at steady state conditions ($q_e = q_c$). If the condenser section and evaporator section are of differing lengths, the heat rate not heat flux must match.

In addition, the radial vapor velocity at the liquid/vapor interface can be written for the evaporator and condenser, respectively. The interfacial velocity accounts for the vaporization of the working fluid in the evaporator and condensation of the fluid in the condenser and is written:

$$v_{\delta,v} = \frac{\dot{m}''_{\delta}}{\rho_{v,\delta}} \tag{48}$$

where, for blowing effects in the evaporator, $v_{\delta,v} > 0$, and for suction in the condenser, $v_{\delta,v} < 0$. The interfacial mass flux $\dot{m}''_{\delta}$, due to phase change can be obtained by the ratio of the heat rate in the evaporator/condenser to the latent heat of vaporization:

$$\dot{m}''_{\delta,e} = \frac{q_{\delta,e}}{h_{fg}} \tag{49}$$

and:

$$\dot{m}''_{\delta,c} = \frac{q_{\delta,c}}{h_{fg}} \tag{50}$$

A pressure boundary condition must be provided to obtain the unique pressure distribution in the heat pipe. This is accomplished through describing the vapor at the end cap of the condenser as a pressure outlet:

$$p_{gage} = p_{abs} - p_{op} \tag{51}$$

Since the heat pipe is simulated as an open system, mass is allowed to enter and exit, this mass flow rate is used to correct the operating temperature and pressure.

3. Modified Merit Number

The Merit number is used as an overall performance indicator of the effectiveness of heat transfer in different sized heat pipes and for those with various working fluids (Reay et al., 2014):

$$M = \frac{\rho \sigma h_{fg}}{\mu} \tag{52}$$

In order to quantify the benefits of a nanofluid-charged heat pipe, as well as to provide a single parameter for comparison with conventional basefluid-charged heat pipes, the original Merit number is written in terms of the effective nanofluid properties:

$$M_{NF} = \frac{\rho_{NF} \sigma_{NF} h_{fg}}{\mu_{NF}} \tag{53}$$

where ρ_{NF}, σ_{NF}, and μ_{NF} are the effective properties of density, surface tension, and viscosity respectively for the nanofluid, and h_{fg} is the latent heat of vaporization of the basefluid. Assuming laminar incompressible vapor flow and negligible gravity effects, and a wet point located at the condenser end of the heat pipe, the maximum heat transfer is calculated (Faghri 2016):

$$\frac{2\sigma_{NF}}{r_{eff}} \geq \left(\frac{\mu_{NF}}{\rho_{NF} A_{wk} K h_{fg}} + \frac{\left(f \,\mathrm{Re}_{z,v} \right) \mu_v}{2 R_v^2 A_v \rho_v h_{fg}} \right) \left(QL \right)_{cap,\max} \tag{54}$$

where r_{eff} is the effective pore radius ($r_{eff} = 1/2N$), N is the mesh number, $f \,\mathrm{Re}_{z,v} = 16$ for laminar flow in a circular pipe, and the maximum heat transport factor $\left(QL \right)_{cap,\max}$ is:

$$\left(QL \right)_{cap,\max} = Q_{max} (0.5 L_e + 0.5 L_c + L_a) \tag{55}$$

The capillary limit is directly related to the surface tension of the nanofluid and the viscous forces within the wick structure. Therefore, the maximum heat load may be numerically predicted for a heat pipe of specific properties, dimensions and working fluid. The sonic limit, another major operating constraint for a heat pipe was not incurred in this study and determined with the following equation for each case (Faghri 2016):

$$Q_{Sonic} = \frac{\rho_{v,e} \mathrm{C}_e h_{hfg} A_v}{\sqrt{2(K'+1)}} \tag{56}$$

where ρ_e, C_e c_0, A_v and K' are the evaporator density, speed of sound at the evaporator temperature and cross sectional area of the vapor core and specific heat ratio.

4. Computational Methodology

The finite volume (control volume) approach (Patankar, 1980) was employed to discretize the differential governing equations. An initial operating temperature and corresponding saturation pressure are estimated and corrected in subsequent iterations. To obtain a unique steady state solution, a vapor pressure boundary condition must be applied at the end cap closest to the condenser for all cooling conditions other than constant condenser heat flux and constant surface temperature. At the endcap, the gage pressure is set to zero and the back flow temperature is set to the operating temperature. In order to remain consistent with the prescribed boundary conditions of adiabatic, and no slip at the endcap, an iterative method is taken and outlined below to decrease and ultimately stop the outflow at the boundary. In order reduce the outflow at the endcap, the mass flux exiting at the condenser endcap was monitored and used as a means to correct the operating temperature. The following solution procedure must be used to correct the operating temperature prediction.

5. Provide sufficient iterations for the endcap mass flow rate to converge.
6. Use the mass flow rate to calculate the change in the operating temperature ΔT_i
7. Re-initialize the domain to the corrected temperature and pressure.

To calculate ΔT_i, the following relation is used:

$$\Delta T_i = \frac{\dot{m}_{out} h_{fg}}{A_v h} \tag{57}$$

where $\dot{m}_{out}$ is the mass flow rate at the condenser endcap, h_{fg} is the heat of vaporization of the working fluid, A_v is the cross sectional area of the heat pipe outlet and h is the heat transfer coefficient external to the condenser section. The solution was deemed mesh independent when the vapor temperature profile varied less than 5.0 % as to when the mesh size is doubled. The numerical solution was solved in the commercial computational fluid dynamics (CFD) package, ANSYS Fluent. Simulations were performed on a Dell Optiplex 7020 (running Microsoft Windows 7 equipped with an Intel i7 – 4790 processor and 16 GB of RAM). Typical computational time for a single simulation was about 1 hour.

5. Results

The performance of the computational approach is compared with two experimental investigations Kumaresan et al. (2014) and Putra et al. (2012). The heat pipe and working fluid properties are presented in Table 9 along with the operating conditions for each study. Following the comparison of the current numerical model, the performances of various nanofluids are evaluated with respect to nanoparticle concentration and overall thermal conductivity of the nanofluid-charged heat pipes.

5.1 Case A

Experimental results by Kumaresan et al. (2014) were used to validate the numerical model. The heat pipe was charged with aqueous CuO nanofluid with nanoparticle concentrations of 1.0 and 1.5 wt.%, and the heat pipe was subject to a constant heat input at the evaporator and a constant heat output boundary condition at the condenser. A similarly sized heat pipe was modeled with a computational mesh of 16, 5, and 6 cells in the radial direction for the vapor, wick and wall, with 200, 160, and 300 cells in the axial directions for the evaporator, adiabatic, and condenser sections. Figure 16 shows the wall temperatures as obtained from the current numerical model, in comparison with those of the experimental data from Kumaresan et al. (2014). The axial wall temperatures for each nanoparticle weight concentration (including 0%, basefluid) are considered to be in excellent agreement with the previous experimental data. Despite small percentage deviation between the numerical and experimental wall temperatures (less than 1%), it can be seen that the numerically obtained temperature drop was higher for both nanofluid-

charged heat pipes compared to that of experimental data. For the 1.00 wt.% nanofluid, the numerical model slightly over-predicted the wall temperature of the evaporator wall, and under-predicted the condenser wall temperature. However, any deviation in wall temperature was at most 0.70% in the evaporator section, and 0.61% in the condenser section.

It was also noted that the deviation between the numerical results and the experimental results are relatively constant for both nanoparticle concentrations. This indicates that the observed over-prediction of the end-to-end temperature drop is constant, and therefore has a similar accuracy for both small and large nanoparticle concentrations.

The slightly larger temperature drop obtained by the numerical model is attributed to an overestimation of the effect of the deposition layer of the nanoparticles. It can be seen that the evaporator temperature is slightly elevated in the numerical prediction compared to the experimental data; this implies that a smaller thermal conductivity exists in the evaporator wick region than the effective thermal conductivity used in the simulation. The thermal conductivity of the nanolayer and the thickness of the layer (eqn. (38) and eqn. (39), respectively) are not reported by Kumaresan et al. (2014) but were specified values based on the specific nanoparticle. The condenser temperature shows less deviation from experimental temperatures, which is expected, because the nanoparticles are not transported by the vapor.

5.2 Case B

The experimental results of Putra et al. (2012) Das et al. and Das et al. (2003) were also compared to the numerical model for simulation of aqueous Al_2O_3 nanofluid (Figure 17, Figure 18). The numerical mesh for a similarly dimensioned heat pipe consisted of 60 axial cells in the condenser and evaporator sections, 80 axial cells in the adiabatic section, and 10, 5 and 6 radial cells in the vapor, wick and wall, respectively. It was found numerically that a 17% reduction in thermal resistance could be achieved from the addition of 2.0 vol.% Al_2O_3 nanoparticles.

Increasing the nanoparticle concentration resulted in a proportional increase in the effective thermal conductivity enhancement, presented as the ratio of the thermal conductivity of the nanofluid to that of the basefluid in **Figure 17**. It was confirmed that the ratio of thermal conductivity enhancement, as predicted by the current numerical model, matched the experimental results of Putra et al. (2012) and Das et al. (2003) within 2%. The experimental data shows relative agreement with this linear trend, and shows a slightly higher thermal conductivity than the numerical data. This is also attributed as a consequence of nanolayer deposition in the wick.

The wall temperature distribution showed a maximum temperature difference of 2.0%, in the adiabatic region between simulations and experimental data (basefluid and nanofluids). It should be noted, that the numerical results predict the wall temperature distribution of the Al_2O_3 nanofluid (Figure 18) with greater accuracy than for Case A, where CuO nanofluid was used in comparison to the experimental results of Kumaresan et al. (2014). This could indicate a smaller nanolayer deposition on the wick evaporator surface when using Al_2O_3 nanoparticles.

5.3 Parametric Study

A parametric study is presented with the intention of isolating the parameters that result in the improved heat transfer performance associated with nanofluids. Most significantly, the effect of nanoparticle volume concentration is examined, and the optimal concentration of nanoparticles is identified. In addition, the effect of several other factors is included, such as the heat input, nanolayer thickness, as well as the ratio of the nanolayer to nanoparticle thermal conductivity. These effects are largely ignored by other analytical and numerical investigations, and are often addressed only qualitatively by experimental means. The three nanofluids considered for each case of the parametric study are aqueous Al_2O_3, CuO, and TiO_2. The input parameters and properties for each parametric case are presented in Table 3 and Table 4. Table 3 indicates the heat pipe dimensions, container, and vapor properties. Table 4 presents the liquid and effective properties used in each case of the parametric study. Unless otherwise noted, the heat rate Q at the evaporator of the heat pipe was 100 W, the ratio of thermal conductivity of the nanolayer to nanoparticle α was unity, and the ratio of the nanolayer thickness to nanoparticle radius β was 20%.

The first parameter considered was the change in working fluid properties and thermal performance due to changes in each nanoparticle concentration. Figure 19 shows the effective properties of the nanofluid charged heat pipe a) the ratio of the nanofluid conductivity to that of the basefluid, b) the effective viscosity of the fluid and c) Merrit number. It can be seen that the enhancement in thermal conductivity and increase in effective viscosity are non-linear. This is in direct agreement with the findings of Choi et al. (2001) but is contrary to the linear trends of thermal conductivity obtained by Eastman et al. (2001), Nsofor & Gadge (2011), and (Oztas & Menlik, 2014). However, the past experimental studies determined a linear dependence of thermal conductivity on volume concentration can be attributed to the limited range of nanoparticle volume concentrations examined by Eastman et al. (2001), Nsofor & Gadge (2011) and Oztas & Menlik (2014), 0-6.0%, 0-5.50%, and 0-5.0%, respectively. For larger volume concentrations of nanoparticles, the thermal conductivity ratio and properties of the nanofluids are non-linear with increased nanoparticle concentration. Increased volume concentration proved to be the most effective in decreasing the total thermal resistance compared to any other parameter, for all nanoparticles. Using the Merit number as a concise descriptor of the heat pipe performance, a similar trend is obtained, where the Merit number has a maximum at the same concentrations for Al_2O_3 and TiO_2 (Figure 19c). Instead, additional limits are anticipated to exist due to the plugging of capillary pores in the wick, as well as due to the inability to keep nanoparticles suspended in the working fluid which are not included in Figure 19c and eqn (53).

In the present study, the end-to-end wall temperature drop of the heat pipe continues to decrease when the particle concentration becomes infeasibly high, i.e. no physical limit was found for the enhancement using nanofluid (Figure 20a). Instead, Figure 20a implies that the end-to-end wall temperature drop will continue to decrease until the thermal conductivity of the nanofluid has reached that of the nanoparticle. A similar trend can be seen in the overall heat pipe thermal resistance (Figure 20b), where the thermal resistance steadily decreases with nanoparticle concentration. However, a limit to the heat transfer of a heat pipe will exist when

the capillary force is overcome by the viscous forces within the wick. Accordingly, the maximum heat transfer based on the capillary limit was numerically obtained for each nanoparticle and relates the nanoparticle concentration to the surface tension of the nanofluid (Figure 20c). The surface tension of an aqueous nanofluid decreases with higher nanoparticle concentration (Khandekar et al. 2008; Liu et al., 2011; Venkatachalapathy et al., 2015) and was approximated as linear. A maximum heat transfer rate is obtained at 25 vol.% for the Al_2O_3 and TiO_2 nanofluids, and 35 vol.% for CuO. The corresponding capillary limits are reached at maximum heat inputs of 790 W, 825 W and 1100 W, for the Al_2O_3, TiO_2, and CuO, respectively. It can be seen that any deviation from this concentration results in a lower capillary limit and thus reduces the maximum heat transfer rate for the heat pipe. This trend is explained by the inverse relationship between surface tension and the density of the nanofluid, shown in eqn. (53). For higher density nanofluids, the viscous force increases, and surface tension decreases. With an increase in Al_2O_3 volume concentration from 0 to 40%, the total thermal resistance of the heat pipe decreased significantly, by approximately 83%. Likewise, the decrease in the total thermal resistance of a CuO and TiO_2 charged heat pipe was approximately 79%, and 76%, respectively. The effective viscosity was determined based solely on nanoparticle concentration and base fluid viscosity as the effect of unique nanoparticles was considered insignificant (Brinkman, 1952).

A separate parametric study was performed to investigate the effect of increased heat input (50-200 W) on an aqueous nanofluid charged-heat pipe with emphasis on the resulting thermal resistance and heat pipe end-to-end wall temperature drop. In contrast, the volume concentration of each nanoparticle is fixed at 5% vol. It can be seen that the temperature drop of the heat pipe increased linearly with increased heat flux at the evaporator wall (Figure 21a), though the thermal resistance was relatively constant for each nanofluid (Figure 21b). In general, it is expected that the total thermal resistance should decrease slightly with increased heat input (Kang et al., 2006; Mousa, 2011). However, since the concentration of nanoparticles is not varied in this case, the thermophysical properties of the heat pipe remain constant; the effective thermal conductivity is fixed, and the thermal resistance is relatively constant. It should be noted, that the tested heat inputs are far less than the predicted maximum heat input for each nanoparticle volume concentration, and thus the capillary limit and sonic limit were not a concern.

The property variations induced by the nanolayer deposition on the particle surface are difficult to measure and are generally assumed to be a fixed value in other studies. In this study the effects of varying nanolayer thicknesses were examined. The nanolayer thickness to nanoparticle radius ratio, β, is 19-22% of the nanoparticle diameter according to the findings of Tillman & Hill (2007)) but an expanded range of 10-25% is studied here for greater insight (Figure 22). Also, a constant nanolayer to nanoparticle thermal conductivity ratio, α, of 1.0 was assumed for the case. The thickness of the nanoparticle deposition layer influences the temperature drop and overall thermal resistance of the heat pipe to a different extent depending on the type of nanoparticle used. The thickness of the nanoparticle layer has a relatively large effect on the working fluid properties and thermal behavior. Most notably, the thermal resistance of the heat pipe decreases by approximately 5.9%, 6.7%, and 7.0% for TiO_2, CuO, and Al_2O_3, respectively, for nanolayer thicknesses ranging between 10 and 25% of the nanoparticle diameter

(20 nm). The maximum nanolayer thickness (a β value of 25%) caused a more significant reduction in thermal resistance than that induced by the maximum heat input examined (200 W).

The last nanofluid case was the effect of the ratio of thermal conductivities of the deposition nanolayer to that of the nanoparticles themselves, α. This ratio is neglected in most existing works because of the difficulty in measurement, and is normally assumed to be 1.0 to indicate a nanolayer with the same thermal conductivity as the nanoparticles (Yu & Choi, 2003). For the purposes of the parametric study, values of α from 0.25 to 1.5 were used as the ratio of nanolayer to nanoparticle thermal conductivity. It can be seen that there is a limit to the increase in thermal conductivity of a nanofluid (Figure 23a), which is approached as α reaches 1.5%. Similarly, the reduced end-to-end temperature drop (Figure 23b) reaches a corresponding limit. It can be further noted that the effect of an increased nanolayer thermal conductivity on the overall axial wall temperature drop is similar in magnitude to that caused by increased nanolayer thickness (Figure 23b). The approach of the nanofluid thermal conductivity to a maximum value can be attributed to the quadratic influence of the ratio of the nanolayer and nanoparticle thermal conductivity on the overall thermal conductivity of the working fluid as shown in eqn. (36).

Conclusions

A 2-D laminar, steady, compressible heat pipe numerical model was presented to simulate the operation of a conventional cylindrical heat pipe charged with nanofluid. It was shown that an increase in nanoparticle concentration of the nanofluid lowered the total thermal resistance of the heat pipe up to an optimal volume concentration corresponding to the capillary limit, and was 25% vol. for both Al_2O_3 and TiO_2, and 35% for CuO.

A parametric study was conducted to explore the effects of nanofluid property variations with consideration to nanoparticle concentration, heat input, nanoparticle layer thickness and conductivity. The nanoparticle concentration was found to have the greatest effect on the fluid thermal conductivity and thermal resistance while the heat input was found to have the lowest. In addition, the ratio of the nanolayer thickness to nanoparticle radius, and the ratio of nanolayer to nanoparticle thermal conductivity were found to have pronounced effect on the overall thermal resistance. It is important to include the effects of nanoparticle deposition and the formation of a nanolayer for accurate modeling. A limiting thermal conductivity ratio of the nanolayer to the nanoparticle was identified, at which nanoparticle enhancement no longer made a significant difference on the overall temperature drop and thermal resistance of the heat pipe. In addition, a large increase in nanoparticle concentration is believed to reduce the convection in the wick, effectively lowering the maximum heat transfer rate that of the heat pipe. In this case, the effects of increased thermal conductivity would be offset by decreased convection in the wick. Additional efforts are required for determination of more accurate effective nanofluid properties such as: density, viscosity, and surface tension.

Acknowledgement

This material is based upon work supported by the National Science Foundation under Grant Nos. 1435233 (University of Connecticut) and 1435131 (University of Kansas).

References

Ashley, S., 1994. Small-scale Structure Yields Big Property Payoffs. *Mechanical Engineering*, 116(2), pp.52–57.

Brinkman, H.C., 1952. The Viscosity of Concentrated Suspensions and Solution. *Journal of Chemical Physics*, 20(4), p.571.

Buschmann, M.H. & Franzke, U., 2014. Improvement of Thermosyphon Performance by Employing Nanofluid. *International Journal of Refrigeration*, 40, pp.416–428. http://linkinghub.elsevier.com/retrieve/pii/S0140700713003630.

Choi, S.U.S., Cho, Y.I. & Kasza, K.E., 1992. Degradation Effects of Dilute Polymer Solutions on Turbulent Friction and Heat Transfer Behavior. *Journal of Non-Newtonian Fluid Mechanics*, 41(3), pp.289–307.

Choi, S.U.S. & Eastman, J.A., 1995. Enhancing Thermal Conductivity of Fluids With Nanoparticles. *The Proceedings of the 1995 ASME International Mechanical Engi- neering Congress and Exposition, SanFrancisco, USA, ASME, FED231/MD66*, pp.99–105.

Choi, S.U.S., France, D.M. & Knodel, B.D., 1992. Impact of Advanced Fluids on Costs of District Cooling Systems. In *83rd Annual Conference of the International District Heating and Cooling Association*. Boston, MA.

Choi, S.U.S. & Tran, T.N., 1991. Experimental Studies of the Effects of Non-Newtonian Surfactant Solutions on the Performance of a Shell-and-Tube Heat Exchanger. *Recent Developments in Non-Newtonian Flows and Industrial Applications*, pp.47–52.

Choi, S.U.S., Zhang, Z.G., Yu, W., Lockwood, F.E. & Grulke, E. a., 2001. Anomalous Thermal Conductivity Enhancement in Nanotube Suspensions. *Applied Physics Letters*, 79(14), pp.2252–2254.

Das, S.K., Putra, N., Thiesen, P. & Roetzel, W., 2003. Temperature Dependence of Thermal Conductivity Enhancement for Nanofluids. , 125, pp.567–574.

Do, K.H. & Jang, S.P., 2010. Effect of Nanofluids on the Thermal Performance of a Flat Micro Heat Pipe with a Rectangular Grooved Wick. *International Journal of Heat and Mass Transfer*, 53(9-10), pp.2183–2192. http://dx.doi.org/10.1016/j.ijheatmasstransfer.2009.12.020.

Eastman, J.A., Choi, S.U.., Li, S., Yu, W. & Thompson, L.J., 2001. Anomalously Increased Effective Thermal Conductivities of Ethylene Glycol-Based Nanofluids Containing Copper Nanoparticles. *Applied Physics Letters*, 78(6), pp.718–720.

Faghri, 2016. *Heat Pipe Science and Technology* 2nd ed., Colombia, MO: Global Digital Press.

Faghri, A., 2014. Heat Pipes: Review, Opportunities, and Challenges. *Frontiers in Heat Pipes (FHP)*, 5(1), pp.1–48.

Faghri, A., 2012. Review and Advances in Heat Pipe Science and Technology. *Journal of Heat Transfer*, 134(12), p.123001.

Faghri, A. & Zhang, Y., 2006. *Transport Phenomena in Multiphase Systems* 1st ed., United

States of America: Elsevier.

Faghri, A., Zhang, Y. & Howell, J., 2010. *Advanced Heat and Mass Transfer* 1st ed., Columbia, MO: Global Digitial Press.

Ghanbarpour, M. & Khodabandeh, R., 2015. Entropy Generation Analysis of Cylindrical Heat Pipe Using Nanofluid. *Thermochimica Acta*, 610, pp.37–46. http://www.sciencedirect.com/science/article/pii/S0040603115001720.

Ghanbarpour, M., Nikkam, N., Khodabandeh, R. & Toprak, M.S., 2015. Thermal Performance of Inclined Screen Mesh Heat Pipes Using Silver Nanofluids. *International Communications in Heat and Mass Transfer*, 67, pp.14–20. http://linkinghub.elsevier.com/retrieve/pii/S0735193315001232.

Grab, T., Gross, U., Franzke, U. & Buschmann, M.H., 2014. Operation Performance of Thermosyphons Employing Titania and Gold Nanofluids. *International Journal of Thermal Sciences*, 86, pp.352–364. http://dx.doi.org/10.1016/j.ijthermalsci.2014.06.019.

Granqvist, C.G. & Buhrman, R.A., 1976. Ultrafine Metal Particles. *Journal of Applied Physics*, 47(5), pp.2200–2219.

Gunnasegaran, P., Abdullah, M.Z. & Shuaib, N.H., 2013. Influence of Nanofluid on Heat Transfer in a Loop Heat Pipe. *International Communications in Heat and Mass Transfer*, 47, pp.82–91.

Hamilton, R.L. & Crosser, O.K., 1959. Two-Com Ponent Systems. *I & EC Fundumentals*, 1(3), pp.187–191.

Hill, P.G., Witting, H. & Demetri, E.P., 1963. Condensation of Metal Vapors During Rapid Expansion. *Journal of Heat Transfer1*, 85(4), pp.303–314.

Huminic, G. & Huminic, A., 2013. Numerical Study on Heat Transfer Characteristics of Thermosyphon Heat Pipes Using Nanofluids. *Energy Conversion and Management*, 76, pp.393–399. http://dx.doi.org/10.1016/j.enconman.2013.07.026.

Kang, S.W., Wei, W.-C., Tsai, S.-H. & Huang, C.-C., 2009. Experimental Investigation of Nanofluids on Sintered Heat Pipe Thermal Performance. *Applied Thermal Engineering*, 29(5-6), pp.973–979. http://linkinghub.elsevier.com/retrieve/pii/S1359431108002263.

Kang, S.W., Wei, W.C., Tsai, S.H. & Yang, S.Y., 2006. Experimental Investigation of Silver Nano-fluid on Heat Pipe. *Applied Thermal Engineering*, 26(17-18), pp.2377–2382.

Khandekar, S., Joshi, Y.M. & Mehta, B., 2008. Thermal Performance of Closed Two-phase Thermosyphon Using Nanofluids. *International Journal of Thermal Sciences*, 47(6), pp.659–667.

Kim, K.M. & Bang, I.C., 2016. Effects of Graphene Oxide Nanofluids on Heat Pipe Performance and Capillary Limits. *International Journal of Thermal Sciences*, 100, pp.346–356. http://linkinghub.elsevier.com/retrieve/pii/S1290072915003166.

Kim, K.M., Jeong, Y.S., Kim, I.G. & Bang, I.C., 2015. Comparison of Thermal Performances of Water-Filled, SiC Nanofluid-Filled and SiC Nanoparticles-Coated Heat Pipes. *International Journal of Heat and Mass Transfer*, 88, pp.862–871.

http://linkinghub.elsevier.com/retrieve/pii/S0017931015004792.

Kole, M. & Dey, T.K., 2013. Thermal Performance of Screen Mesh Wick Heat Pipes Using Water-based Copper Nanofluids. *Applied Thermal Engineering*, 50(1), pp.763–770. http://linkinghub.elsevier.com/retrieve/pii/S135943111200470X.

Kumaresan, G., Venkatchalapathy, S., Asirvatham, L.G. & Wongwise, S., 2014. Comparative Study on Heat Transfer Characteristics of Sintered and Mesh Wick Heat Pipes Using CuO Nanofluids. *International Communications in Heat and Mass Transfer*, 57, pp.208–215.

Lee, S., Choi, S.U.S., Li, S. & Eastman, J.A., 1999. Measuring Thermal Conductivity of Fluids Containing Oxide Nanoparticles. *Journal of Heat Transfer*, 121(2), pp.280–289.

Lin, Y.H., Kang, S.W. & Chen, H.L., 2008. Effect of Silver Nano-fluid on Pulsating Heat Pipe Thermal Performance. *Applied Thermal Engineering*, 28(11-12), pp.1312–1317. http://www.sciencedirect.com/science/article/pii/S1359431107003468.

Liu, Z. & Zhu, Q., 2011. Application of Aqueous Nanofluids in a Horizontal Mesh Heat Pipe. *Energy Conversion and Management*, 52(1), pp.292–300. http://dx.doi.org/10.1016/j.enconman.2010.07.001.

Liu, Z.-H., Li, Y.-Y. & Bao, R., 2011. Compositive Effect of Nanoparticle Parameter on Thermal Performance of Cylindrical Micro-grooved Heat Pipe Using Nanofluids. *International Journal of Thermal Sciences*, 50(4), pp.558–568. http://linkinghub.elsevier.com/retrieve/pii/S129007291000325X\nhttp://www.sciencedirect.com/science/article/pii/S129007291000325X.

Mashaei, P.R. & Shahryari, M., 2015. Effect of Nanofluid on Thermal Performance of Heat Pipe with Two Evaporators; Application to Satellite Equipment Cooling. *Acta Astronautica*, 111, pp.345–355. http://www.sciencedirect.com/science/article/pii/S0094576515000430.

Maxwell, J.C., 1881. *A Treatise on Electricity and Magnetism* 2nd ed., Clarendon Press.

Mehta, B. & Khandekar, S., 2007. Two-Phase Closed Thermosyphon with Nanofluids. In *14th International Heat Pipe Conference*. Florianopolis, Brazil. http://home.iitk.ac.in/~samkhan/Bio_data/publications/Khandekar_Conf_14.pdf.

Mousa, M.G., 2011. Effect of Nanofluid Concentration on the Performance of Circular Heat Pipe. *Ain Shams Engineering Journal*, 2(1), pp.63–69. http://linkinghub.elsevier.com/retrieve/pii/S2090447911000049.

Naphon, P., Assadamongkol, P. & Borirak, T., 2008. Experimental Investigation of Titanium Nanofluids on the Heat Pipe Thermal Efficiency. *International Communications in Heat and Mass Transfer*, 35, pp.1316–1319.

Noie, S.H., Heris, S.Z., Kahani, M. & Nowee, S.M., 2009. Heat Transfer Enhancement Using Al2O3/water Nanofluid in a Two-phase Closed Thermosyphon. *International Journal of Heat and Fluid Flow*, 30(4), pp.700–705. http://linkinghub.elsevier.com/retrieve/pii/S0142727X09000563.

Nsofor, E.C. & Gadge, T., 2011. Investigations on the nanolayer heat transfer in nanoparticles-in-liquid suspensions. *ARPN Journal of Engineering and Applied Sciences*, 6(1), pp.21–28.

Oztas, S. & Menlik, T., 2014. Heat Transfer Enhancement Using MgO / Water Nano Fluid in Heat Pipe. , 88, pp.1–11.

Pak, B.C. & Cho, Y.I., 1998. Hydrodynamic and Heat Transfer Study of Dispersed Fluids with Submicron Metallic Oxide Particles. *Experimental Heat Transfer*, 11, pp.151–170.

Patankar, S., 1980. Numerical Heat Transfer and Fluid Flow. In *Series in Computational Methods in Mechanics and Thermal Sciences*. pp. 1–197.

Putra, N., Nata, W., Rahman, H. & Irwansyah, R., 2012. Thermal Performance of Screen Mesh Wick Heat Pipes with Nanofluids. *Experimental Thermal Fluid Science*, 40, pp.10–17.

Putra, N., Roetzel, W. & Das, S.K., 2003. Natural convection of nano-fluids. *Heat and Mass Transfer/Waerme- und Stoffuebertragung*, 39(8-9), pp.775–784.

Riehl, R.R. & Dos, S.N., 2012. Water-copper Nanofluid Application in an Open Loop Pulsating Heat Pipe. *Applied Thermal Engineering*, 42, pp.6–10. http://www.sciencedirect.com/science/article/pii/S1359431111000263.

Schwartz, L.M., Garboczi, E.J. & Bentz, D.P., 1995. Interfacial Transport in Porous Media: Application to DC Electrical Conductivity of Mortars. *Journal of Applied Physics*, 78(10), p.5898. http://link.aip.org/link/JAPIAU/v78/i10/p5898/s1&Agg=doi.

Shabgard, H., Allen, M.J., Sharifi, N., Benn, S.P., Faghri, A. & Bergman, T.L., 2015. Heat pipe heat exchangers and heat sinks: Opportunities, challenges, applications, analysis, and state of the art. *International Journal of Heat and Mass Transfer*, 89, pp.138–158. http://linkinghub.elsevier.com/retrieve/pii/S0017931015005037.

Shabgard, H. & Faghri, A., 2011. Performance Characteristics of Cylindrical Heat Pipes with Multiple Heat Sources. *Applied Thermal Engineering*, 31(16), pp.3410–3419. http://www.sciencedirect.com/science/article/pii/S135943111100336X.

Shafahi, M., Bianco, V., Vafai, K. & Manca, O., 2010a. An Investigation of the Thermal Performance of Cylindrical Heat Pipes Using Nanofluids. *International Journal of Heat and Mass Transfer*, 53(1-3), pp.376–383. http://linkinghub.elsevier.com/retrieve/pii/S0017931009005006.

Shafahi, M., Bianco, V., Vafai, K. & Manca, O., 2010b. Thermal Performance of Flat-Shaped Heat Pipes using Nanofluids. *International Journal of Heat and Mass Transfer*, 53(7-8), pp.1438–1445. http://dx.doi.org/10.1016/j.ijheatmasstransfer.2009.12.007.

Teng, T.P., Hsu, H.G., Mo, H.E. & Chen, C.C., 2010. Thermal Efficiency of Heat Pipe with Alumina Nanofluid. *Journal of Alloys and Compounds*, 504(1), pp.380–384. http://dx.doi.org/10.1016/j.jallcom.2010.02.046.

Tharayil, T., Asirvatham, L.G., Ravindran, V. & Wongwises, S., 2016. Thermal Performance of Miniature Loop Heat Pipe with Graphene–water Nanofluid. *International Journal of Heat and Mass Transfer*, 93, pp.957–968. http://linkinghub.elsevier.com/retrieve/pii/S0017931015305111.

Tillman & Hill, 2007. Determination of Nanolayer Thickness for a Nanofluid. *International Communications in Heat and Mass Transfer*, 34(4), pp.399–407.

Tsai, C.Y., Chien, H.T., Ding, P.P., Chan, B., Luh, T.Y. & Chen, P.H., 2004. Effect of Structural Character of Gold Nanoparticles in Nanofluid on Heat Pipe Thermal Performance. *Materials Letters*, 58(9), pp.1461–1465. http://linkinghub.elsevier.com/retrieve/pii/S0167577X03008036.

Venkatachalapathy, S., Kumaresan, G. & Suresh, S., 2015. Performance Analysis of Cylindrical Heat Pipe Using Nanofluids – An Experimental Study. *International Journal of Multiphase Flow*, 72, pp.188–197. http://www.sciencedirect.com/science/article/pii/S0301932215000270.

Wan, Z., Deng, J., Li, B., Xu, Y., Wang, X. & Tang, Y., 2015. Thermal Performance of a Miniature Loop Heat Pipe Using Water-Copper Nanofluid. *Applied Thermal Engineering*, 78, pp.712–719. http://linkinghub.elsevier.com/retrieve/pii/S1359431114009983.

Xuan, Y. & Li, Q., 2000. Heat Transfer Enhancement of Nanofluids. *International Journal of Heat and Fluid Flow*, 21(1), pp.58–64.

Xue, H.S., Fan, J.R., Hu, Y.C., Hong, R.H. & Cen, K.F., 2006. The Interface Effect of Carbon Nanotube Suspension on the Thermal Performance of a Two-phase Closed Thermosyphon. *Journal of Applied Physics*, 100(10), p.104909. papers2://publication/doi/10.1063/1.2357705.

Yang, X.F. & Liu, Z.H., 2011. Application of Functionalized Nanofluid in Thermosyphon. *Nanoscale Research Letters*, 6(1), p.494. http://www.pubmedcentral.nih.gov/articlerender.fcgi?artid=3212009&tool=pmcentrez&rendertype=abstract.

You, S.M., Kim, J.H. & Kim, K.H., 2003. Effect of Nanoparticles on Critical Heat Flux of Water in Pool Boiling Heat Transfer. *Applied Physics Letters*, 83(16), p.3374. http://scitation.aip.org/content/aip/journal/apl/83/16/10.1063/1.1619206.

Yu, W. & Choi, S.U.S., 2003. The Role of Interfacial Layers in the Enhanced Thermal Conductivity of Nanofluids: A Renovated Maxwell Model. *Journal of Nanoparticle Research*, 5(1-2), pp.167–171.

List of Figures

Figure 1: Two-dimensional axisymmetric configuration of a conventional heat pipe. 66
Figure 2: Case 1 - Wall temperature variation with CuO nanoparticle concentration 67
Figure 3: Case 2 - thermal conductivity variation vs. nanoparticle volume concentration 68
Figure 4: Case 2 - Wall temperature variation with Al_2O_3 nanoparticle concentration 69
Figure 5: Effect of nanoparticle volume concentration on fluid properties 70
Figure 6: Effect of nanoparticle volume concentration on heat pipe performance 71
Figure 7: Effect of evaporator input on heat pipe operation 72
Figure 8: Effect of nanolayer thickness ratio on heat pipe performance 73
Figure 9: Effect of nanoparticle conductivity ratio on on heat pipe performance 74

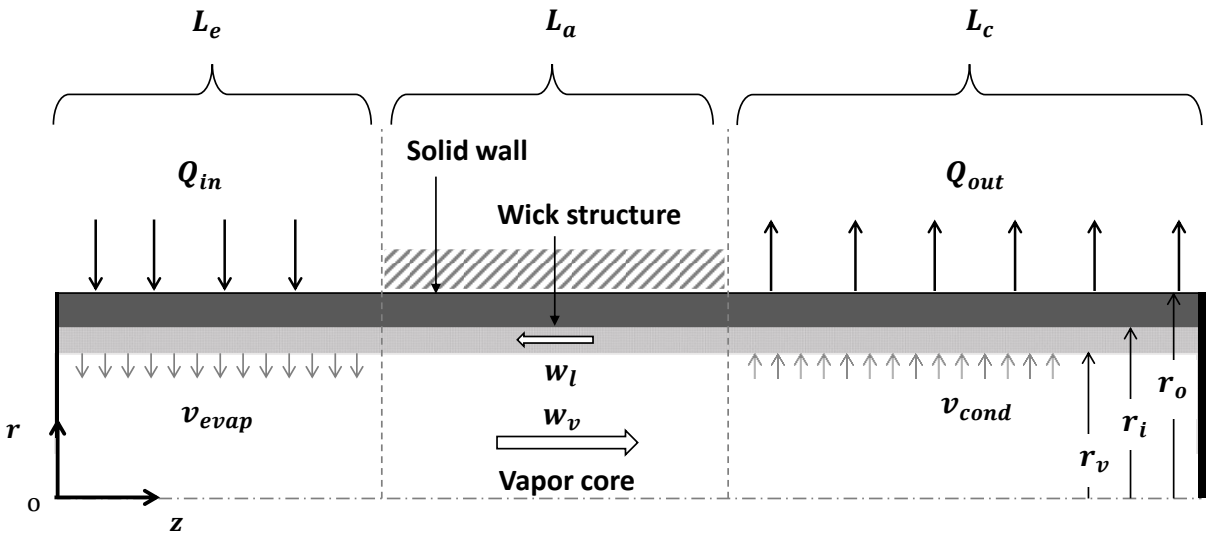

Figure 15: Two-dimensional axisymmetric configuration of a conventional heat pipe.

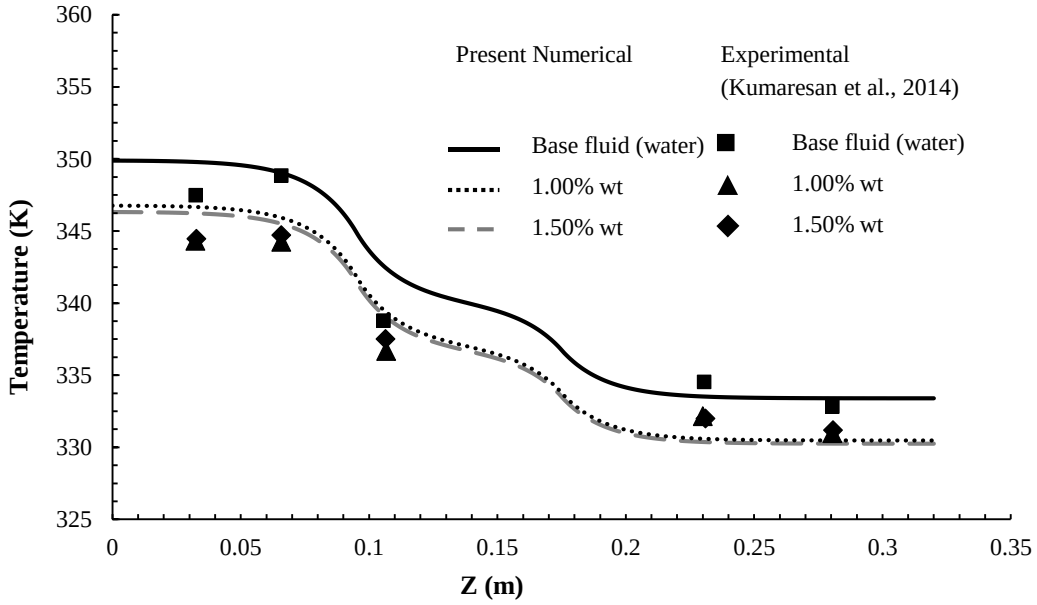

Figure 16: The effect of CuO nanoparticle concentration on outer wall temperature for Case A.

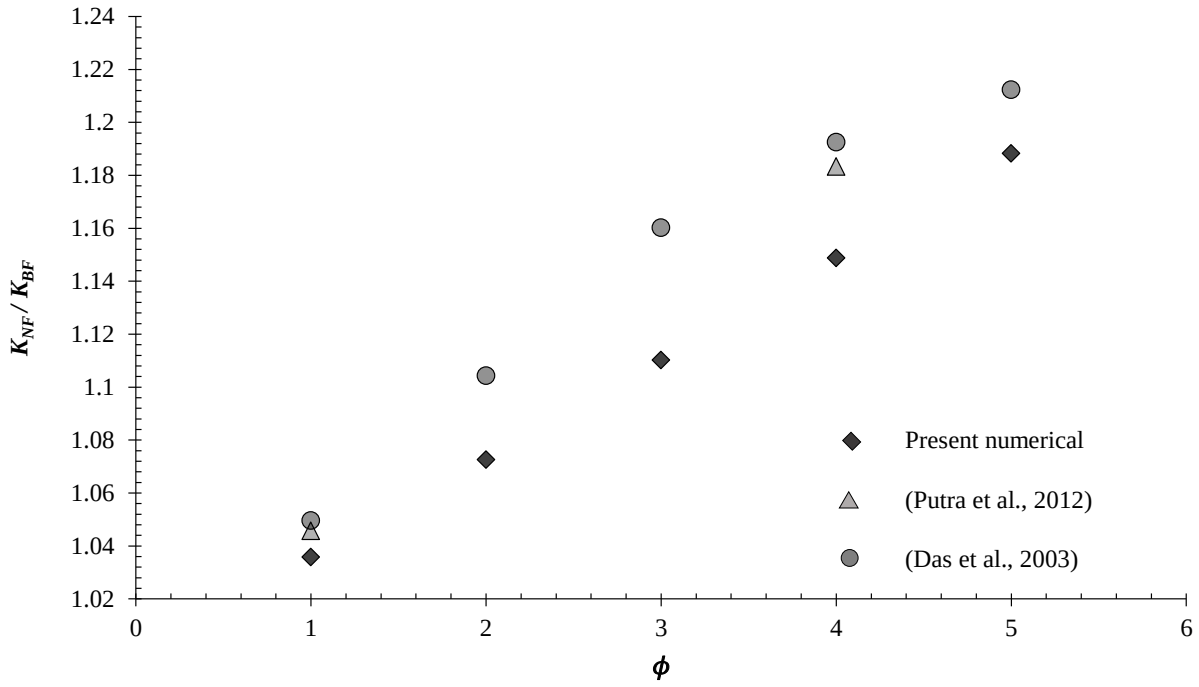

Figure 17: Thermal conductivity enhancement versus Al_2O_3 nanoparticle concentration for Case B.

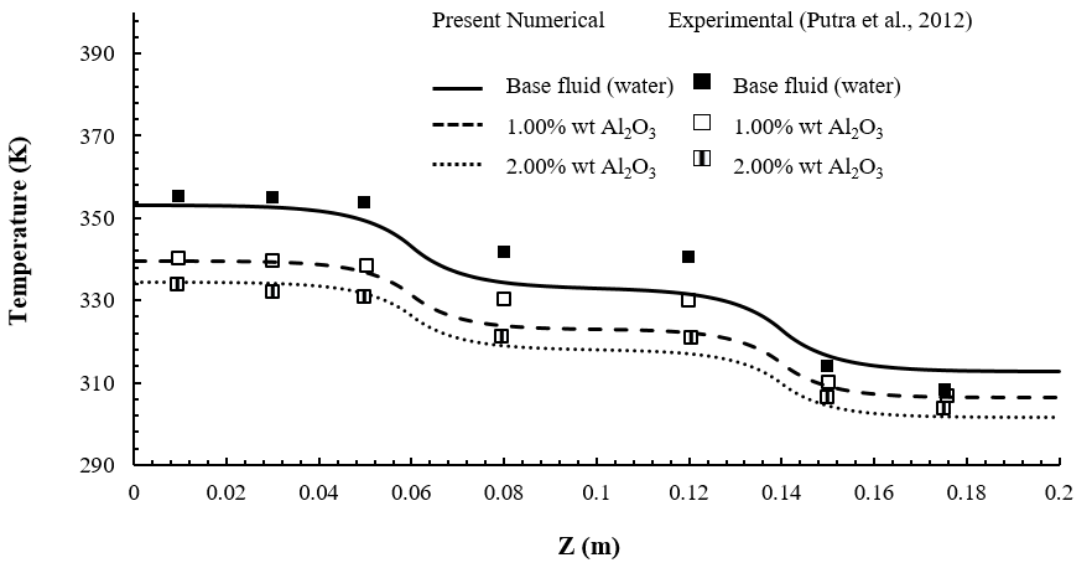

Figure 18: The effect of Al_2O_3 nanoparticle concentration on wall temperature for Case B.

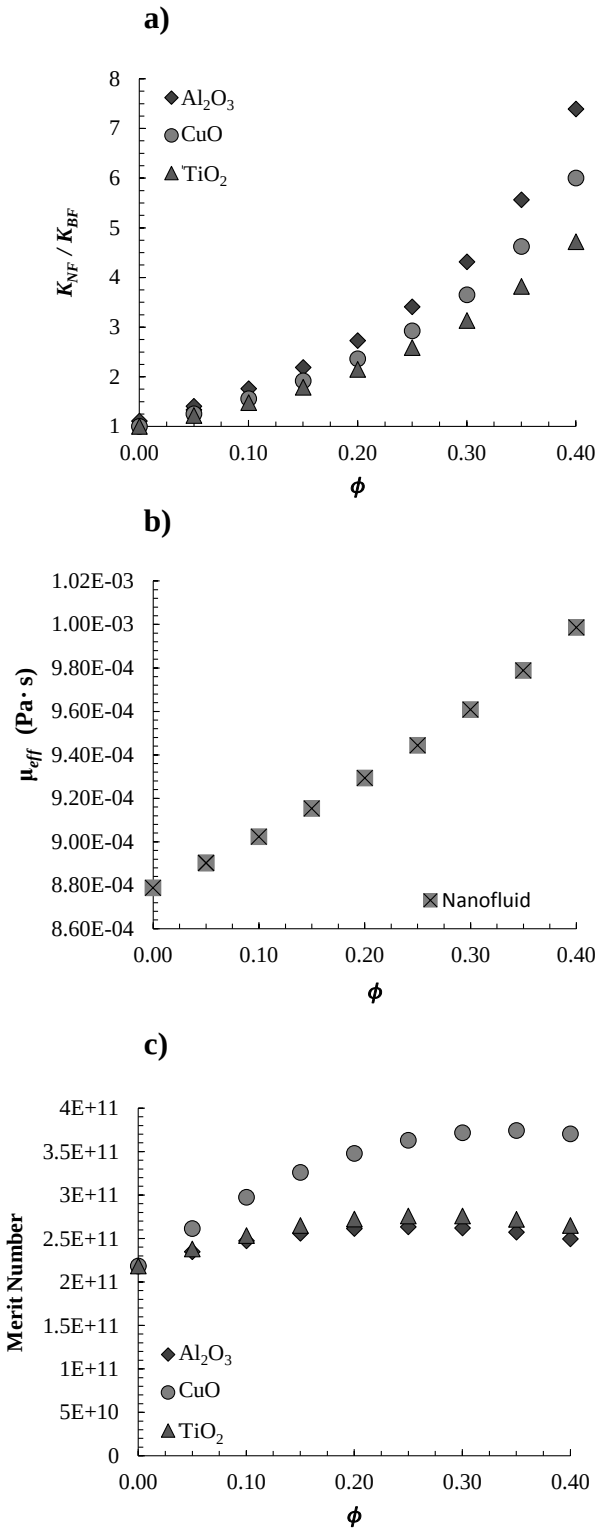

Figure 19: Effect of nanoparticle volume concentration on fluid properties: a) nanofluid to base fluid thermal conductivity ratio b) effective dynamic viscosity c) merit number

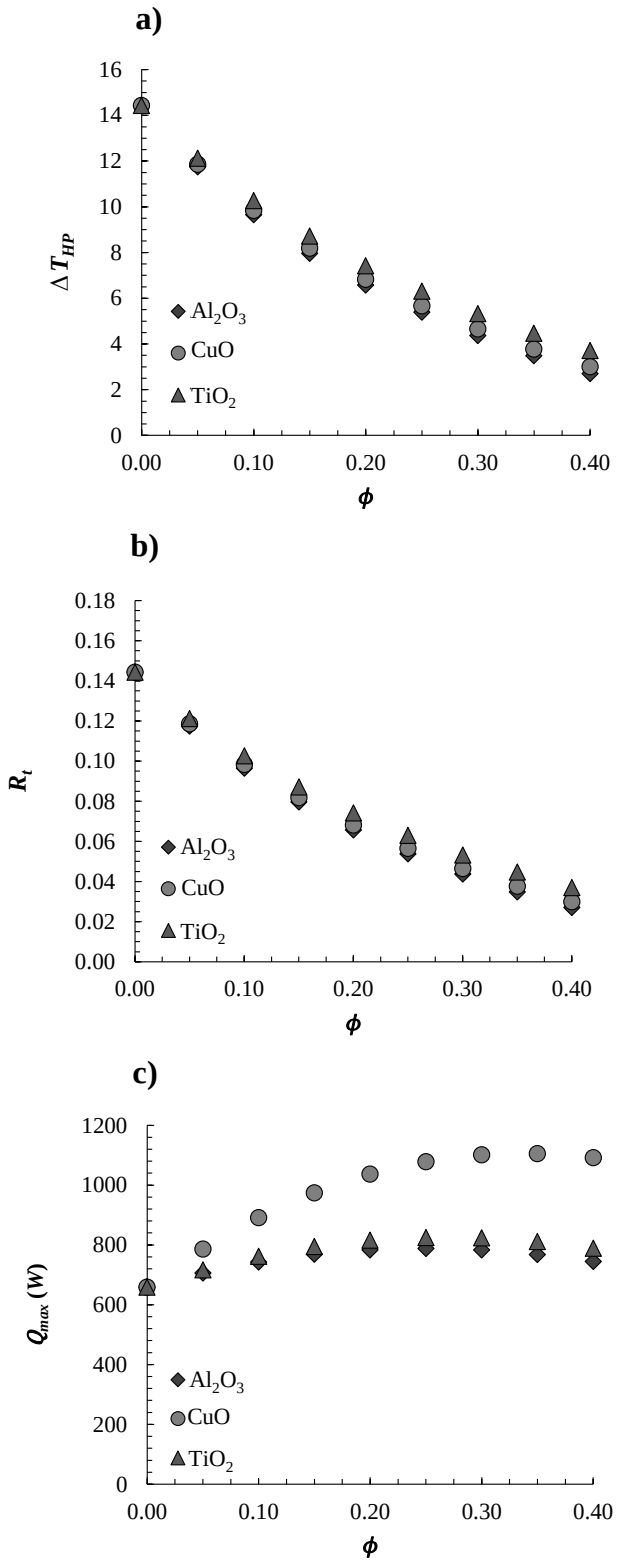

Figure 20: Effect of nanoparticle volume concentration on heat pipe performance: **a)** overall thermal resistance **b)** end to end wall temperature drop **c)** maximum heat input

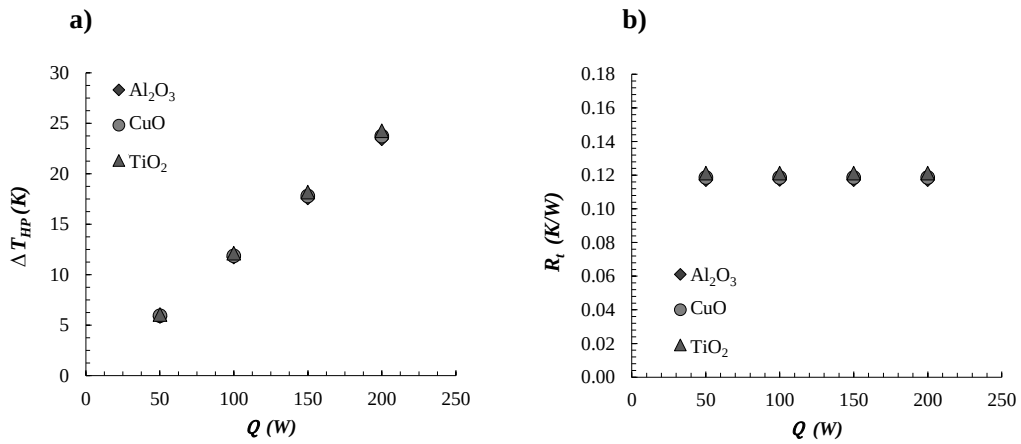

Figure 21: Effect of evaporator input on: **a)** end-to-end wall temperature drop and **b)** overall thermal resistance

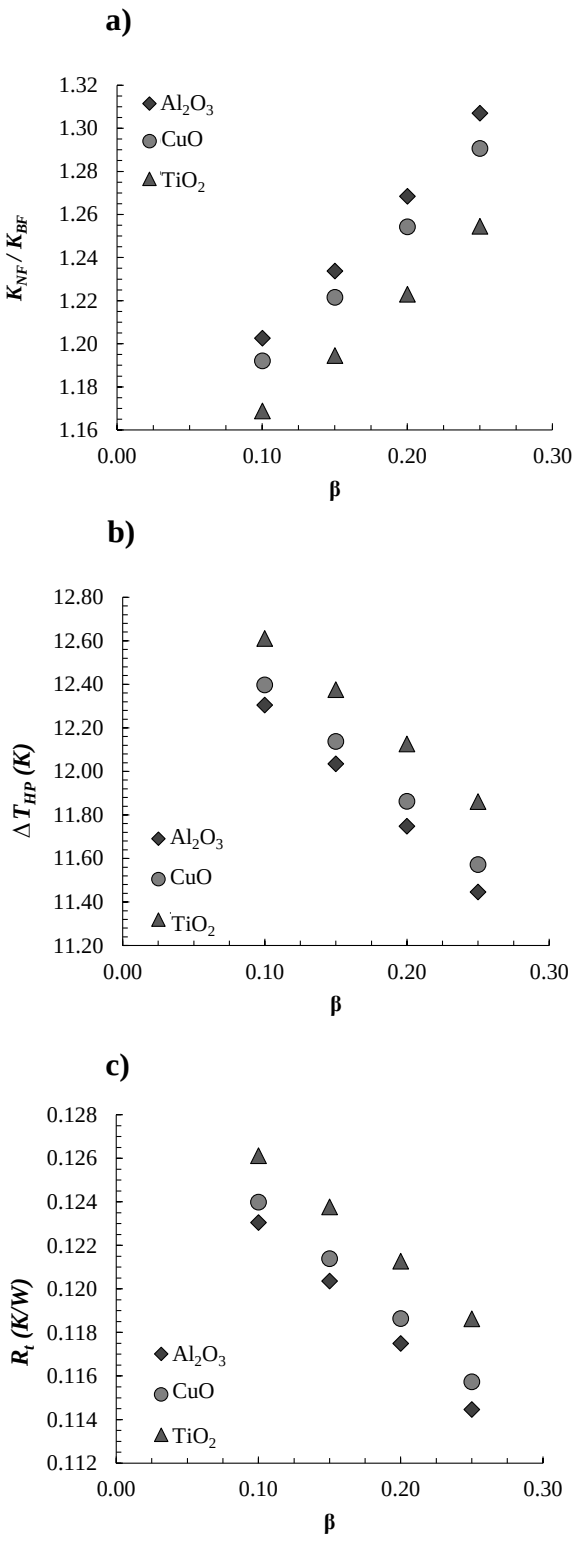

Figure 22: Effect of β on: **a)** nanofluid to base fluid thermal conductivity ratio **b)** end to end wall temperature drop **c)** overall thermal resistance

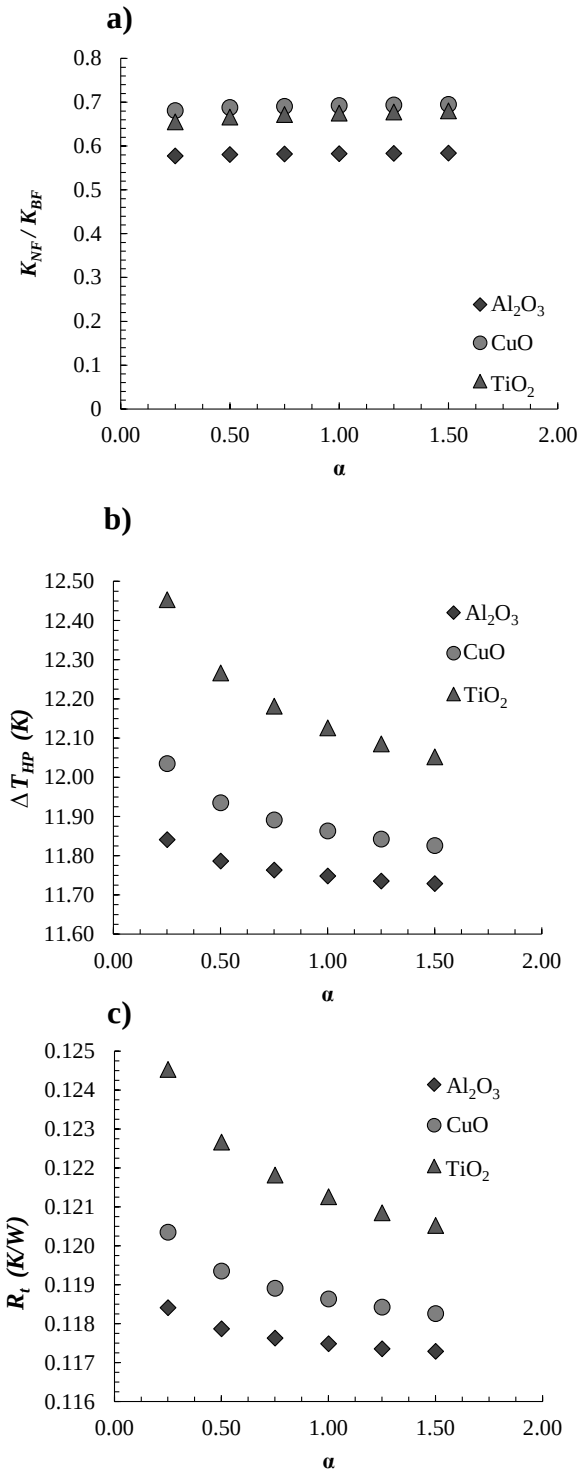

Figure 23: Effect of α on nanoparticle conductivity ratio on: **a)** nanofluid to base fluid thermal conductivity ratio **b)** end to end wall temperature drop **c)** overall thermal resistance

List of Tables

Table 1: Experimental and Theoretical Studies of the Effect of Nanofluid/Particles in Heat Pipes. 76
Table 2: Heat Pipe and Working Fluid Properties, Dimensions and Operating Conditions. 84
Table 3: Dimensions and Specifications for Parametric Study Heat Pipe 85
Table 4: Parametric Study Parameters and Properties 86

Table 8: Experimental and Theoretical Studies of the Effect of Nanofluid/Particles in Heat Pipes.

Investigator, Year (Type)	Working Fluid	Nanoparticle Concentration	HP Type and Dimensions	Thermal Resistance	Comments
Tsai et al., 2004 (Experimental)	Au-H_2O d_{NP} (nm): 21.3, 8.0, 9.3, 15.6, 43.7	Original mass concentration (mg/L): $HAuCl_4$: 1.0 $Na_3C_6H_5O_7$: 1.0 $C_{76}H_{52}O_{46}$: 1.0 K_2CO_3: 2.5mM	Conventional Cylindrical HP $L_e = 30$ mm $L_a = 90$ mm $L_c = 50$ mm $D_o = 6$ mm	• $R_t = 0.17$, permanent precipitation to solid, $0.20, 0.206, 0.215$ (0.27 °C/W for water-filled HP) • Maximum reduction in R_t of 37% ($d_{NF} = 21.3$ nm) compared to water-filled HP	• All nanofluids effectively lowered the thermal resistance compared to the same charge volume of water • Aggregation of Au nanoparticles increased with higher $[HAuCl_4]$. Higher $[C_{76}H_{52}O_{46}]$ prevented formation of large Au nanoparticles • Recommended use of monodispersed particles over aggregated nanoparticles
Kang et al., 2006 (Experimental)	Ag-H_2O d_{NP} (nm): 10, 35	Mass concentration (mg/L): 1, 10, 50, 100	Conventional Cylindrical HP $L = 200$ mm $D_o = 6.0$ mm	• R_t decreased 10 – 80% compared to the water-filled HP at a Q_{in} of 30 – 60 W • R_t decreased with increased NP diameter and concentration • R_t for 10 nm NPs was 52% lower than for water at a Q_{in} of 50 W, and for 35 nm NPs, R_t was 81% lower at a Q_{in} 40 W	• Grooved wick (211 x 217 µm) • Ag nanoparticles were produced by catalytic chemical vapor deposition • Wall temperature was lower for increased [Ag] • Change in wall temperature between evaporator and condenser decreased as [Ag] increased • No further lowering of wall temperature was observed for [Ag] > 50 mg/L
Xue et al., 2006 (Experimental)	Carbon nano-tubes-H_2O d(nm): 15 L(µm): 10	Volume %: 1.0	Conventional Cylindrical TS $D_i = 20.0$ mm $t_w = 2.5$ mm	• R_t decreased with increasing Q_{in} • At a Q_{in} of 250 W and [NP] of 1.0 vol.%, R_t was about 0.0275 °C/W, compared to 0.013 °C/W for water-filled HP • At a Q_{in} of 555 W and [NP] of 1.0 vol.%, R_t was about 0.020 °C/W, compared to 0.006 °C/W for water-filled HP	• High evaporator and incipience temperatures, and increased R_t lowered the thermal performance of NF-filled thermosyphon • Carbon nanotubes increased surface tension, and decreased contact angle • Decreased cavity site density and bubble detachment frequency lowered heat transfer
Lin et al., 2008 (Experimental)	Ag-H_2O d_{NP} (nm): 20	Mass concentration (mg/L): 100, 450	Loop HP $D_o = 3.0$ mm $D_i = 2.45$ mm $L_e = 22.0$ mm $L_a = 113.0$ mm $L_c = 35.0$ mm 10 parallel tubes	• For a FR of 0.60, and a Q_{in} of 85 W, R_t was reduced 0.092 °C/W (ΔT_{ec} was 7.79 °C lower) compared to a water-filled HP • For a FR of 0.80, a Q_{in} of 85 W, and: $[Al_2O_3]$ of 450 mg/L, $R_t \approx 0.95$ °C/W $[Al_2O_3]$ of 100 mg/L, $R_t \approx 0.75$ °C/W water-filled, $R_t \approx 0.80$ °C/W	• Tested FRs of 0.20, 0.40, 0.60, and 0.80 • Fill ratios of 0.40 and 0.60 showed best thermal performance of HP, and with a $[Al_2O_3]$ mg/L • At a $[Al_2O_3]$ of 450 mg/L, the increased viscosity of the working fluid hindered bubble formation and decreased bubble transport

Table 1 **(**Continued).

Investigator, Year (Type)	Working Fluid	Nanoparticle Concentration	HP Type and Dimensions	Thermal Resistance	Comments
Mehta & Khandekar, 2007 (Experimental)	Al_2O_3, CuO, Laponite clay, -H_2O d_{Al2O3}= 40-47 nm d_{CuO}= 8.6-13.5nm d_{clay}= 25 nm	Weight %: 1.0	Conventional Cylindrical TS $D_o = 19.0$ mm $D_i = 16.0$ mm $L_e = 120.0$ mm $L_a = 200.0$ mm $L_c = 300.0$ mm	• Reduced thermal performance (higher R_t was observed for all nanofluids tested) • At a Q_{in} of 40 W and [NP]= 1.0 wt.%, $R_t \approx 0.106$ ºC/W (Laponite clay) $R_t \approx 0.088$ ºC/W (CuO-H_2O) $R_t \approx 0.075$ ºC/W (Al_2O_3-H_2O) $R_t \approx 0.068$ ºC/W (H_2O)	• All nanofluids showed inferior thermal performance compared to water • Wettability increased for all nanofluids • Presence of NPs caused adverse effects to bubble departure, diameter, frequency and nucleation site density • Adverse effects outweighed the relative increase in effective thermal conductivity of NFs
Naphon et al., 2008 (Experimental)	Ti-C_2H_6O, C_2H_6O, H_2O d_{NP} (nm): 21	Volume %: 0.01, 0.05, 0.10, 0.50, 1.0	Conventional Cylindrical HP $L_e = 20$ cm $L_a = 20.0$ cm $L_c = 20$ cm $D_o = 15$ mm	• R_t decreased with greater tilt angle due to a thinner liquid film • Higher thermal efficiency (lower R_t) for increased [Ti-C_2H_6O]. At a [Ti-C_2H_6O] of 0.10 vol.% the max increase in thermal efficiency was 10.60% (over base fluid efficiency)	• Increased thermal efficiency for tilt angles < 60º for water and < 45º for alcohol • At [Ti-C_2H_6O] > 0.10 vol.%, properties of nanofluids resembled those of solids
Kang et al. 2009 (Experimental)	Ag-H_2O d_{NP} (nm): 10, 35	Mass concentration (mg/L): 1.0, 10, 100	Conventional Cylindrical HP $L_e = 40$ mm $L_a = 60$ mm $L_c = 100$ mm $D_o = 6.0$ mm	• At a Q_{in} range of 30 to 50 W, the evaporator and condenser temp. difference decreased (lower R_t) by 0.56 - 0.65 ºC compared to the water-filled HP • At a Q_{in} of 60 W, the water-filled HP had a ΔT_{ec} of 10 ºC, compared to a ΔT_{ec} of less than 1.2 ºC for all NF-filled HPs	• Sintered copper wick, $t_{wick} = 1$ mm • NF-filled HP functioned at a Q_{in} of up to 70 W (20 W higher than for water-filled HP) • Only a slightly lower ΔT_{ec} observed for 35 nm and 10 nm nanoparticles
Noie et al., 2009 (Experimental)	Al_2O_3 -H_2O d_{NP} (nm): 20	Volume %: 1.0, 1.5, 2.0, 2.5, 3.0	Conventional Cylindrical TS $D_i = 20.0$ mm $L = 1000.0$ mm $L_e = 350.0$ mm $L_a = 250.0$ mm $L_c = 400.0$ mm $t_w = 1.0$ mm	• Decreased ΔT_{ec} for all [Al_2O_3] compared to the water-filled HP (lower R_t for all [Al_2O_3]) • Major thermal resistance is attributed to bubble formation at liquid-solid interface. • Nanoparticle bombardment and additional nucleation sites lower R_t	• At a Q_{in} of 97.1 W, and [Al_2O_3] of 0.10 vol.%, thermal efficiency increased from 75.1% (water-filled TS) to 81.56% (with nanofluid) and increased further with higher [Al_2O_3] • At a Q_{in} of 97.1 W and [Al_2O_3] of 0.20 vol.%, thermal efficiency increased 14.7% • Enhancement depends on particle type, size, base fluid, and bubble nucleation size

Table 1 **(**Continued).

Investigator, Year (Type)	Working Fluid	Nanoparticle Concentration	HP Type and Dimensions	Thermal Resistance	Comments
Do & Jang, 2010 (Analytical)	Al_2O_3 -H_2O d_{NP} (nm): 10, 20, 30, 40, 50, 60	Volume %: 0.3	Flat Plate HP $L_e = 15.6$ mm $L_a = 70.0$ mm $L_c = 34.4$ mm $W = 13.41$ mm $D = 8.92$ mm $H = 0.42$ mm $t = 0.10$ mm $N = 62$	• Model I ($R_t \approx 0.097$ °C/W) showed higher thermal resistance than Model II ($R_t \approx 0.058$ °C/W) • Thermal resistance of condensation was similar for Models I, II, and H_2O-filled HP ($R_{cond} \approx 0.2$ °C/W) • Thermal resistance of evaporation decreased for Model I and II, respectively ($R_{evap,BF} \approx 0.09$, $R_{evap,Model\ I} \approx 0.08$, $R_{evap,Model\ II} \approx 0.04$ °C/W)	• Model I accounts for nanofluid enhancement by changes to effective properties (k, μ, and ρ) • Model II considers deposition of a thin porous NP coating layer in the heat pipe evaporator • Increased volume fraction caused increased thermal conductivity and viscosity of the NF • Optimum volume fraction was identified (0.3 vol. %) for ($T_v = 90$ °C, $Q_{in} = 40$ W) • Thermal resistance decreased for increasing nanoparticle diameter
Shafahi et al., 2010a (Analytical)	Al_2O_3, TiO_2, CuO, d_{NP} (nm): 10, 20, 40	Volume %: 0, 2.0, 3.0, 4.0, 10, 20	Conventional Cylindrical HP $D_o = 19.1$ mm $D_i = 18.8$ mm $D_v = 17.3$ mm $L = 89.0$ cm $L_e = 60.0$ cm $L_a = 9.0$ cm $L_c = 20.0$ cm	• Increased [NP] decreased HP thermal resistance • Thermal resistance decreased with higher heat input at the evaporator for all NFs • CuO NPs had the lowest thermal resistance of all NPs ($R_{CuO}/R_{BF} \approx 0.94$, $R_{Al2O3}/R_{BF} \approx 0.95$, $R_{TiO2}/R_{BF} \approx 0.97$) for a vol. % of 1.0) • For a vol. % of 4.0 CuO (d_{NP}=10 nm), thermal resistance was reduced by 75 %	• The maximum liquid velocity in the wick decreased with increased particle concentration • Overall heat transfer of the heat pipe increased with higher nanoparticle concentrations • At a critical concentration level, higher viscosity of the NF results in a higher liquid pressure drop, and decreased thermal performance • Smaller diameter particles had a greater effect on the end-to-end temperature drop of the heat pipe
Teng et al., 2010 (Experimental)	Al_2O_3-H_2O d_{NP} (nm): 10, 35	Weight %: 0.5, 1.0, 3.0	Conventional Cylindrical HP $L = 600$ mm $D_i = 16.0$ mm	• Thermal efficiency increased by 16.8% for all NF-filled HPs (lower R_t) compared to water-filled HPs • Thermal efficiency decreased (increased R_t) at excessively high [Al_2O_3] due to solid phase of the base fluid	• Al_2O_3 nanoparticles prepared by direct synthesis • Optimum FR was found to be 0.60 • Evaporation occurred more readily at low [Al_2O_3] • Optimum FR decreased with increased [Al_2O_3]
Liu & Zhu, 2011 (Experimental)	CuO-H_2O d_{NP} (nm): 50	Weight %: 0.5 – 2.0 Volume %: 0.078 – 0.310	Conventional Cylindrical HP $L_e = 100$ mm $L_a = 100$ mm $L_c = 150$ mm $D_o = 8.0$ mm $D_i = 6.8$ mm	• R_t decreased by 60% at an operating pressure of 7.45 kPa and heat flux < 44 KW • For a Q_{in} of 20 W and[CuO] of 1.0 vol.% $R_t \approx 0.60$ °C/W (1.20 °C/W for H_2O) • For a range of [CuO] from 0 to 1.0 wt.%, R_t decreased with increased heat flux, and increased at greater [CuO]	• 2-layer copper mesh wick (mesh number = 160) • Three steady state operating pressures were studied (19.97, 12.38, and 7.45 KPa) • Optimal mass concentration of NP was 1.0% • Increased heat transfer for low heat fluxes, but decreased for moderate and high heat flux (at all operating pressures)

Table 1 **(**Continued).

Investigator, Year (Type)	Working Fluid	Nanoparticle Concentration	HP Type and Dimensions	Thermal Resistance	Comments
Mousa, 2011 (Experimental)	Al_2O_3,-H_2O d_{NP} (nm): 40	Volume %: 0.25 – 1.5	Conventional Cylindrical HP $L_e = 60.0$ mm $L_a = 40.0$ mm $L_c = 60.0$ mm $D_{a,o} = 20.0$ mm $D_{e,o} = 40.0$ mm $D_{c,o} = 40.0$ mm	• R_t decreased with increased $[Al_2O_3]$ and compared to water-filled HP • R_t decreased for FRs increasing to 0.45 (optimum FR), and increased for higher FRs • For a FR of 0.45, and a $[Al_2O_3]$ of 1.20 vol.%, the maximum R_t decreased by 62.60%	• Tested fill ratios of 0.2, 0.4, 0.45, 0.50, 0.55, 0.60, 0.65, 0.70, 0.80, and 1.0 • Improved nucleate boiling and nanoparticle deposition in the wick increased wettability • Increased effective conductivity of working fluid minimized temp. gradient between evaporator and condenser • Developed an experimental correlation based on heat input, fill ratio, and Prandtl number
Yang & Liu, 2011 (Experimental)	SiO_2, SiO_2+SiH_4, -H_2O d_{NP} (nm): 30	Weight %: 0.5, 1.0, 1.5, 2.0, 2.5	Rectangular TS $L_e = 100.0$ mm $L_a = 100.0$ mm $L_c = 150.0$ mm $D_h = 8.0$ mm	• Evaporating HTC increased (decreased R_t) for functualized nanofluids • Max increase in evaporating HTC of 17% for functualized nanofluids • For conventional NF, the evaporating HTC decreased 7, 9, and 11 % for operating pressures (7.38, 15.75, and 31.18 kPa, respectively)	• SiO_2 nanoparticles were functualized by grafting polar silane (SiH_4) to nanoparticles • Conventional SiO_2 (non-functualized) left porous deposition layer in evaporator • Maximum heat flux of functualized NF was similar to that of water (no enhancement) • Functualized NPs kept good dispersion after inactivity (no sedimentation was observed)
Riehl & Dos, 2012 (Experimental)	Cu-H_2O d_{NP} (nm): 29	Weight %: 5.0	Loop HP $D_i = 1.5$ mm $L_e = 100.0$ mm $L_a = 100.0$ mm $L_c = 100.0$ mm 13 parallel tubes	• R_t increased for nanofluid-filled HP compared to water-filled HP • At [Cu] of 5.0 wt.% and a Q_{in} of 50 W, • $R_t \approx 0.68$ °C/W (1.04 °C/W for water-filled HP)	• NPs acted as nucleation sites, intensified bubble generation and deployment; the water-filled HP did not illustrate temperature oscillations • Condenser stabilized at 90 °C for NF-filled HP, lower than the 118 °C for water-filled HP • NFs decreased critical bubble diameter, improving thermal performance
Gunnasegaran et al., 2013 (Experimental, Numerical)	SiO_2-H_2O d_{NP} (nm): 12	Weight %: 3.0	Loop HP Evaporator: 50 x 50 x 4 mm Condenser: 321 x 100 x1 mm	• R_t decreased with increasing Q_{in} • Nanofluids showed lower R_t than water-filled HP for all heat loads • At a Q_{in} of 100 W, $R_t = 1.304$ °C/W (1.480 °C/W for water-filled HP) Average R_t decreased 28-44 % for a range of Q_{in} from 20-100 W	• Increased Q_{in} caused flow in the vapor line to transition from bubbly, to slug, to annular flow • NF-filled HP had decreased nucleation size of vapor bubbles, attributed to NP bombardment • A corresponding numerical simulation used the Finite Element Method to obtain transient and steady state temp. distributions in the LHP

Table 1 **(**Continued).

Investigator, Year (Type)	Working Fluid	Nanoparticle Concentration	HP Type and Dimensions	Thermal Resistance	Comments
Huminic & Huminic, 2013 (Experimental)	FeO_2-H_2O d_{NP} (nm): 4-5	Volume %: 2.0, 5.3	Conventional Cylindrical TS $D_i = 15.0$ mm $L = 2000.0$ mm $L_e = 850.0$ mm $L_a = 300.0$ mm $L_c = 850.0$ mm $t_w = 0.7$ mm	• R_t decreased with increased [FeO_2] and greater inclination angle • At a tilt of 45° and [FeO_2] of 2.0 vol.%, heat transferred by the TS increased by 19% compared to the water-filled TS • At a tilt of 90° and [FeO_2] 2.0 vol.%, heat transferred by the TS increased by 39% compared to the water-filled TS	• FeO_2 nanoparticles obtained by laser pyrolysis • A major internal thermal resistance is due to formation of vapor bubbles at the liquid-solid interface • Nanofluids cause improved thermal performance by bombarding vapor bubbles and thus require smaller nucleation sites
Kole & Dey, 2013 (Experimental)	Cu-H_2O d_{NP} (nm): 40	Weight %: 0.0005, 0.005, 0.05, 0.5	Conventional Cylindrical HP $L_e = 70.0$ mm $L_a = 80.0$ mm $L_c = 150.0$ mm $D_o = 10.0$ mm $t_w = 0.60$ mm	• R_t of the vertical HP with a [Cu] of 0.5 vol.% decreased approximately 27% compared to the water-filled HP at all applied Q_{in} • High R_t was observed for all HPs at low heat flux, decreased R_t at higher heat fluxes	• Q_{in} was applied from 10-100 W with 10 W step • Maximum enhanced effective conductivity by 15% for a [Cu] of 0.5 vol.% (compared to the water-filled HP) • Lower evaporator wall temperature was observed for NF-filled HPs, due to deposition of a Cu nanoparticle layer on the screen wick
Buschmann & Franzke, 2014 (Experimental)	TiO_2, Au, -H_2O d_{NP} (nm): 85	Volume %: [TiO_2]= 0.1, 0.2, 0.3, 0.4 [Au]=2.84x10^{-4}	Conventional Cylindrical TS $D_i = 25$ mm $L = 500.0$ mm $L_e = 22.0$ mm $L_a = 378.0$ mm $L_c = 100.0$ mm	• Minimum R_t occurred at a [TiO_2] between 0.20 and 0.30 vol.% • At a higher [TiO_2] than optimum, R_t remained constant or increased • Maximum decrease in R_t of 24.0% compared to water-filled TS • Lessened effect of NFs at high Q_{in} (R_t for nanofluids and water were about equal)	• Nanoparticle layer deposition in evaporator • Gold based nanofluid indicated no vapor transport of nanofluids to condenser region • For the higher [TiO_2] of 0.30 and 0.40 vol.%, more massive particle layers were deposited in evaporator than for [TiO_2] of 0.10 and 0.20 vol.% • After 5 weeks, [TiO_2] of 0.3 and 0.4% did not show the thermal improvement that was observed for fresh nanofluid solution
Grab et al., 2014 (Experimental)	TiO_2, Au, -H_2O d_{NP} (nm): TiO_2: 85 Au: 16, 66	Volume %: [TiO_2]= 1.1, 0.2 [Au]= 5.20x10^{-4}	Conventional Cylindrical TS $D_i = 108$ mm $L = 1440.0$ mm $L_e = 40$ mm (x4) $L_a = 1000$ mm $L_c = 400.0$ mm	• R_t decreased for increased Q_{in} • Difference in R_t compared to water-filled TS decreased for increased Q_{in} • At a Q_{in} of 50 W and a [TiO_2] of 0.20 vol.%, $R_t = 0.165$ °C/W (0.185 °C/W for water-charged TS) • At a Q_{in} of 50 W and a [Au]= 5.20x10^{-4} vol.%, $R_t = 0.145$ °C/W (0.170 °C/W for water-filled TS)	• Used video recordings for *in situ* observation of nanofluid behavior • Effective thermal conductivity increased for all nanofluid cases (from 0.26 to 0.59%) • Deposition of the time-dependent nanoparticle layer in evaporator was observed. No transport of nanoparticles in the vapor flow was observed • Doubling of [NP] did not affect deposition of the porous layer

Table 1 **(**Continued).

Investigator, Year (Type)	Working Fluid	Nanoparticle Concentration	HP Type and Dimensions	Thermal Resistance	Comments
Ghanbarpour & Khodabandeh, 2015 (Analytical, Experimental)	Al_2O_3, TiO_2, -H_2O d_{NP} (nm): Al_2O_3: 235 TiO_2: 120	Volume %: Al_2O_3: 1-5.0 TiO_2: 1-5.0	Conventional Cylindrical HP $L_e = 20$ mm $L_a = 100$ mm $L_c = 50$ mm $D_o = 6.35$ mm $t = 0.71$ mm	• R_t and entropy generation decreased with increased [Al_2O_3] and [TiO_2] • Analytical results: [Al_2O_3] of 1.0, 3.0, 5.0 vol.%, $R_t \approx$ 0.156, 0.145, 0.139 °C/W [TiO_2] of 1.0, 3.0, 5.0 vol.%, $R_t \approx$ 0.158, 0.149, 0.136 °C/W	• Thermal conductivity and viscosity of both nanofluids increased with NP concentration • Entropy generation due to temperature gradients between the HP vapor and external reservoirs is due to the liquid pressure drop, and influenced by NPs. Entropy generation due to vapor pressure drop is unaffected by NPs. • Entropy generation decreased 3-13.5% for [NF]
Ghanbarpour et al. 2015 (Experimental)	Ag-H_2O d_{NP} (nm): 165	Mass %: 0.25, 0.5, 0.75	Conventional Cylindrical HP $L_e = 30$ mm $L_a = 190$ mm $L_c = 30$ mm $R_o = 3.2$ mm $R_i = 3.0$ mm $R_v = 2.9$ mm	• R_t decreased with increased [Ag] • At horizontal, Q_{in} of 100 W, and [Ag] 0, 0.25, 0.5, 0.75 mass%: $R_t \approx$ 0.096, 0.090, 0.084, 0.078 °C/W • At vertical, Q_{in} of 100 W, and [Ag] 0, 0.25, 0.5, 0.75 mass%: $R_t \approx$ 0.087, 0.084, 0.072, 0.066 °C/W	• Increased [Ag] decreased the solid-liquid contact angle, resulting in increased capillary force • Enhanced evaporator heat transfer coefficient by 18, 22, and 10% for inclination angles of 30, 60 and 90° compared to that at horizontal • Maximum heat flux increased 18-32% when using NF compared to basefluid
Kim et al., 2015 (Experimental)	SiC-H_2O	Volume %: 0.01, 0.1	Conventional Cylindrical HP $L_e = 350$ mm $L_a = 150$ mm $L_c = 500$ mm $R_o = 19$ mm $R_i = 17.4$ mm	• Increased Q_{in} showed reduced R_t • At a Q_{in} of 100 W and [SiC] of 0.10 vol.%: $R_t = 0.480$ °C/W (0.510 °C/W) for water-filled HP $R_{evap} = 0.340$ °C/W (0.210 °C/W) for water-filled HP $R_{cond} = 0.450$ °C/W (0.470 °C/W) for water-filled HP	• SEM images of wick showed NP deposited layer • Decreased boiling heat transfer, unchanged condensation heat transfer for NF-filled HPs • Thick NP deposition, large- sized bubble formation and decreased departure frequency increased R_{evap} • Enhanced wettability resulted and easier film formation increased R_{cond}
Mashaei & Shahryari, 2015 (Analytical)	Al_2O_3, TiO_2, -H_2O d_{NP} (nm): 10, 20, 40	Volume %: 2.0, 4.0, 8.0	Conventional Cylindrical HP $L_e = 0.01$ mm $L_a = 0.05$ mm $L_c = 0.15$ mm $D_o = 15.8$ mm $D_i = 14.0$ mm $D_v = 11.0$ mm	• Increased [NP] reduced thermal resistance • Larger NP diameter caused higher R_t • R_t decreased for [Al_2O_3] = 2.0, 4.0, and 8.0 vol.% by 16.8%, 27.6%, and 44.8%, respectively (d_{NP} = 10 nm) • R_t increased for d_{NP} = 10, 20, and 40 nm by 44.8%, 32.6%, and 23.47%, respectively	• Performance of a NF charged heat pipe were compared to a water–filled HP for equal Q_{in} • Evaporator wall temperature was decreased • The effect of particle size was less significant as the particle size increased • NP type showed less importance compared to particle concentration and size

Investigator, Year (Type)	Working Fluid	Nanoparticle Concentration	HP Type and Dimensions	Thermal Resistance	Comments
Wan et al., 2015 (Experimental)	Cu-H_2O d_{NP} (nm): 50	Weight %: 1.0, 1.5, 2.0	Miniature Loop HP Evaporator: 55 x 50 x 18 mm Condenser: 76 x 80 x 95 mm	• Decreased R_t by 21.7 % as compared to water charged HP • At a Q_{in} of 100 W and [Cu] of 1.5 wt.%, $R_t = 0.065$ °C/W • At a Q_{in} of 150 W and [Cu] of 1.0 wt.%, $R_t = 0.053$ °C/W At a Q_{in} of 150 W and [Cu] of 1.5 wt.%, $R_t = 0.039$ °C/W At a Q_{in} of 150 W and [Cu] of 2.0 wt.%, $R_t = 0.077$ °C/W	• Thermal performance improved with increasing [Cu] due to reduced contact angle, enhanced boiling heat transfer, and NP deposition • At a Q_{in} of 100 W and [Cu] of 1.0 wt.%, the evaporator wall temperature decreased by 12.8%, and the overall HTC decreased by 19.5% • Correct LHP function occurred at a lower $T_{e,w}$ when using nanofluid versus water-filled HP ($T_{e,w} = 66.1, 75.8$, respectively)
Kim & Bang, 2016 (Experimental)	Graphene oxide - H_2O sheet LxW (nm): 1 x 350	Volume %: 0.01, 0.03	Conventional Cylindrical HP $L_e = 215$ mm $L_a = 285$ mm $L_c = 500$ mm $D_o = 25.4$ mm $D_i = 22.0$ mm	• Evaporator thermal resistance was lowered by ≈ 25% compared to water-filled HP • Similar condenser thermal resistances for both nanofluid and water-filled HP • At Q_{in} of 300 W and [GO-H_2O] of 0 vol.%, $R_e \approx 0.055$ °C/W At Q_{in} of 350W and [GO-H_2O] of 0.01 vol.%, $R_e \approx 0.048$ °C/W At Q_{in} of 350W and [GO-H_2O] of 0.03 vol.%, $R_e \approx 0.043$ °C/W	• 0.01% had lower thermal resistance and better boiling heat transfer than 0.03 vol.%, attributed thickness of nanoparticle deposition in the evaporator wick • Increased thermal resistance with [NP] due to large sized bubbles at the hydrophobic surfaces of the GO nanoparticles, compared to the hydrophilic wick structure • Capillary limit increased for GO-H_2O filled HP due to decreased radius of capillary pores and menisci in the wick
Tharayil et al. 2016 (Experimental)	Graphene-H_2O sheet LxW (nm): 1-5 x 130	Volume %: 0.003, 0.006, 0.009	Miniature Loop HP Evaporator: 20 x 20 x 7.5 mm Condenser: 140 x 60 x 40 mm	• The lowest thermal resistance of 0.083 °C/W was obtained at 380 W at optimal concentration of 0.006% and 30% FR • At Q_{in} of 380 W and [G- H_2O] of 0 vol.%, $R_t \approx 0.113$ °C/W At Q_{in} of 380 W and [G- H_2O] of 0.003 vol.%, $R_t \approx 0.105$ °C/W At Q_{in} of 380 W and [G- H_2O] of 0.006 vol.%, $R_t \approx 0.100$ °C/W At Q_{in} of 380 W and [G- H_2O] of 0.009 vol.%, $R_t \approx 0.085$ °C/W	• End-to-end temperature drop and thermal resistance decreased with [NP] • Evaporator interface temperature decreased 10.3 °C at highest heat rate (380 W) compared to water-filled heat pipe • Optimal fill ratio was identified as 30% fill • SEM analysis showed nanoparticle deposition within the wick structure • Nanoparticle deposition in the wick provided increased nucleation sites, and collision enhanced bubble formation and departure
Poplaski et al. 2016 (Numerical)	Al_2O_3, TiO_2, - CuO d_{NP} (nm):	Volume % 0.5-40	Conventional Cylindrical HP $L_e = 63.5$mm $L_a = 596.5$ mm	• R_t decreased with increasing nanoparticle concentration • At a Q_{in} of 100 W and [Cu] of 35 vol.%,	• Maximum heat transfer rate determined numerically based on capillary limit for three nanoparticles

	20		$L_c = 300$ mm $L_t = 1000$ mm $D_o = 25.4$ mm $D_i = 20.5$ mm	$R_t \approx 0.044$ °C/W • At a Q_{in} of 100 W and [TiO_2] of 30 vol.%, $R_t \approx 0.060$ °C/W • At a Q_{in} of 100 W and [Al_2O_3] of 30 vol.%, $R_t \approx 0.044$ °C/W	• Consideration of thermophysical properties with nanolayer formation on nanoparticles • Parametric study of [NP], Q_{in}, α and β on a nanofluid charged heat pipe • Maximum heat transfer rate was found to be higher for CuO nanofluid by 30% • Decreased R_t with increased [NP]

d_{NP}: average diameter of nanoparticles, FR: fill ratio, HP: heat pipe, HTC: heat transfer coefficient, LHP: loop heat pipe, NP: nanoparticle, NF: nanofluid, Q_{in}: heat input, SEM: scanning electron microscope, TS: thermosyphon, $T_{e,w}$: evaporator wall temperature, ΔT_{ec}: temperature difference between evaporator and condenser, []: concentration

Table 1 **(**Continued).

Table 9: Heat Pipe and Working Fluid Properties, Dimensions and Operating Conditions.

	Case number					
	Case A (Kumaresan et al., 2014)			**Case B** (Putra et al., 2012)		
Fluid	**Base (Water)**	**1% wt CuO**	**1.5% wt CuO**	**Base (Water)**	**1% wt Al_2O_3**	**2% wt Al_2O_3**
k_{BF}/k_{NF} (W/mK)	0.63	0.68	0.69	0.63	0.697	0.788
Heat pipe dimensions						
r_v (mm)	10			2.72		
r_i (mm)	11			3.72		
r_o (mm)	12			4		
L_e (mm)	100			60		
L_a (mm)	80			80		
L_c (mm)	150			60		
Vapor						
k_v (W/mK)	0.0228					
μ_v (N-s/m^2)	1.11e-05					
h_{fg} (kJ/kg)	2360					
Container						
Material	Copper					
k_w (W/mK)	397					
ρ_w (kg/m^3)	8978					
$c_{p,w}$ (J/kgK)	381					
Wick						
Material/type	screen (100 MS)			screen		
N (m^{-1})	NA*			6,742		
φ	0.60			0.6859		
Heat input	Constant source (100 W)			Constant source (30 W)		
Heat output	Constant sink (100 W)			Constant sink (30W)		
k_{eff} (W/mK)	1.20	1.58	1.61	1.16	1.33	1.50
ρ_{eff} (kg/m^3)	3284	3321	3340	1919	1994	2066
$c_{p,eff}$ (J/kgK)	3089	2930	2857	2992	2670	2422

* Porosity value obtained from screen mesh data; thus mesh number is not required (Faghri 2016)

Table 10: Dimensions and Specifications for Parametric Study Heat Pipe

Heat pipe dimensions	
r_v (mm)	10.25
r_i (mm)	11.00
r_o (mm)	12.70
L_e (mm)	63.5 (Starting at 20 mm from endcap)
L_a (mm)	596.5
L_c (mm)	300
L_t (mm)	1000
Vapor	
Working fluid	Water
k_v (W/mK)	0.01926
μ_v (N-s/m^2)	9.13e-06
h_{fg} (kJ/kg)	2360
Container	
Material	Copper
k_w (W/mK)	401
ρ_w (kg/m^3)	8930
$c_{p,w}$ (J/kgK)	386

Table 11: Parametric Study Parameters and Properties

Case 1 Nanoparticle Concentration

Nanoparticle	Alumina (Al_2O_3) / Copper Oxide (CuO) / Titania (TiO2)								
ϕ	0	0.05	0.1	0.15	0.2	0.25	0.3	0.35	0.4
k_{eff} (W/mK)	1.11	1.40 / 1.39 / 1.35	1.76 / 1.72 / 1.64	2.19 / 2.12 / 1.98	2.73 / 2.61 / 2.37	3.41 / 3.23 / 2.86	4.31 / 4.02 / 3.45	5.56 / 5.09 / 4.21	7.40 / 6.59 / 5.19
ρ_{eff} (kg/m^3)	3291	3394 / 3487 / 3406	3498 / 3683 / 3521	3601 / 3879 / 3636	3704 / 4075 / 3751	3807 / 4271 / 3866	3910 / 4467 / 3981	4013 / 4663 / 4096	4117 / 4859 / 4210
μ_{eff} * (Pa/s)x10^4	8.79	8.9	9.02	9.15	9.29	9.44	9.61	9.79	9.99
$c_{p,eff}$ (J/kgK)	3083	2659 / 2422 / 2631	2332 / 1995 / 2288	2070 / 1689 / 2021	1857 / 1479 / 1806	1679 / 1310 / 1630	1529 / 1177 / 1483	1401 / 1069 / 1358	1290 / 979 / 1250
k_{NF} (W/mK)	0.61	0.78 / 0.77 / 0.75	0.97 / 0.95 / 0.91	1.21 / 1.17 / 1.09	1.51 / 1.45 / 1.31	1.89 / 1.79 / 1.58	2.40 / 2.23 / 1.92	3.10 / 2.83 / 2.34	4.13 / 3.67 / 2.89
ρ_{NF} (kg/m^3)	997	1142 / 1273 / 1159	1287 / 1548 / 1320	1433 / 1824 / 1482	1578 / 2100 / 1644	1723 / 2375 / 1805	1868 / 2651 / 1967	2013 / 2927 / 2129	2158 / 3202 / 2290
$c_{p,NF}$ (J/kgK)	4181	3585 / 3250 / 3544	3123 / 2650 / 3063	2755 / 2232 / 2686	2455 / 1923 / 2384	2205 / 1686 / 2136	1994 / 1499 / 1929	1814 / 1346 / 1753	1658 / 1220 / 1602

Case 2 Heat Inputs*

Q (W)	50	100	150	200

Case 3 Nanolayer Thickness*

Nanoparticle	Alumina (Al_2O_3) / Copper Oxide (CuO) / Titania (TiO2)			
β (w/r_{NP})	0.10	0.15	0.20	0.25
k_{eff} (W/mK)	1.33 / 1.32 / 1.29	1.37 / 1.35 / 1.32	1.40 / 1.39 / 1.35	1.45 / 1.43 / 1.39
ρ_{eff} (kg/m^3)	3394 / 3487 / 3406	3394 / 3487 / 3406	3394 / 3487 / 3406	3394 / 3487 / 3406
k_{NF} (W/mK)	0.736 / 0.730 / 0.715	0.755 / 0.748 / 0.731	0.78 / 0.77 / 0.75	0.800 / 0.768 / 0.768

Case 4 Nanolayer to Nanoparticle Thermal Conductivity *

Nanoparticle	Alumina (Al_2O_3) / Copper Oxide (CuO) / Titania (TiO2)					
α (k_{layer}/k_{NP})	0.25	0.5	0.75	1	1.25	1.5
k_{eff} (W/mK)	1.392 / 1.366 / 1.314	1.399 / 1.379 / 1.337	1.403 / 1.385 / 1.347	1.405 / 1.389 / 1.354	1.406 / 1.392 / 1.360	1.407 / 1.394 / 1.364
k_{NF} (W/mK)	0.769 / 0.755 / 0.726	0.773 / 0.762 / 0.739	0.775 / 0.766 / 0.745	0.776/ 0.768 / 0.749	0.777 / 0.769 / 0.751	0.778 / 0.770 / 0.754
k_{NP} (W/mK)	9 / 4.5 / 2	18 / 9 / 4	27 / 13.5 / 6	36 / 18 / 8	45 / 22.5 / 10	54 / 27 / 12

*Properties not provided in this section are the same as Nanoparticle Concentration section. Unless otherwise noted, the heat rate Q at the evaporator of the heat pipe was 100 W, the ratio of thermal conductivity of the nanolayer to nanoparticle α was unity, and the ratio of the nanolayer thickness to nanoparticle radius β was 20%.

Chapter 3. Two-Phase Numerical Simulation of a Two-Phased Closed Thermosyphon

Nomenclature:

C_p	specific heat (W/kg K)	*Subscripts*	
E	enthalpy (J/kgK)	a	adiabatic
F_{CSF}	continuum surface force (N)	abs	absolute
h	heat transfer coefficient (W/m^2 K)	c	condenser
h_{lv}	latent heat (J/kg)	CSF	continuum surface
k	thermal conductivity (W/m K)	e	evaporator
L	length (m)	eff	effective
p	pressure (Pa)	l	liquid
Q	heat rate (W)	lv	liquid to vapor
q	heat flux (W/m^2)	mix	mixture
R	thermal resistance (W/K)	o	outer
R_g	universal gas constant (J/kg K)	sat	saturation
r	radius (m), relaxation time (1/s)	v	vapor
S_E	energy source term (w/m^3)	0	reference value
S_M	mass source term (kg/m^3)	∞	free stream
T	temperature (K)	*coordinates*	*r, x*
u	velocity magnitude (m/s), Volume (m^3)		
V	volume (m^3)		
v	specific volume (m^3/kg)		
α	volume fraction		
ρ	density (kg/m^3)		
σ	surface tension (N/m)		
ν	kinematic viscosity (m^2/s)		
Φ	arbitrary property		

Introduction:

Heat pipes are passive two-phase devices that utilize the latent energy of a working fluid as a means of transport for thermal energy with minimal thermal resistance. Heat pipes allow for flexibility in choice of working fluid and container material as well as robustness in design, and the ability to dissipate high heat fluxes over a small cross-sectional area with various shape configurations. The aforementioned characteristics of heat pipes makes them ideal for many engineering applications [1]–[3]. A heat pipe operates through the principals of latent heat transfer; where heat input at the evaporator vaporizes the working fluid in the wick the vapor is then transported to the condenser section due to a pressure gradient where it condenses. Heat pipes contain three main regions: a container, which provides structural rigidity, a wick, whose capillary action is responsible for return of condensed working fluid to the evaporator and a vapor core, where the vaporized working fluid is transported to the condenser section. With the increasing CPU clock speed and associated power requirements of modern day computers, comes a greater demand for improvements in passive thermal management devices such as heat pipes [4]. Heat pipes are utilized primarily in laptops and high end desktops for CPU cooling [2]–[4] however, other applications such as heat exchanger systems [5], power plants dry cooling towers [6], [7], and solar thermal energy storage devices [4], [8]–[14] are other proposed uses of heat pipe technologies.

A special type of heat pipes called thermosyphons do not include a wick, but rather employ a condenser located above the evaporator to exploit the gravitational force in return of the working fluid [3]. Thermosyphons can only transfer heat in one direction, making them an effective thermal diode[15]. Thermosyphons have proven to have distinct advantages over heat pipes in certain applications including: micro scale heat transfer [16]–[18], reduction of permafrost melting [19] and aircraft cabin cooling [20]. Riffae et al. [17] showed that micro thermosyphons have increased heat transfer rates compared to those of miniature heat pipes of the same cross sectional area. This increase in heat transfer capacity is attributed to the miniature heat pipe hitting the entrainment limit. In the Qinghai–Tibet Plateau region of China, thermosyphons are used in another important application where they limit the melting of permafrost under power transmission lines; effectively mitigating frost heave damage to the infrastructure [19]. Since heat transfer may only occur from the permafrost in the ground to the air on the surface, due to a lack of capillary structure, no melting will occur when the air temperature becomes hotter than the permafrost. Oliveira et al. [20] demonstrated the practical use of a loop thermosyphon as heat exchanger system in an aircraft. Due to lower weight than a heat pipe attributed to lack of a capillary structure and one way heat transfer ability, thermosyphons were ideal in this application. Loop thermosyphosn were imbedded in the cabin wall and heat was rejected to the HVAC system as well as to the outer portion of the fuselage.

Numerous experimental studies have been performed to optimize the thermal performance of thermosyphons through fill ratio (FR) [21], [22] and inclination angle [23]–[25]. The FR is the ratio of liquid volume to the total evaporator volume inside the thermosyphon and greatly impacts the thermal response time and thermal resistance of a thermosyphon [26]. An under-filled thermosyphons can experience dryout, where dramatic increases in evaporator temperature occur due to complete evaporation of the working fluid, while overfilled thermosyphons can have a longer

thermal response time and higher overall thermal resistance due to a larger liquid pool volume [26] . The inclination angle greatly impacts the performance of a thermosyphon due to the gravitational effect which can cause a thickening or thinning in the liquid film and a variation in the speed of condensate return. Furthermore, flooding limit semi-empirical correlations including the effects of thermosyphon diameter, surface tension and fluid properties was proposed by Faghri et al [27].

In some studies nanofluids have been employed to further enhance the conductivity of the working fluid through addition of nanoparticle solids [24], [28]–[32]. The most popular nanoparticles include: titanium oxide, copper oxide and aluminum oxide in most cases the overall thermal resistance of the thermosyphon was found to decrease with an increase in nanoparticle concentration [24], [30], [31]. However, there is still some disagreement on the mechanism responsible for these improvements.

Numerous numerical simulations have been performed using computational fluid dynamics (CFD) of the two-phase thermosyphon [24], [24]–[26], [33]–[36]. Numerical simulation of the liquid and vapor flow within a thermosyphon is accomplished in the following manners: 1) as two physically separated phases each with its own set of localized governing equations for mass, momentum and energy conservation (localized separated flow method) or 2) as a multiphase mixture which requires that volume averaging be performed on the governing equations (Eulerian or Lagragian average). Once the volume averaged governing equations have been formulated, they are resolved based on individual phases or over the entire mixture depending on the choice of multiphase model (homogenous, separated flow mixture or multifluid).

Modeling of a thermosyphon using localized separated flow (LSF) has been widely performed due to its lower computational cost and relatively high degree of accuracy [4], [21], [26], [28], [32], [36], [37]. A LSF numerical model of a thermosyphon was presented by Harley and Faghri [37] which implemented Nusselt analysis to model the heat transfer through the liquid film in a thermosyphon in addition to the two-dimensional numerical modeling of the heat transfer in the wall and vapor core. The results of their numerical simulations successfully predicted wall temperature profiles for low temperature heat pipes.

The LSF numerical model of Harley and Faghri [37] was extended by Shabgard et al. [26] to perform two dimensional transient simulations of a thermosyphons operation under various filling ratios. The mass momentum and energy equations were solved using a finite volume discretization method accounting for heat transfer through the liquid film and in the liquid pool at the bottom of the thermosyphon. Validation with experimental data was performed against two thermosyphons with different fill ratios and heat inputs, where good agreement was found, followed by a numerical study on the optimal fill ratio which was shown to lower the thermal response time of the thermosyphon. Despite its accuracy in predicting thermal operation as well as vapor velocity distribution, the LSF model lacks necessary physics to model complex processes such as boiling and condensation as well and provides no insight into the limitations produced by flooding effects.

In recent years multiphase modeling has become a more popular method of thermosyphon numerical simulation primarily for its ability caputre the details of boiling and condensation [28],

[34]–[36], [38]–[40]. The most common multiphase flow models are : a) homogenous, b) multi-fluid and c) separated flow mixture [41].

In order to use a multiphase model the governing equations must be averaged using Eulerian or Lagrangian averaging techniques [41]. In Eulerian the approach, an average is taken over both time and volume of the domain. The volume average may be taken intrinsicly, over each phase; or over the entire domain, extrinsically. Similar to Eulerian appraoch, Lagrangian averaging applies the Lagrangian definition of a system, and only performs a temporal averaging.

The homogenous multiphase model is obtained if spatial averaging is performed over each phase and then the averaged governing equations in each category are summed overall all phases. Since all phase are assumed to move as a homogenous mixture, a mass-averaged mixture velocity is used in the continuity, momentum, and energy equation in place of individual phase velocities. In performing the aforementioned simplification, the continuity equation is solved for each phase while a single momentum and energy equation are solved throughout the domain. Sometimes this method of modeling is referred to as volume of fluid modeling (VOF) [42], however volume of fluid is the name of the interface tracking methodology used in the two phase models to distinguish between liquid and vapor cells [41].

The multifluid model is obtained [41] by averaging each phase within the control volume. In this model each phase has its own separate set of governing equations for mass, momentum and energy. In order for there to be closure on this model, additional source terms are needed to account for the interaction between phases. Due to the use of Eulerian averaging over the domain, and the consideration of unique continuity, momentum and energy equation for each phase this model is commonly referred to as Eulerian modeling in some CFD comercial codes [42].

Separated flow mixture model is the intermediate between the multfluid and homogenous models. In this model spatial averaging is performed and the individual phase governing equations are summed for continuity, momentum and energy. The velocity is not mass averaged, but rather the velocities are allowed to differ between phases. In addition, the pressure over the domain is assumed to be the same between phases. Due to the differing phase velocity and associated mixing of distinct phases, the model is referred to as the mixture model [42].

Homogenous modeling has been found to be an effective way to capture the physics of evaporation and condensation within thermosyphons [34], [35], [40]. Several thermosyphon numerical models have been based on the work of De Shepper et al. [43] who created a homogenous numerical simulation to model the boiling, evaporation and condensation of hydrocarbon feedstock in a steam cracker. Source terms added to the continuity equations for the liquid and vapor phase to account for the evaporation and condensation of the working fluid. One source term accounts for energy exchange between the phases, since a single energy equation is resolved in this method. It was determined that the temperature dependence of thermophysical properties needed to be considered in order to obtain accurate results.

Building on the work of De Shepper et al. [43] , Alizadehdakhel et al. [40] developed a homogenous model to numerically simulate the operation of a two-phase thermosyphon. The variation in fluid properties with temperature as well as the interaction of the two phases due to

surface tension were considered. The effects of non-condensable gases were also included in the liquid and vapor mass source terms. Numerical results were obtained for various heat inputs and fill ratios and were then compared to experimental data with reasonable agreement. Similarly, Fadhl et al. [34] used homogenous modeling and the aforementioned source terms of De Shepper et al. [43] for mode1ing of a water filled thermosyphon. Experimental wall temperature data was obtained to validate numerical results and a transient visualization of the boiling process was performed using the numerical simulation. Thermosyphons using refrigerates R134a and R404a were simulated using the same homogenous model of Fadhl et al. [34] by Fadhl et al. [35]. Flow visualization was provided for the transient evaporation and condensation process up to 120 seconds.

Expanding on the work of Fadhl et al. [34] and Fadhl et al. [35], Jouhara H et al. [38] used 3-dimensional homogenous modeling to obtain flow visualization of boiling in a thermosyphon. It was found when compared to experimental results that 3-dimensional homogenous model can successfully predict geyser boiling flow patterns inside a two-phase closed thermosyphon.

The multi-fluid model was used by Kafeel and Turan [39] to simulate both transient and steady state operation of a thermosyphon under different heating rates. In this model the continuity, momentum and energy equation were solved for both the vapor and the liquid phase with evaporation and condensation of the working fluid resolved by implementing an interfacial mass transfer term into the phase continuity equations. The drag between phases is considered through the uses of interphase exchange coefficients in the momentum equations. It was shown that this method of modeling can accurately describe the behavior of a two-phase closed thermosyphon.

The separated flow mixture model was employed by Lin et al. [36] to simulate boiling and condensation inside a thermoshphon. In this model, local equilibrium is assumed over small lengths, and the governing equation are resolved by solving the energy equations for the mixture as well as the volume fraction for the primary and secondary phase and each respective phase velocity. Source terms were provided to simulate the mass transfer from liquid to vapor through specified drift velocities. Lin et al. [36] showed experimental and numerically that the separated flow model was a more appropriate method for use in modeling of oscillating heat pipes than the homogenous or multi-fluid models.

In this effort, a comprehensive approach was taken simulating two phase performance of a thermosyphon assuming temperature dependent thermophysical properties. The proposed model predicted both the flooding limit and optimal fill ratio of a thermosyphon, and was validated through established empirical correlations. To the author's best knowledge, this is the first two phase simulation of a thermosyphon to predict both the flooding limit and optimal fill ratio without the use of empirical correlations.

Two Phase Simulation Analysis:

The governing equations for mass, momentum and energy are solved using the homogenous multiphase modeling where the velocity, pressure and temperature field are shared by all phases however, the continuity equation for each phase is considered in order to determine the volume fraction of each cell. The volume fraction of each phase is defined as [41]:

$$\alpha_k = \frac{\Delta V_k}{\Delta V} \tag{58}$$

where ΔV is the total differential cell volume and ΔV_k is the differential phase volume.

By definition, the sum of all volume fractions must be unity where $\sum_{k=1}^{\Pi} \alpha_k = 1$ and $k = l$ or v. The volume is assumed to be all liquid if $\alpha_l = 1$ or if $\alpha_v = 0$. A similar statement may be made for the vapor phase.

In cells where the volume fraction is between 0 and 1 an interface is assumed to occur, thus effective properties of the following form are used:

$$\Phi_{eff} = \sum_{k}^{N} \alpha_k \Phi_k \tag{59}$$

where Φ is a property of the mixture, liquid or vapor phase, such as: viscosity, density, thermal conductivity and specific heat.

Phase Continuity:

The continuity equation for each phase assuming two-dimensional axisymmetric, laminar flow, with a source terms accounting for the mass transfer due to evaporation and condensation is:

$$\frac{\partial}{\partial t}(\alpha_k \rho_k) + \frac{\partial}{\partial x}(\rho_k u_x) + \frac{\partial}{\partial r}(\rho_k u_r) + \frac{\rho_k u_r}{r} = S_M \tag{60}$$

The mass source terms are added to account for the phase change due to boiling and condensation with consideration to volume average mixture temperature T_{mix} to differentiate between processes [43]:

For condensation $T_{sat} < T_{mix}$:

Liquid:

$$S_M = r_{vl}\alpha_v\rho_v\frac{T_{sat}-T_{mix}}{T_{sat}} \tag{61}$$

Vapor:

$$S_M = -r_{lv}\alpha_v\rho_v\frac{T_{sat}-T_{mix}}{T_{sat}} \tag{62}$$

For evaporation $T_{sat} > T_{mix}$ *:*

Liquid:

$$S_M = -r_{vl}\alpha_l\rho_l\frac{T_{mix}-T_{sat}}{T_{sat}} \tag{63}$$

Vapor:

$$S_M = r_{lv}\alpha_l\rho_l\frac{T_{mix}-T_{sat}}{T_{sat}} \tag{64}$$

where r_{lv} and r_{vl} are the relaxation time for evaporation and condensation respectively. For this work a value of 0.1 1/s for evaporation and 90,000 1/s for condensation was selected based on previous physical models [33]–[35], [38], [43]. The vapor density is assumed to vary with the ideal gas equation of state while the liquid density follows the following relation [1]:

$$\begin{aligned}\rho_l = {} & 1430 - 7.008T + 4.426\cdot10^{-2}T^2 - 1.306\cdot10^{-4}T^3 \\ & + 1.781\cdot10^{-6}T^4 - 9.501\cdot10^{-11}T^5\end{aligned} \tag{65}$$

Momentum Equations:

The momentum equation for the homogenous mixture is solved in both the radial and axial directions with terms included to account for the interaction between phases due to surface tension. Fluid flow was assumed to laminar and the vapor was modeled as a compressible ideal gas. In addition, the forces of pressure, gravity, surface tension and friction were considered [34]:

axial momentum:

$$\frac{\partial}{\partial t}\left(\rho_{eff}u_x\right)+\frac{1}{r}\frac{\partial}{\partial x}\left(r\rho_{eff}u_xu_x\right)+\frac{1}{r}\frac{\partial}{\partial r}\left(r\rho_{eff}u_ru_x\right)=\rho_{eff}g_x+\frac{\partial p}{\partial x}+$$
$$\frac{1}{r}\frac{\partial}{\partial x}\left[r\mu_{eff}\left(2\frac{\partial u_x}{\partial x}--\frac{2}{3}\left(\nabla\cdot\mathbf{u}\right)\right)\right]+\frac{1}{r}\frac{\partial}{\partial r}\left[r\mu_{eff}\left(\frac{\partial u_x}{\partial r}+\frac{\partial u_r}{\partial x}\right)\right]+F_{CSF,x} \quad (66)$$

radial momentum:

$$\frac{\partial}{\partial t}\left(\rho_{eff}u_r\right)+\frac{1}{r}\frac{\partial}{\partial x}\left(r\rho_{eff}u_ru_x\right)+\frac{1}{r}\frac{\partial}{\partial r}\left(r\rho_{eff}u_ru_r\right)=\rho_{eff}g_r+\frac{\partial p}{\partial r}+$$
$$\frac{1}{r}\frac{\partial}{\partial x}\left[r\mu_{eff}\left(\frac{\partial u_r}{\partial x}+\frac{\partial u_x}{\partial r}\right)\right]+\frac{1}{r}\frac{\partial}{\partial r}\left[r\mu_{eff}\left(2\frac{\partial u_r}{\partial r}--\frac{2}{3}\left(\nabla\cdot\mathbf{u}\right)\right)\right] \quad (67)$$
$$-2\mu_{eff}\frac{u_r}{r^2}+\frac{2}{3}\frac{\mu_{eff}}{r}\left(\nabla\cdot\mathbf{u}\right)+F_{CSF,r}$$

F_{CSF} is the continuum surface force which arises due to the surface tension between the liquid and vapor. The continuum surface force model proposed by Brackbill et al. [44] was used to obtain the interaction force :

$$F_{CSF}=\sigma_{lv}\frac{\alpha_l\rho_lK_l+\alpha_v\rho_vK_v}{\frac{1}{2}\left(\rho_l+\rho_v\right)} \quad (68)$$

The curvature *K* for each phase is defined as the divergence of the surface normal vector [41].

The surface tension (σ_{lv}) in equation (68) is assumed temperature dependent [1]:

$$\sigma_{lv}=0.0575+4.489\cdot10^{-4}T_{mix}-2.393\cdot10^{-6}{T_{mix}}^2$$
$$+5.099\cdot10^{-9}{T_{mix}}^3-6.261\cdot10^{-12}{T_{mix}}^4+3.255\cdot10^{-15}{T_{mix}}^5 \quad (69)$$

where T_{mix} is the temperature of the liquid and vapor mixture.

Energy equation:

Since one energy equation is used in homogenous modeling and shared between all phases, a source term must be appended to account for the energy stored or released due to phase change and is done so as follows:

$$\rho_{eff}\left(\frac{\partial E}{\partial t}+u_r\frac{\partial E}{\partial r}+u_x\frac{\partial E}{\partial x}+u_r\frac{\partial p}{\partial r}+u_x\frac{\partial p}{\partial x}\right)=k_{eff}\left(\frac{1}{r}\frac{\partial}{\partial r}\left(r\frac{\partial T}{\partial r}\right)+\frac{\partial^2T}{\partial x^2}\right)+S_E \quad (70)$$

In homogenous modeling the enthalpy term in equation (70) is taken to be a mass average variable:

$$E = \frac{\alpha_l \rho_l E_l + \alpha_v \rho_v E_v}{\alpha_l \rho_l + \alpha_v \rho_v} \tag{71}$$

where E_l *and* E_v are the enthalpy of the liquid and vapor respectively and are obtained using specific heats of each along with the mixture temperature.

The source term in equation (70) is defined for condensation, when latent energy is released, and evaporation, when energy is stored [43]:

Condensation $T_{sat} < T_{mix}$*:*

$$S_E = r_{vl} \alpha_v \rho_v h_{lv} \frac{T_{sat} - T_{mix}}{T_{sat}} \tag{72}$$

Evaporation $T_{sat} > T_{mix}$*:*

$$S_E = -r_{lv} \alpha_v \rho_v h_{lv} \frac{T_{mix} - T_{sat}}{T_{sat}} \tag{73}$$

Boundary Conditions:

The no slip condition was applied at all wall surfaces inside the thermosyphon. The thermal boundary conditions are:

Evaporator:

$$k \left. \frac{dT}{dx} \right|_{r=\pm r_o,\ 0<x<L_e} = q \tag{74}$$

Condenser:

$$k \left. \frac{dT}{dx} \right|_{r=\pm r_o,\ L_e+L_a<x<L_e+L_a+L_c} = h(T_\infty - T_c) \tag{75}$$

Adiabatic Sections:

$$k \left. \frac{dT}{dx} \right|_{r=\pm r_o,\ L_e<x<L_e+L_a} = 0 \tag{76}$$

the end caps at $x=0$ and $x=l$ are also assumed to be insulated like the adiabatic section.

Solution Methodology:
A homogenous multiphase model was used for simulation of the condensation and boiling inside the thermosyphon in order to resolve the liquid vapor interface, a VOF interface tracking technique with a liquid cutoff ratio of 1e-13 was employed. A steady state formulation with a pseudo transient solution scheme was used to add time variant parameters into the steady governing equations to provide necessary initial conditions for the condensation and boiling processes. A coupled solution scheme was used to resolve pressure and velocity while quick was used for volume fraction, energy and momentum. Iterations were performed until the residuals for mass, momentum and energy were less than 1e-4 and the surface averaged liquid volume fraction on the cold wall changed less than 5% in 10000 iterations.

Results:
The relaxation time used in boiling has been widely accepted [33]–[35], [38], [43] , however a wide range of values for the condensation relaxation time have been used and is the source of much dispute [33] . In order to validate the relaxation time used for condensation in this model film thickness values were compared to those obtained from the classical Nusselt condensation analytical model. In the test case a vertical flat plate was exposed to a quiescent reservoir of saturated water vapor at 363 K. The vertical plate was held at a constant surface temperature of 340 K so that condensation would occur on its surface. In Figure 25 the film thickness is plotted along the length of the vertical plate stating at the upper edge; the initial film thickness was found to deviate from the analytical Nusselt condensation model. This is largely attributed to linear temperature dependence of equation (72), however within 5 cm this deviation quickly disappears and the final solution shows only a 1 percent variation from the analytical solution.

Conclusion:
A two-phase numerical simulation was created for the simulation of a thermosyphon. The thermal relaxation time for the condenser was found to be 90,000 1/s and showed good agreement with Nusselt condensation on a flat plate. Further research is required to determine the operating temperature range and geometry the thermal relaxation time is applicable for. In addition the thermal relaxation time for boiling in the evaporator region needs to be validated. There is a need for a model which requires no constant relaxation time, but rather can adapt to the internal heat pipe conditions.

References:

[1] A. Faghri, *Heat Pipe Science and Technology*, 2nd ed. Global Digital Press, 2016.

[2] A. Faghri, "Heat Pipes: Review, Opportunities and Challenges," *Frontiers in Heat Pipes*, vol. 5, no. 1, 2014.

[3] A. Faghri, "Review and Advances in Heat Pipe Science and Technology," *Journal of Heat Transfer*, vol. 134, no. 12. p. 123001, 2012.

[4] H. Shabgard, M. J. Allen, N. Sharifi, S. P. Benn, A. Faghri, and T. Bergman, "Heat Pipe Heat Exchangers and Heat Sinks: Opportunities, Challenges, Applications, Analysis, and State of the Art," *International Journal of Heat and Mass Transfer*, vol. 89, no. 2015, pp. 138–158, 2015.

[5] V. L, "Heat Pipes and Heat Pipe Exchangers for a Heat Recovery Systems," *Journal of Heat and Recovery Systems*, vol. 4, no. 4, pp. 227–233, 1984.

[6] S. P. Benn, L. M. Poplaski, A. Faghri, and T. L. Bergman, "Analysis of thermosyphon/heat pipe integration for feasibility of dry cooling for thermoelectric power generation," *Applied Thermal Engineering*, vol. 104, pp. 358–374, 2016.

[7] R. A. and C. E., "Development and Operational Testing of a Heat Pipe Dry Cooling Tower," in *Joint Power Generation Conference*, 1980, pp. 1157–1562.

[8] N. Sharifi, T. L. Bergman, and A. Faghri, "Enhancement of PCM melting in enclosures with horizontally-finned internal surfaces," *International Journal of Heat and Mass Transfer*, vol. 54, no. 19–20, pp. 4182–4192, 2011.

[9] N. Sharifi, S. Wang, T. L. Bergman, and A. Faghri, "Heat pipe-assisted melting of a phase change material," *International Journal of Heat and Mass Transfer*, vol. 55, no. 13–14, pp. 3458–3469, 2012.

[10] N. Sharifi, C. W. Robak, T. L. Bergman, and A. Faghri, "Three-dimensional PCM melting in a vertical cylindrical enclosure including the effects of tilting," *International Journal of Heat and Mass Transfer*, vol. 65, pp. 798–806, 2013.

[11] N. Sharifi, A. Faghri, T. L. Bergman, and C. E. Andraka, "Simulation of heat pipe-assisted latent heat thermal energy storage with simultaneous charging and discharging," *International Journal of Heat and Mass Transfer*, vol. 80, pp. 170–179, 2015.

[12] N. Sharifi, T. L. Bergman, M. J. Allen, and A. Faghri, "Melting and solidification enhancement using a combined heat pipe, foil approach," *International Journal of Heat and Mass Transfer*, vol. 78, pp. 930–941, 2014.

[13] M. J. Allen, N. Sharifi, A. Faghri, and T. L. Bergman, "Effect of inclination angle during melting and solidification of a phase change material using a combined heat pipe-metal foam or foil configuration," *International Journal of Heat and Mass Transfer*, vol. 80, pp. 767–780, 2015.

[14] M. J. Allen, T. L. Bergman, A. Faghri, and N. Sharifi, "Robust Heat Transfer Enhancement During Melting and Solidification of a Phase Change Material Using a Combined Heat Pipe-Metal Foam or Foil Configuration," *Journal of Heat Transfer*, vol. 137, no. 10, pp. 102301–

102301, 2015.

[15] S. Almsater, W. Saman, and F. Bruno, “Performance Enhancement of High Temperature Latent Heat Thermal Storage Systems Using Heat Pipes With and Without Fins for Concentrating Solar Thermal Power Plants,” *Renewable Energy*, vol. 89, pp. 36–50, 2016.

[16] Y. Chen, F. Yu, C. Zhang, and X. Liu, “Experimental study on thermo-hydrodynamic behaviors in miniaturized two-phase thermosyphons,” *International Journal of Heat and Mass Transfer*, vol. 100, pp. 550–558, 2016.

[17] S. B. Riffat, X. Zhao, and P. S. Doherty, “Analytical and numerical simulation of the thermal performance of ‘mini’ gravitational and ‘micro’ gravitational heat pipes,” *Applied Thermal Engineering*, vol. 22, no. 9, pp. 1047–1068, 2002.

[18] L. L. Vasiliev, “Micro and miniature heat pipes - Electronic component coolers,” *Applied Thermal Engineering*, vol. 28, no. 4, pp. 266–273, 2008.

[19] L. Guo, Q. Yu, Y. You, X. Wang, X. Li, and C. Yuan, “Cooling effects of thermosyphons in tower foundation soils in permafrost regions along the Qinghai–Tibet Power Transmission Line from Golmud, Qinghai Province to Lhasa, Tibet Autonomous Region, China,” *Cold Regions Science and Technology*, vol. 121, pp. 196–204, 2016.

[20] J. L. G. Oliveira, C. Tecchio, K. V. Paiva, M. B. H. Mantelli, R. Gandolfi, and L. G. S. Ribeiro, “In-flight testing of loop thermosyphons for aircraft cooling,” *Applied Thermal Engineering*, vol. 98, pp. 144–156, 2016.

[21] B. Jiao, L. M. Qiu, X. B. Zhang, and Y. Zhang, “Investigation on the effect of filling ratio on the steady-state heat transfer performance of a vertical two-phase closed thermosyphon,” *Applied Thermal Engineering*, vol. 28, no. 11–12, pp. 1417–1426, 2008.

[22] “Heat Transfer Enhancement in a Closed Thermosyphon with Thermally Conductive PA6/Water,” *Applied Thermal Engineering*, 2016.

[23] M. Ghanbarpour, N. Nikkam, R. Khodabandeh, and M. S. Toprak, “Thermal performance of inclined screen mesh heat pipes using silver nanofluids,” *International Communications in Heat and Mass Transfer*, vol. 67, pp. 14–20, 2015.

[24] G. Huminic and A. Huminic, “Numerical Study on Heat Transfer Characteristics of Thermosyphon Heat Pipes Using Nanofluids,” *Energy Conversion and Management*, vol. 76, pp. 393–399, 2013.

[25] G. Huminic, A. Huminic, I. Morjan, and F. Dumitrache, “Experimental study of the thermal performance of thermosyphon heat pipe using iron oxide nanoparticles,” *International Journal of Heat and Mass Transfer*, vol. 54, no. 1–3, pp. 656–661, 2011.

[26] H. Shabgard, B. Xiao, A. Faghri, R. Gupta, and W. Weissman, “Thermal characteristics of a closed thermosyphon under various filling conditions,” *International Journal of Heat and Mass Transfer*, vol. 70, pp. 91–102, 2014.

[27] A. Faghri, M. M. Chen, and M. Morgan, “Heat transfer characteristics in two-phase closed conventional and concentric annular thermosyphons,” *Transactions of the ASME Journal of Heat Transfer*, vol. 111, no. 3, pp. 611–618, 1989.

[28] S. Khandekar, Y. M. Joshi, and B. Mehta, “Thermal Performance of Closed Two-phase Thermosyphon Using Nanofluids,” *International Journal of Thermal Sciences*, vol. 47, no. 6, pp. 659–667, 2008.

[29] H. S. Xue, J. R. Fan, Y. C. Hu, R. H. Hong, and K. F. Cen, “The interface effect of carbon nanotube suspension on the thermal performance of a two-phase closed thermosyphon,” *Journal of Applied Physics*, vol. 100, no. 10, p. 104909, 2006.

[30] S. H. Noie, S. Z. Heris, M. Kahani, and S. M. Nowee, “Heat transfer enhancement using Al2O3/water nanofluid in a two-phase closed thermosyphon,” *International Journal of Heat and Fluid Flow*, vol. 30, no. 4, pp. 700–705, 2009.

[31] T. Grab, U. Gross, U. Franzke, and M. Buschmann, “Operation performance of thermosyphons employing titania and gold nanofluids,” *International Journal of Thermal Sciences*, vol. 86, pp. 352–364, 2014.

[32] B. Mehta and S. Khandekar, “Two-Phase Closed Thermosyphon with Nanofluids,” in *14th International Heat Pipe Conference*, 2007.

[33] M. Lecki and G. Gorecki, “Different Approaches to FVM Method Fluid Flow and Heat Transfer Simulation Inside Thermosyphon,” in *Proceedings of the 15th internationl heat transfer conference*, 2014, pp. 1–15.

[34] B. Fadhl, L. C. Wrobel, and H. Jouhara, “Numerical modelling of the temperature distribution in a two-phase closed thermosyphon,” *Applied Thermal Engineering*, vol. 60, no. 1–2, pp. 122–131, 2013.

[35] B. Fadhl, L. C. Wrobel, and H. Jouhara, “CFD modelling of a two-phase closed thermosyphon charged with R134a and R404a,” *Applied Thermal Engineering*, vol. 78, pp. 482–490, 2015.

[36] Z. Lin, S. Wang, R. Shirakashi, and L. Winston Zhang, “Simulation of a miniature oscillating heat pipe in bottom heating mode using CFD with unsteady modeling,” *International Journal of Heat and Mass Transfer*, vol. 57, no. 2, pp. 642–656, 2013.

[37] C. Harley and A. Faghri, “Complete transient two-dimensional analysis of twophase closed thermosyphons including the falling condensate film,” *ASME Journal of Heat Transfer*, vol. 116, no. 2, pp. 418–426, 1994.

[38] H. Jouhara, B. Fadhl, and L. C. Wrobel, “Three-dimensional CFD Simulaiton of Geyser Boiling in a Two-Phase Closed Thermosyphon,” *i n t e r n a t i o n a l journal of hydrogen energy xxx*, no. I–I4, pp. 1–14, 2016.

[39] K. Kafeel and A. Turan, “Simulation of the response of a thermosyphon under pulsed heat input conditions,” *International Journal of Thermal Sciences*, vol. 80, no. 1, pp. 33–40, 2014.

[40] A. Alizadehdakhel, M. Rahimi, and A. A. Alsairafi, “CFD Modeling of Flow and Heat Transfer in a Thermosyphon,” *International Communications in Heat and Mass Transfer*, vol. 37, no. 3, pp. 312–318, 2010.

[41] A. Faghri and Y. Zhang, *Transport Phenomena in Multiphase Systems*. 2006.

[42] I. Ansys, “ANSYS FLUENT 12 . 0 UDF Manual,” *Knowledge Creation Diffusion Utilization*,

vol. 15317, no. April, pp. 724–746, 2009.

[43] S. C. K. De Schepper, G. J. Heynderickx, and G. B. Marin, “Modeling the evaporation of a hydrocarbon feedstock in the convection section of a steam cracker,” *Computers and Chemical Engineering*, vol. 33, no. 1, pp. 122–132, 2009.

[44] J. U. Brackbill, D. B. Kothe, and C. Zemach, “A continuum method for modeling surface tension,” *Journal of Computational Physics*, vol. 100, no. 2, pp. 335–354, 1992.

List of Figures:

Figure 1: Two-Phase Closed Thermosyphon During Operation with Dimensions 102

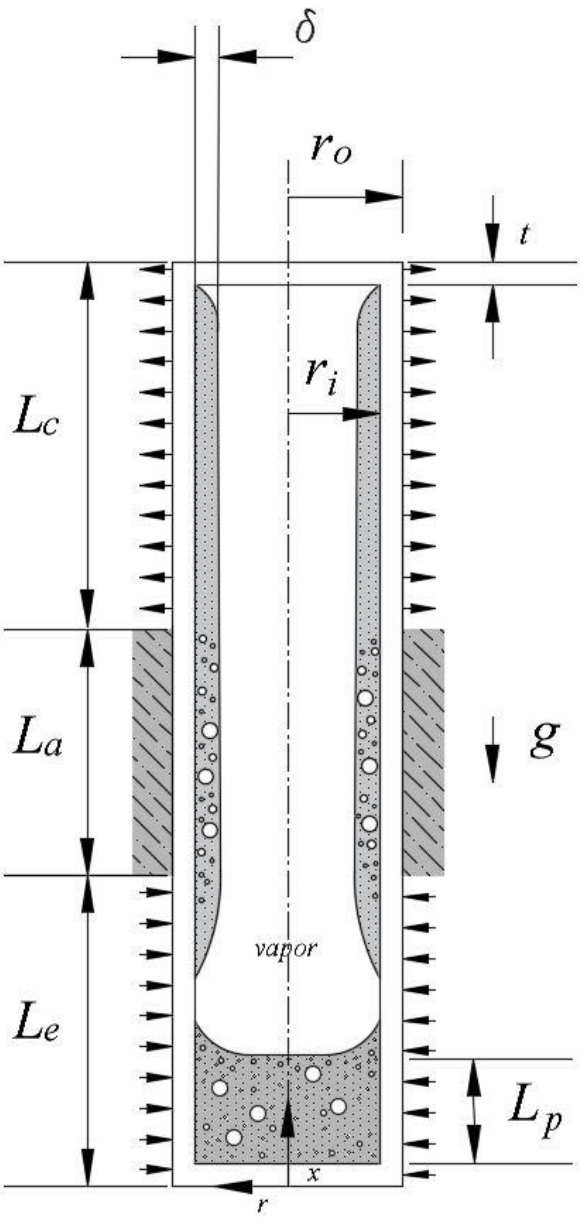

Figure 24: Two-phase closed thermosyphon

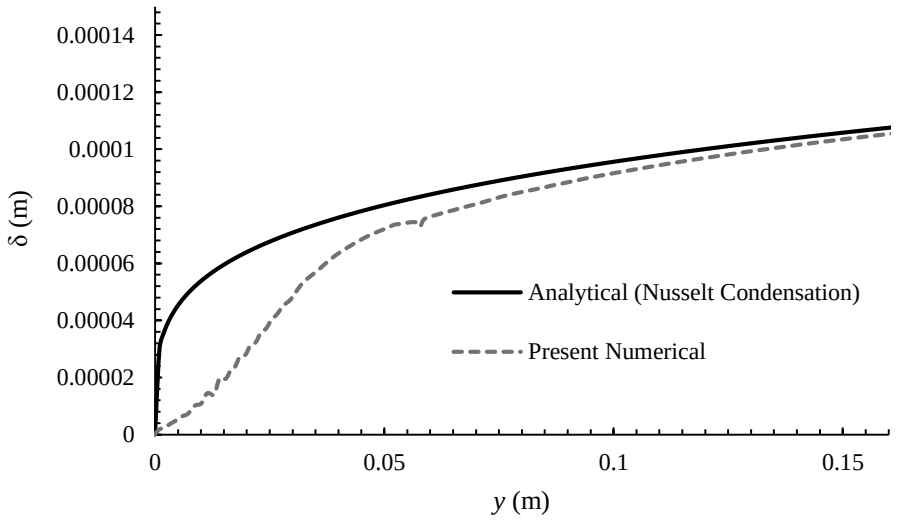

Figure 25 Film thickness VS plate length comparison to Nusselt analytical